HIGH-EFFICIENCY ARRAYS OF INDUCTIVE COILS

A THESIS

SUBMITTED TO THE DEPARTMENT OF ELECTRICAL AND

ELECTRONICS ENGINEERING

AND THE GRADUATE SCHOOL OF ENGINEERING AND SCIENCE

OF BILKENT UNIVERSITY

IN PARTIAL FULFILLMENT OF THE REQUIREMENTS

FOR THE DEGREE OF

MASTER OF SCIENCE

By

Erdal Gönendik

July, 2014

I certify that I have read this thesis and that in my opinion it is fully adequate, in scope and in quality, as a thesis for the degree of Master of Science.

Assoc. Prof. Dr. Hilmi Volkan Demir (Advisor)

I certify that I have read this thesis and that in my opinion it is fully adequate, in scope and in quality, as a thesis for the degree of Master of Science.

Prof. Dr. Ayhan Altıntaş

I certify that I have read this thesis and that in my opinion it is fully adequate, in scope and in quality, as a thesis for the degree of Master of Science.

Assist. Prof. Dr. Yiğit Karpat

Approved for the Graduate School of Engineering and Science:

Prof. Dr. Levent Onural
Director of the Graduate School

ABSTRACT

HIGH-EFFICIENCY ARRAYS OF INDUCTIVE COILS

Erdal Gönendik
M.S. in Electrical and Electronics Engineering
Supervisor: Assoc. Prof. Dr. Hilmi Volkan Demir
July, 2014

Inductive heating is widely exploited in industrial operations including metal hardening, forging and brazing. Recently, as a promising alternative to traditional heating, inductive heating has attracted substantial commercial interest for domestic cookers. This is because inductive heating offers fast, precise and efficient heating compared to traditional methods that make use of either convection or conduction as a means of heat transfer. To introduce full flexibility in using the cooking space, a strong demand is currently directed toward all-surface induction ovens, with the capability to heat a vessel placed arbitrarily anywhere on the surface of the induction cook top. For this purpose, inductive coils of tens of mm in diameter are required to be designed and stacked together to form coil arrays. However, this typically comes at the cost of reduced efficiency. To address this problem, this thesis work focuses on high-efficiency coil arrays designed for all-surface induction with optimum ferrite placement. Here analytical, numerical and experimental electromagnetic analyses of sample coils are performed. Effects of different ferrite placements are investigated and, contrary to the general intuition of placing ferrite bars only under the coil, an effective way of ferrite placement is proposed and shown. These results indicate that the proposed high-efficiency arrays of inductive coils are highly promising for all-surface inductive heating.

Keywords: RF coils, coil arrays, inductive heating, all-surface induction oven.

ÖZET

YÜKSEK VERİMLİ İNDÜKTİF BOBİN DİZİNLERİ

Erdal Gönendik
Elektrik ve Elektronik Mühendisliği, Yüksek Lisans
Tez Yöneticisi: Doç. Dr. Hilmi Volkan Demir
Temmuz, 2014

İndüktif ısıtma endüstride metal döküm, prinç ile lehimleme ve demir dövmeciliğinde yaygın olarak kullanılmaktadır. Yakın geçmişte indüktif ısıtmanın ev ocaklarında kullanılmasının gelenekesel ocaklara güçlü bir alternatif teşkil etmesi, indüktif ocaklara karşı büyük bir ticari ilgi uyandırdı. Bunun nedeni indüktif ısıtmanın normal ocaklarda kullanılan konveksiyon (doğalgazli ocaklar) veya temas (elektrik rezistanslı ocaklar) yolu ile ısıtma metodlarına göre hızlı, hassas ve verimli olmasıdır. Günümüzde, gözlü indüktif ocaklarda ocak yüzeyinin tamamının esnek olarak kullanılabilmesini, diğer bir deyişle ısıtılacak tencerenin ocak yüzeyinin herhangi bir yerine konularak ısıtılmasını mümkün kılmak için tüm yüzey indüktif ocak olarak anılan yapılara doğru güçlü bir yönelim oluşmuştur. Bu amaç doğrultusunda çapları onlarca mm olan küçük bobinlerin tasarlanması ve bu bobinler ile uygun dizinler oluşturulması gerekmektedir. Fakat bu bobinlerin yanyana konulmaları ocak verimini düşüren bir etki yaratmaktadır. Bu problemi çözmek için bu tezde yüksek verimli bobin dizinleri ve bu dizinler için optimal ferrit yerleşimi üzerine yoğunlaşılmıştır. Burada bazı örnek bobinlerin analitik, sayısal ve deneysel elektromanyetik çalışmaları yapılıp, farklı ferrit yerleşimleri incelenmiştir. Genel bir kanı olan ferrit çubukların sadece bobinlerin altına yerleştirilmesinin aksine farklı ve optimal bir ferrite yerleşimi önerilmiştir. Elde edilen sonuçlar önerilen yüksek verimli bobin dizininin tüm yüzey indüktif ocaklar için umut verici olduğunu göstermektedir.

Anahtar sözcükler: RF bobinler, bobin dizinleri, indüktif ısınma, tüm yüzey indüktif ocaklar.

Acknowledgement

I would like to express my special appreciation and thanks to my advisor Professor Dr. Hilmi Volkan Demir, you have been a tremendous mentor for me. I would like to thank you for encouraging my research work and for allowing me to grow as a research scientist. Your advice on both research as well as on my career have been priceless. I would also like to thank my committee members, Professor Ayhan Altıntaş and Professor Yiğit Karpat for serving as my committee members. Many thanks to you. I would especially like to thank my colleagues Emre Ünal and Veli T. Kılıç for helping me out to build the experimental setup and fabricate the prototypes. I would like to thank Namık Yılmaz, lead design engineer at Arçelik power electronics department and all other Arçelik R&D engineers and managers for their helpful advices and discussions. Also thanks to MİKES Inc. for giving me the opportunity to study towards M.Sc.

A special thanks to my family. Words cannot express how grateful I am to my mother, father siblings for all of the sacrifices that you have made on my behalf. Your prayer for me was what kept me going thus far. I would also like to thank all of my friends who supported me in writing. This thesis work is supported by SANTEZ, for which I am very grateful and happy to acknowledge.

Contents

List of Figures

List of Tables

Chapter 1

Introduction

Induction heating technology has been used in industry in a wide variety of applications including heat treating, welding and annealing cooking among many others [1, 2]. The idea of using induction heating in domestic appliances such as induction ovens goes back to 1973 [3]. In those days domestic induction hubs were becoming popular, due to its features of safety, fast heating, high efficiency, precise control of heat transfer, and cleanliness compared to other conventional heating techniques of convection and conduction heating. Most of these features are because of the fact that the heating in induction heating occurs right in the vessel due to the eddy currents and the joules heating generated in the vessel.

In domestic induction ovens the desired heating in the metallic vessel is generated by a time-varying magnetic field. This time-varying magnetic field is generated by a planar coil powered by a power inverter. This planar turn is placed right below a metallic vessel. Domestic induction ovens typically consist of mainly three components: inductor and magnetic components, power inverter and digital controller.

The first component of an induction oven is the power converter part. Induction ovens take the energy from the mains voltage. This voltage is rectified and bus filtered to allow a high voltage ripple to get an input power factor close to one. Then the power is delivered to the inductor-load couple by varying the frequency

of the voltage using resonant inverter topologies. Most common topologies employed in induction ovens are full-bridge [4, 5], half-bridge [6–10] and two single switch inverter topologies: a ZVS one [11,12] and a ZCS one [13]. These days due to its robustness and cost savings most popular topology used is the half-bridge topology [14]. In today's research end development, this half-bridge topology is still being studied and developed to for new application specific topologies. For example, in [15–17] topologies for heating two or more loads simultaneously are reported. In [18] half-bridge topology to feed three separate concentric windings simultaneously is presented. In [19], for large signal characterization of inductive loads, a series-resonant half-bridge inverter module that delivers up to 7kW power is reported. Power converters are not the main focus of this thesis, however it is essential for a successful coil design to understand how the coil is driven.

The second component, which is the main focus of this thesis, is the induction coil and magnetic materials used with it. Induction coils transfer the electrical power delivered by the power inverter to the load by means of magnetic coupling. To deliver the power to a flat vessel more effectively, flat-type spiral windings are commonly used [20, 21]. Here external diameter of a coil is defined by the size of the burners. In other words, the size of the coil is chosen to be as large as the load intended to be used for that burner. Then, number of turns is determined depending on the inductor value required by the power inverter and maximum power desired to be delivered to the load. For efficiency considerations, the number of strands used in the coil is set to decrease the loss in the coil as much as possible [22]. Analysis of the equivalent impedance of the designed coil [23, 24] can be used as a feedback to the resonant inverter for further optimization of the system.

In today's induction ovens as mentioned above, one coil is designed for each burner on the cook top. This allows the user to put the vessel only where the burner is at. To increase the flexibility in using the surface of the cook top, all-surface induction oven has become the hot topic of domestic induction heating. In all-surface ovens, inductive coils of tens of mm in diameter are required to be designed and stacked together to form coil arrays so the the user can put the vessel anywhere s/he likes on the cook top and the vessel is heated by powering

up the coils only under the vessel. However, due to coupling effect between the coils of small diameters, the power delivery efficiency of the system is greatly reduced and this is an important problem of current all-surface induction ovens to be addressed.

The main purpose of this thesis is to design high-efficiency coil arrays to be used in all-surface induction ovens with ferrite placement. For this purpose in Chapter 2 analytical model of a simple case where one planar coil is sandwiched between a load and ferrite is derived. Using this model, effect of the ferrite is investigated. Also effect of the material properties of the load placed at different distances to the coil on the heating is investigated. In Chapter 3, numerical electromagnetic analyses of some sample coils currently used in induction ovens of different types are performed using CST Electromagnetic Studio (CST EMS), followed by experimental analyses to confirm the obtained results. In Chapter 4, performance enhancement in utilization of ferrite is investigated in detail, and comparisons of different ferrite placement is performed. With the knowledge obtained from Chapters 2-4, finally in Chapter 5 we study coil array stacking. The studied array scheme has been shown to outperform common coil arrays used today. Three patent applications have been made as a result of this thesis work.

Chapter 2

Inductive Heating

In Figure 2.1, a simple induction heating system typically used in induction ovens is shown with a planar coil and load put above it. Here the red substrate is the ferrite used to enhance the magnetic field component in the z direction. In this setup the coil is fed with a sinusoidal current to generate a sinusoidal magnetic field in the system. This magnetic field creates a time-varying magnetic flux on the bottom of the load and this forms eddy currents that heat up the load. This heating is directly proportional to the square of the current driving the coil. In a typical induction oven, the current levels are commonly in the range of 20-100 A depending on the application. As the frequency of the current driving the coil is increased, the heat generated in the load is also increased. However, due to practical limitations, the frequency of operation is commonly set around tens of kHz and usually does not exceed 100 kHz. Increasing the frequency of operation causes some practical problems. As the frequency is increased, parasitic capacitances between windings of the coil become more sound and this deteriorates the operation. In addition to this, being able to switch currents of peak values of tens of amperes at higher frequencies requires more costly transistors. In order to deliver real power to the load most efficiently, the system must be working at the resonant frequency. Thus, another practical limitation on the frequency of operation is the availability of low value power capacitors that can be used in the power electronics of such a system. To make the operating frequency higher, the

capacitance of the corresponding capacitor that the electronics will require to be using to put the system in resonance will go lower. Given a rough estimate of the inductance of the system, the only factor that determines the capacitor value to be used for resonance is the operating frequency. Larger frequencies simply require smaller capacitor values. And power capacitors with lower capacitance values are harder to find in the market. With all these considerations, the appropriate operating frequency of an induction heating system is typically in the range of 20-100 kHz; for example, a common operating frequency is 30 kHz.

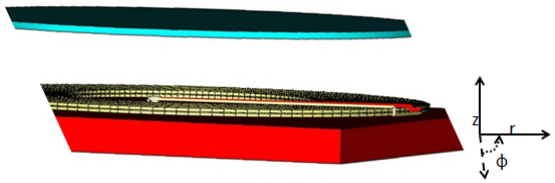

Figure 2.1: A simple induction heating system with coil (yellow), load to be heated (cyan) and ferrite substrate (red).

2.0.1 Analytical Background

Typical coil diameters in an induction oven changes in the range of 70 to 2000 mm. As discussed above, a common operating frequency is around 30 kHz. Therefore, the wavelength of the resulting fields is 10 km. Apparently, physical dimensions of the system compared to the wavelength of the fields generated in the system is very small. This validates the assumption of quasi-static solution of the Maxwell's equations. The displacement current term can be safely ignored. This conceptually means that there are not any electromagnetic waves generated by this system that propagate into the free space. Instead, there are stationary and time-varying fields in the system. With this assumption the problem is reduced to a magneto quasi-static problem. Applying Coulomb gauge condition ($\vec{\nabla}.\vec{A} = 0$), the following equations apply to this system.

$$\vec{\nabla} \times \vec{H} = \vec{J_\phi} \tag{2.1}$$

$$\vec{\nabla} \times \vec{E} = -\frac{\partial \vec{B}}{\partial t} \tag{2.2}$$

$$\vec{\nabla} \times \vec{A} = \vec{B} \tag{2.3}$$

where $\vec{E}$ is the electric field vector, $\vec{H}$ is the magnetic field strength vector, $\vec{A}$ is the vector potential, $\vec{B}$ is the magnetic field and $\vec{J}_\phi$ is the volumetric current density in a circular winding.

Electromagnetic problem of a typical system used in induction ovens can be represented as shown in Figure 2.2. This shows the most general case for a filamentary turn used in a coil. If we analytically calculate the fields as a result of a single filamentary turn in six regions shown in the above figure, we can use superposition to calculate the final field distribution in the system by vectorially summing up the fields generated by each filamentary turn. Although here by applying superposition, we assume that the system is linear. In magnetic materials, such as the ferrite or the load with magnetic properties, there can occur two types of nonlinearities. These are magnetic hysteresis and saturation. In domestic pots normally soft magnetic materials are used with very little residual magnetization and, as a result, magnetic hysteresis can be ignored. Secondly, in induction ovens there always occurs a flux reduction due to induced currents in load and usually the material works far off its saturation point. Also in this thesis work, during the experiments where we used aluminum as the load we did not feed the coil with very high current levels (below 20 A). As a result magnetic saturation can also safely be ignored.

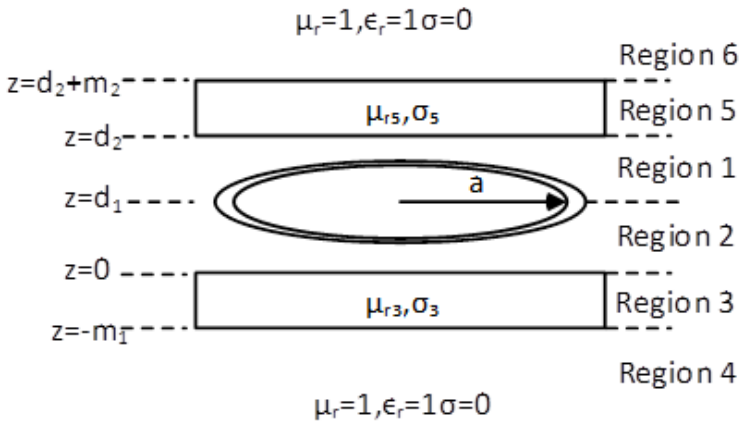

Figure 2.2: A filamentary turn between two finite thickness substrate of certain material properties.

The procedure that will be followed here to analytically solve the electromagnetic problem depicted in Figure 2.2 is carried out in [25] for the infinite substrate. The method in [25] is the same method as we use here, which is based on the Fourier-Bessel integral transformation. In [26] and [27], inductive components of the filamentary formulas are derived using the method of images. An alternative method is used in [28] for infinite substrate utilizing magnetic vector potential. Another method that uses magnetic vector potential is [29]. In [29], each of the substrates is defined to possess a finite thickness and many layers of materials are defined both above and below the filamentary turn. Our approach to the problem is also given in [30]. Here we further elaborated on the results of [30] for different regions given in Figure 2.2 and implemented the closed form solutions of the fields in these regions using MATLAB.

We assume that the filamentary turn with radius a at $z = d_1$ carries a sinusoidal current $i_\phi = I_\phi e^{jwt}$. The solution of the Maxwell's equations must be considered in six different regions as shown in Figure 2.2. Due to cylindrical symmetry of the problem we use cylindrical coordinates. Since the only external source in the system is in the ϕ-direction, we do not expect to see a magnetic field in the ϕ-direction, besides since the problem is considered to be magneto quasi-static and displacement current term in Maxwell's equations is ignored, the only electric field we expect to see in the system is in the ϕ-direction. On the basis of cylindrical symmetry following identities hold for the electric field and the magnetic field.

$$H_\phi = 0, \frac{\partial H_r}{\partial \phi} = 0, \frac{\partial H_z}{\partial \phi} = 0, E_r = 0, E_z = 0, \frac{\partial E_\phi}{\partial \phi} = 0 \tag{2.4}$$

After these observations, Maxwell's equations reduce to the following equations in each region.

Region 1 ($d_1 \leq z < d_2$): Utilizing the set of equalities given in Eq. (2.4) and noticing that the only current source in the system is in the ϕ-direction, Eqs. (2.1) and (2.2) boil down to:

$$\frac{\partial H_r}{\partial z} - \frac{\partial H_z}{\partial r} = I_\phi \delta(r-a)\delta(z-d_1)$$

$$\frac{\partial E_\phi}{\partial z} = jw\mu_0 H_z$$

$$\frac{1}{r}\frac{\partial(rE_\phi)}{\partial r} = -jw\mu_0 H_z \tag{2.5}$$

Eliminating H gives the following equation for the only component of the electric field in the system.

$$\frac{\partial^2 E_\phi}{\partial z^2} - \frac{\partial^2 E_\phi}{\partial r^2} + \frac{1}{r}\frac{\partial E_\phi}{\partial r} - \frac{E_\phi}{r^2} = jw\mu_0 I_\phi \delta(r-a)\delta(z-d_1) \tag{2.6}$$

Region 2 ($0 \leq z < d_1$): There is no current in this region, so equations obtained for Region 1 can be simplified into the following equation for this region:

$$\frac{\partial^2 E_\phi}{\partial z^2} - \frac{\partial^2 E_\phi}{\partial r^2} + \frac{1}{r}\frac{\partial E_\phi}{\partial r} - \frac{E_\phi}{r^2} = 0 \tag{2.7}$$

Region 3 ($-m_1 \leq z < 0$): In this region there is current due to the conductivity of this region ($J_\phi = \sigma E_\phi$), so the equation for E_ϕ in this region is reduced to the following:

$$\frac{\partial^2 E_\phi}{\partial z^2} - \frac{\partial^2 E_\phi}{\partial r^2} + \frac{1}{r}\frac{\partial E_\phi}{\partial r} - (\frac{1}{r^2} + jw\mu_0\mu_{r_3}\sigma_3)E_\phi = 0 \tag{2.8}$$

Region 4 ($z < -m_1$): This region has no current thus, the simplified equation for E_ϕ in this region is exactly the same as in Region 2.

Region 5 ($d_2 \leq z < d_2 + m$): Equation for this region is identical to the one we derived for Region 3, except that the material properties are different in this region. Therefore, the equation for E_ϕ in this region is given as follows:

$$\frac{\partial^2 E_\phi}{\partial z^2} - \frac{\partial^2 E_\phi}{\partial r^2} + \frac{1}{r}\frac{\partial E_\phi}{\partial r} - (\frac{1}{r^2} + jw\mu_0\mu_{r_5}\sigma_5)E_\phi = 0 \tag{2.9}$$

Region 6 ($d_2 + m_2 \leq z$): Equation for E_ϕ in this region is similar to the ones in Regions 2 and 4 and is given simply as in Eq. (2.7).

At this point, we are required to solve Eqs. (2.5) through (2.9). Once we solve these equations and obtain E_ϕ, we can find all the fields in each region. To simplify equations given above, we use Fourier-Bessel integral transformation given as:

$$E_\phi^* = \int_0^\infty E_\phi(r,z) r J_1(kr) dr \tag{2.10}$$

In Eq. (2.10), $J_1(kr)$ represents the Bessel function of the first kind of order one. $E^*_\phi(k,z)$ is the transformed form of E_ϕ. For the sake of simplicity, we will denote $E^*_\phi(k,z)$ simply as E^*. With this transform applied, Eq. (2.6) transforms into the following:

$$\frac{d^2E^*}{dz^2} = k^2E^* + jw\mu_0 I_\phi a J_1(ka)\delta(z-d_1) \tag{2.11}$$

The solution of this equation in Region 1 is in the form of :

$$E^* = Ae^{kz} + Be^{-kz} \tag{2.12}$$

Note that this solution form also applies to Regions 2, 4 and 6.

In Regions 3 and 5 we have induced currents. So, applying Fourier-Bessel integral transformation to Eqs. (2.8) and (2.9), we obtain the following equations, respectively:

$$\frac{d^2E^*}{dz^2} = (k^2 + jw\mu_0\mu_{r_3}\sigma_3)E^* \tag{2.13}$$

$$\frac{d^2E^*}{dz^2} = (k^2 + jw\mu_0\mu_{r_5}\sigma_5)E^* \tag{2.14}$$

Solutions of the equations above are in the form of:

$$E^* = Ee^{\eta_3 z} + Fe^{-\eta_3 z} \tag{2.15}$$

$$E^* = Ke^{\eta_5 z} + Le^{-\eta_5 z} \tag{2.16}$$

where $\eta_5 = \sqrt{(k^2 + jw\mu_0\mu_{r_5}\sigma_5)}$ for Region 5 and $\eta_3 = \sqrt{(k^2 + jw\mu_0\mu_{r_3}\sigma_3)}$ for Region 3.

Below is the summary of solutions for E^* in each region:

$$\textit{Region 1 } (d_1 \le z < d_2) \qquad :E^* = Ae^{kz} + Be^{-kz} \tag{2.17}$$

$$\textit{Region 2 } (0 \le z < d_1) \qquad :E^* = Ce^{kz} + De^{-kz} \tag{2.18}$$

$$\textit{Region 3 } (-m_1 \le z < 0) \qquad :E^* = Ee^{\eta_3 z} + Fe^{-\eta_3 z} \tag{2.19}$$

$$\textit{Region 4 } (z < -m_1) \qquad :E^* = Ge^{kz} + He^{-kz} \tag{2.20}$$

$$\textit{Region 5 } (d_2 \le z < d_2 + m_2) \qquad :E^* = Ke^{\eta_5 z} + Le^{-\eta_5 z} \tag{2.21}$$

$$\textit{Region 6 } (d_2 + m_2 \le z) \qquad :E^* = Ie^{kz} + Me^{-kz} \tag{2.22}$$

At first glance one can say that $H = 0$ and $I = 0$ since fields must vanish as z goes to negative and positive infinity. The electric field is also continuous at the boundaries of z = $-m_1$, 0, d_1, d_2, $d_2 + m_2$. Equating E^* at the boundaries result in the following set of equations:

$$Ee^{-\eta_3 m_1} + Fe^{\eta_3 m_1} = Ge^{-km_1} \tag{2.23}$$

$$C + D = E + F \tag{2.24}$$

$$Ae^{kd_1} + Be^{-kd_1} = Ce^{kd_1} + De^{-kd_1} \tag{2.25}$$

$$Ae^{kd_2} + Be^{-kd_2} = Ke^{\eta_5 d_2} + Le^{-\eta_5 d_2} \tag{2.26}$$

$$Ke^{\eta_5(d_2+m_2)} + Le^{-\eta_5(d_2+m_2)} = Me^{-k(d_2+m_2)} \tag{2.27}$$

We have ten unknowns and five equations above. The other five equations come from the continuity of H_r. H_r is simply given by:

$$H_r = \frac{1}{jw\mu_r\mu_0}\frac{\partial E^*}{\partial z} \tag{2.28}$$

Since E^* depends on z only, the exponent derivative of E^* with respect to z can easily be taken. As a result, from the continuity of H_r at the boundaries where there are no surface currents at $z = -m_1, 0, d_2, d_2 + m_2$ we arrive at the following set of equations:

$$k(C - D) = \frac{\eta_3}{\mu_{r_3}}(E - F) \tag{2.29}$$

$$\frac{\eta_3}{\mu_{r_3}}(Ee^{-\eta_3 m_1} - Fe^{\eta_3 m_2}) = kGe^{-km_1} \tag{2.30}$$

$$k(Ae^{kd_2} - Be^{-kd_2}) = \frac{\eta_5}{\mu_{r_5}}(Ke^{\eta_5 d_2} - Le^{-\eta_5 d_2}) \tag{2.31}$$

$$\frac{\eta_5}{\mu_{r_5}}(Ke^{\eta_5(d_2+m_2)} - Le^{-\eta_5(d_2+m_2)}) = -kMe^{-k(d_2+m_2)} \tag{2.32}$$

One last equation comes from the boundary where we have the filamentary turn carrying the source current at $z = d_1$. H_r can be easily found using E^* from Eq. (2.28). The boundary condition for H_r at the boundary $z = d_1$ is given by:

$$\vec{n} \times (\vec{H}_{1r} - \vec{H}_{2r}) = \delta(r - a)I_\phi \tag{2.33}$$

Here $\vec{n}$ is the vector normal to the plane of boundary. $\vec{H}_{1r}$ and $\vec{H}_{2r}$ are radial components of magnetic field in Region 1 and Region 2, respectively. Here we

have the Fourier-Bessel transforms of E^* at hand in both Region 1 and 2. Using Eq. (2.28) we obtain the transform of $(\vec{H}_{1r} - \vec{H}_{2r})$. To use Eq. (2.33), we need to take the transform of $\delta(r-a)I_\phi$, which is indeed given as $I_\phi a J_1(ka)$. So, the final boundary equation is found to be given as in Eq. (2.34).

$$Ae^{kd_1} - Be^{-kd_1} - Ce^{kd_1} + De^{-kd_1} = \frac{jw\mu_0}{k} I_\phi a J_1(ka) \tag{2.34}$$

Now we have ten unknowns of $A, B, C, D, E, F, G, K, L, M$ and ten equations given by Eq. (2.23) to (2.27) and (2.29) to (2.34). The solution of this set of equations gives us E^* in each of 6 regions. From here H_r can easily be obtained using Eq. (2.28). The third field in the system, B_z, can also be easily calculated using the equality:

$$B_z = \frac{1}{-jw}[\frac{E^*}{r} + \frac{\partial E^*}{\partial r}] \tag{2.35}$$

Finally for the transformed fields we need to take the inverse Fourier-Bessel Integral transform given by Eq. (2.36).

$$E = \int_0^\infty E^*(k) k J_1(kr) dk \tag{2.36}$$

A MATLAB program was written to solve this set of equations. This program can compute any field in any region given the parameters including driving current level, frequency of operation, coil size, number of turns, diameter of each turn, turn separation, $\mu_{r_5}, \sigma_5, \mu_{r_3}, \sigma_3$, thicknesses of both load and ferrite, and distance of the coil from load and/or ferrite. Also impedance of the system can be calculated so that inductance and resistance of the system are analyzed under different circumstances. This analytical solution helps us a lot to understand the behavior of the system. We can see how the system reacts to different types of loads and ferrite and how load and ferrite thicknesses affect the system. We can understand dependence of fields on the number of turns and coil sizes and also we have an idea of the inductance and resistance change of the system under different conditions. Below some simulation results are discussed. The effect of ferrite will further be more extensively discussed in Chapter 4. the following MATLAB runs were performed for a coil of 24 turns with a wire diameter of 1.3 mm. The inner radius of the coil is 25 mm and the outer radius of the coil is 88 mm. The

coil was driven with 30 A sinusoidal current. Figure 2.3 shows B_z at different distances from the coil when the coil was driven at 50 kHz without any load or ferrite .

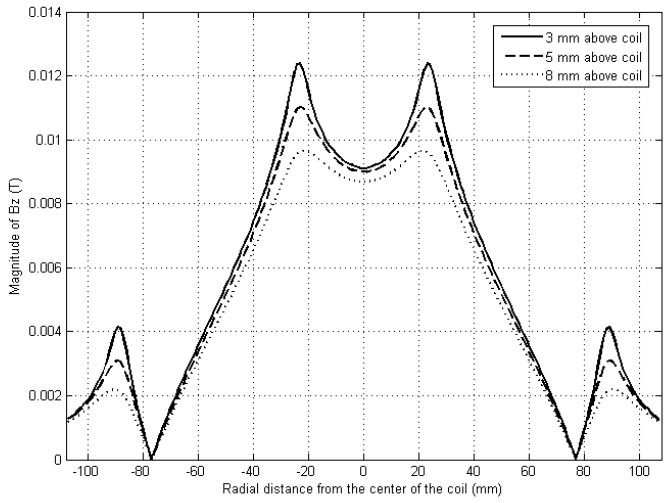

Figure 2.3: Magnitude of the magnetic field in z direction at different distances from the coil. The coil is unloaded and no ferrite is used.

It is apparent from Figure 2.3 that, as the distance from the coil increases, the magnetic field in the z-direction gets smaller in magnitude. B_z is the only component of the fields in the system that creates a changing magnetic flux on the bottom of the vessel i.e., this is what heats up the load by induction and joule heating. This means that if the electronics of the system is capable of providing the coil with a constant current regardless of the impedance of the system, then the load should be put as close to the coil as possible. Couple of other important points that can be observed from Figure 2.3 is that the magnetic field peaks are located where the first turn starts at a distance of approximately 25 mm from the center of the coil in this case. The field then gradually decreases as we further move through other turns. At the 20^{th} turn, the magnetic field sums up to zero and further down the way it starts to peak with a phase difference of 180°, i.e., the magnetic field after the 20^{th} turn is pointing down in the $-z$-direction whereas the magnetic field up to the 20^{th} turn points in the $+z$-direction.

In Figure 2.4, the magnitude of the magnetic field in the r-direction is shown.

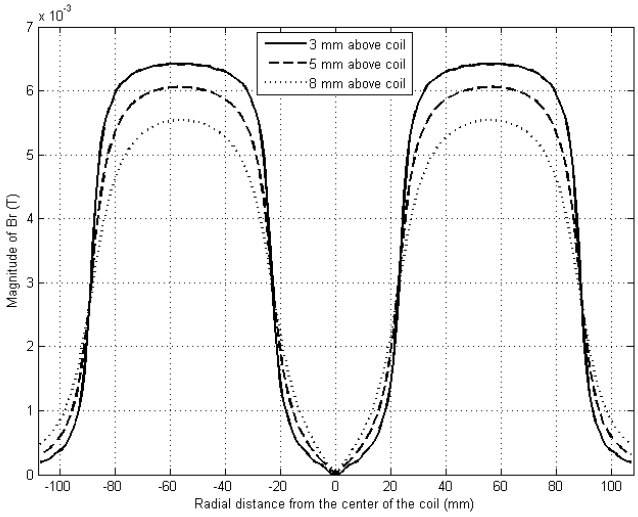

Figure 2.4: Magnitude of the magnetic field in the r-direction for different distances from the coil.

This component of the magnetic field does not contribute to the heating of the load since it does not create any changing flux in the load. Although the load has some finite thickness, its heating caused by B_r due to this finite thickness is negligible because this thickness is usually on the order of a couple of mm's. Here also B_r decreases as we move further away from the coil. B_r stays quite constant throughout the coil turns. Once the coil ends at around $r = 88$ mm B_r decays away very fast. This means, induction ovens would not cause any harm to the surrounding in the r-direction. In the z-direction, since there will always be a load while the system is running, due to the skin effect no field would be present above the load.

Figure 2.5 shows the electric field in the ϕ-direction. As expected E_ϕ decreases as the distance from the coil is increased. This field peaks at the 14^{th} turn and gradually decreases from there. Heating of the bottom of the load can also be thought to be caused by this E_ϕ. Actually this is what causes eddy currents in the load. Looking at Figure 2.5 E_ϕ at $d = 3$ mm is quite larger than E_ϕ at $d = 8$ mm. This means that the load placed at $d = 3$ mm would be heated more than the load at $d = 8$ mm. The eddy current where E_ϕ peaks at about 60 mm away from the center of the coil would be the strongest. This implies that heating

pattern of the coil will be in circles and heating will first start around the circle with radius of 60 mm for this specific case.

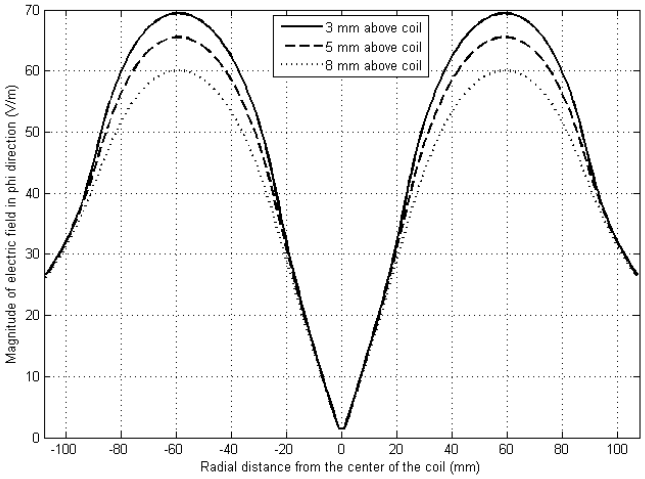

Figure 2.5: Magnitude of electric field in the ϕ-direction.

Figure 2.6 shows the magnitude of B_z when the coil is driven at 100 kHz. As it is obvious from this figure the fields do not depend on the frequency of operation when the coil is not loaded. Results in Figure 2.6 are exactly the same as results of Figure 2.3. However, as it will be analyzed later, when the coil is loaded, the frequency of operation matters. Increasing frequency will increase the loss in the load as it would increase the magnetic flux change on the bottom of the load.

Figure 2.7 shows B_z when a ferrite of 2 mm in thickness and $\mu_r = 500$ is placed 5 mm under the coil. In this case the coil is still not loaded with a vessel load and the operating frequency is at 50 kHz. When we compare Figure 2.3 with Figure 2.7 we observe the dramatic increase in the magnitude of B_z. We can conclude that adding ferrite under the coil would increase the efficiency of the system because with the same amount of current one would expect more heating in the load or with less current one would reach the same level of heating compared to the case without ferrite. Effects of ferrite in induction heating will be analyzed in detail in Chapter 4 and, as a result of this analysis, optimum placement of ferrite will be determined.

In Figure 2.8, the magnitude of B_z when the coil is loaded with three different

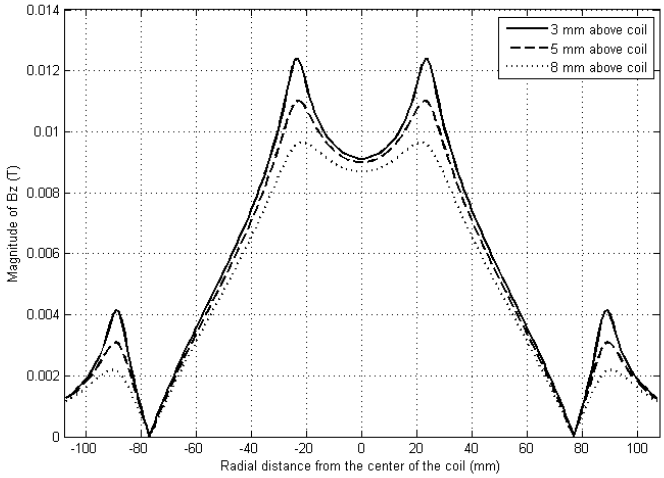

Figure 2.6: Magnitude of B_z at different distances from the coil when the coil is driven at 100 kHz.

materials of load is shown. All loads are taken to be 2 mm in thickness and are placed 3 mm above the coil and the rest of the parameters used in the simulation are the same as the previous ones. Here simulations were carried out with and without ferrite and effect of the ferrite is obvious in the plots. The three types of loads used in the simulations are made of aluminum with $\sigma = 3.538 \times 10^7 \Omega^{-1} m^{-1}$ and $\mu_r = 1$, copper with $\sigma = 5.96 \times 10^7 \Omega^{-1} m^{-1}$ and $\mu_r = 1$ and ferromagnetic steel $\sigma = 1.67 \times 10^6 \Omega^{-1} m^{-1}$ and $\mu_r = 200$. Since using ferromagnetic steel acts like a ferrite with electrical loss, it further enhances the magnetic field between the coil and the load substantially compared to the aluminum and copper loads.

Figure 2.9 shows the electric field in the ϕ-direction when the coil is loaded with the three loads mentioned above. This figure tells us that the electrical loss (ohmic heating) in the ferromagnetic steel would be the highest. A very close look at Figure 2.9 reveals that the electrical loss in aluminum would be slightly larger than that in copper. This is because copper has a larger conductivity than the aluminum. Thus, aluminum has a larger resistance which results in a slightly larger electrical loss.

An other point is that, when we look at the pattern of E_ϕ in Figure 2.9, we

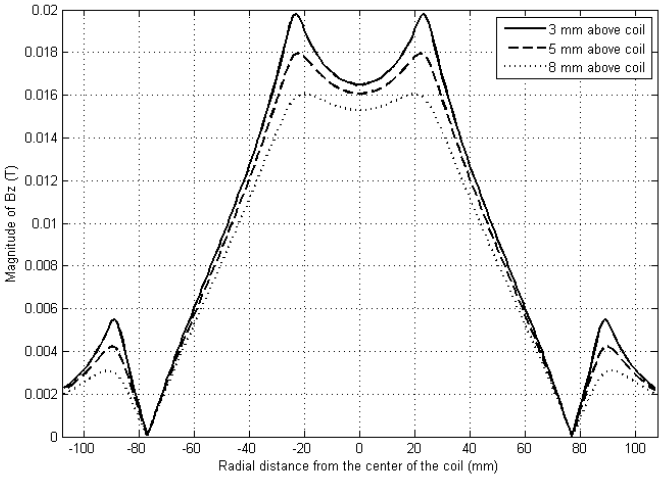

Figure 2.7: Magnitude of B_z when the ferrite is placed under the coil.

observe that E_ϕ is high in the r-direction only where coil turns exist and decays sharply when turns end. This means that the heating in the load would be just like an image of the coil under it, i.e., the eddy currents flowing in the load takes the shape of the coil turns. This tells us, that if we would like to have a homogeneous heating in the load, the inner radius of the coil should approach to zero and the outer radius of the coil should exactly match the size of the load to be heated.

Finally, when we compare B_z at $d = 3$ mm in Figure 2.3 with B_z in Figure 2.8a for ferromagnetic steel, we see that the peak value of B_z drops by 18%. This is due to the opposing magnetic field in the -z-direction created by the eddy currents generated in the load. Loading the coil also increases the amplitude of the valley depth from 32.59 to 36.32 G.

In this part, to understand the operation of an induction heating system we have analytically solved Maxwell's equations and obtained expressions for each field of interest in the system. We have discussed how the fields change over distance across and away from the coil and with the frequency. Also we briefly mentioned the effect of using ferrite on the fields. Loading the coil with different types of materials change the efficiency of the system. Since ferromagnetic materials act like a ferrite with strong electrical loss on them, they form a magnetic

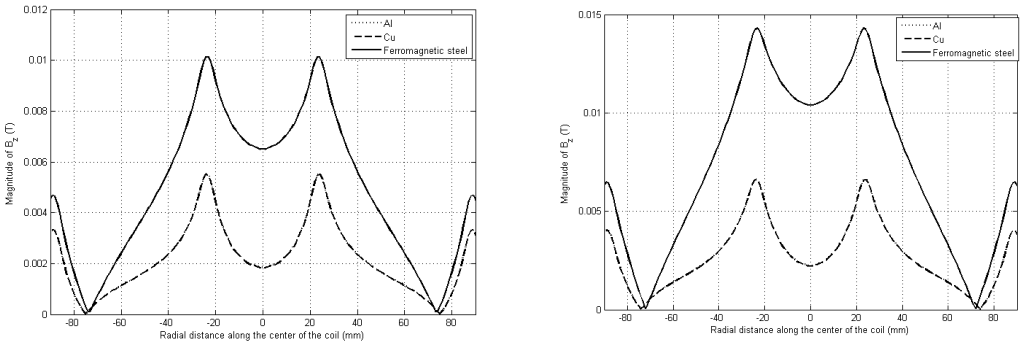

(a) (b)

Figure 2.8: Magnitude of B_z for three different loads (a) without ferrite and (b) with ferrite.

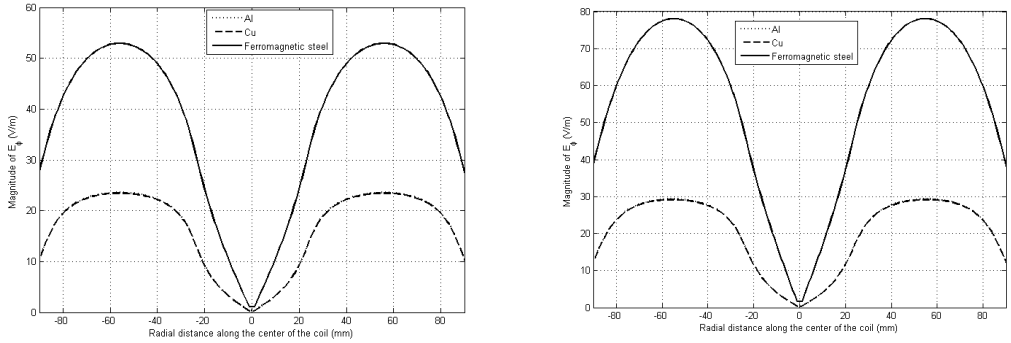

(a) (b)

Figure 2.9: Magnitude of E_ϕ for three different loads (a) without ferrite, (b) with ferrite.

cavity for the coil and enhance magnetic fields in the system drastically, which in turn increases the efficiency of the system. Loads without magnetic properties like aluminum or copper do not form a magnetic cavity like ferromagnetic steel does; thus, it is harder to heat these materials compared to ferromagnetic steel. To heat these materials more current has to be driven into the system, which decreases the efficiency of the overall system.

Chapter 3

Electromagnetic Analyses of Coils for Inductive Heating

3.1 Numerical and Experimental Magnetic Analysis of Coils

Analytical study presented in Chapter 2 gives us an insight about how the induction oven system works; however it has some shortcomings. First of all we model the wires as filamentary. Therefore the MATLAB simulations implementing the analytical model do not take the wire thickness into account. Secondly, the structure shown in Figure 2.2 represents a very general situation. Most of the time, coils with ferrite and load have more complex shapes and it is very hard to model such systems analytically even if it might be possible. To overcome these shortcomings we took a numerical approach using CST Electromagnetic Studio (CST EMS) to perform our simulations. In the rest of this thesis, unless otherwise stated, all numerical simulation results are obtained using CST EMS. To confirm these simulation results, we also built an experimental setup to measure the magnetic fields of different coils under loaded and unloaded conditions.

In the next part, the experimental setup for the magnetic measurements will

be described with the methodologies developed and used both in simulations and measurements. We also performed magnetic analyses of five different types of coils currently used in induction ovens. In the next part, both numerical simulations and experimental measurements of these coils will be discussed.

3.1.1 Experimental Setup and Measurement Methodology

To measure the magnetic field in the z-direction we constructed a measurement setup as shown in Figure 3.1. This setup consists of a single turn pickup coil of 1 cm in diameter that is used to measure the magnetic field in the z-direction,along with a function generator, a power amplifier, an oscilloscope to measure the volt-

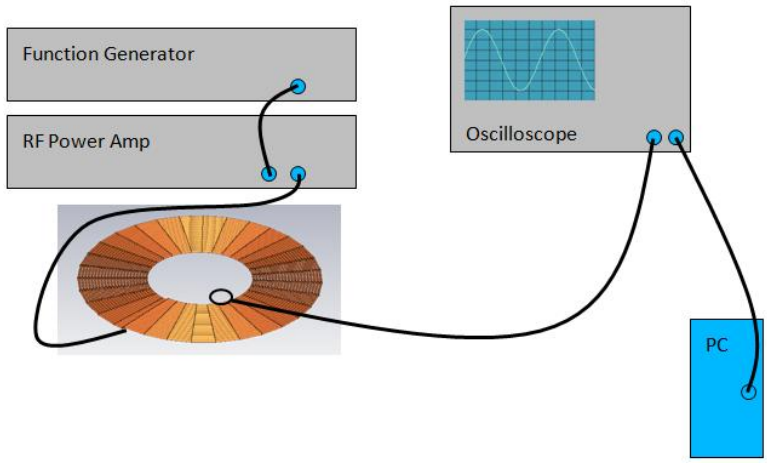

Figure 3.1: Measurement setup.

age induced in the pickup coil, a pc to process the data taken by the oscilloscope and to control xyz stage that allows us to move the pickup coil in 3D with a sensitivity of 50 μm.

In this setup, the function generator provides the power amplifier with a single tone signal at the desired amplitude and frequency. This signal is amplified in the power amplifier and fed to the coil. This creates a time-varying magnetic field in the system and this magnetic field induces a voltage in the pickup coil. This voltage value is read by the oscilloscope and transferred to the computer

using a MATLAB code. With the help of this code, xyz stage movement can also be controlled very precisely. During the measurement, the xyz stage moves continuously on a predefined path while taking continuous measurements of induced voltage in the pickup coil. This way we obtain the magnetic field distribution (magnetic field map) of the system. With this setup we could load the coil with a load at any distance from the coil and still measure the magnetic field distribution between the coil and the load.

The voltage induced in the pickup coil is directly proportional to the frequency of operation, magnetic field amplitude at that location and the area of the pickup coil. Therefore, this voltage value gives us a very good idea about the magnetic field in the z-direction around pickup coil location. By changing the direction that the pickup coil looks, we could also measure the magnetic field in the r-direction in principle. However, here what we focus on is B_z because this component is what heats up the load. The frequency of operation for the coil is very far away from the resonant frequency of the pickup coil, which is in MHz range. Thus, the measurements we took here are not distorted by the resonance of the pickup coil. With this setup we have take two different types of measurements. One is

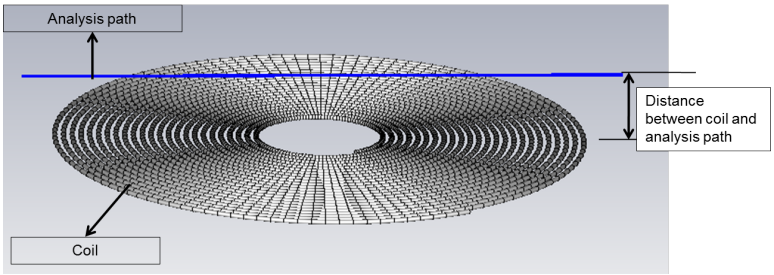

Figure 3.2: Measurement technique I.

based on taking the measurement along a line above the coil at a certain distance from it as shown in Figure 3.2. The line along which we took the measurements goes through the center of the coil. The second measurement method is based on tracing the whole surface scan. As shown in Figure 3.3, the magnetic field on a plane parallel to the plane of coil and at any distance desired above it was measured and the result of this measurement is obtained as a surface plot.

As we mentioned above, the voltage induced in the pickup coil is directly

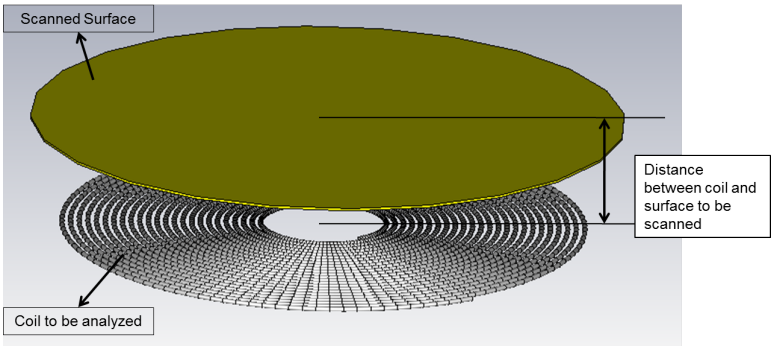

Figure 3.3: Measurement technique II.

proportional to B_z at the pickup coil location. To validate this assumption we compared the magnetic field that we measured using a Hall probe with the voltage induced in the pickup coil. For this measurement we used standard 24-turn coil coil 1 with a diameter of 180 mm (a product of Arelik). We derived the coil with a sinusoidal signal at 50 kHz. The coil was unloaded and no ferrite was used during this test. We measured the magnetic field 1 mm above the coil using the first measurement technique. While taking this measurement we also placed the Hall probe to make sure that it only reads magnetic field in the z-direction. The results are shown in Figure 3.4. In this figure the left y-axis is in volts and shows

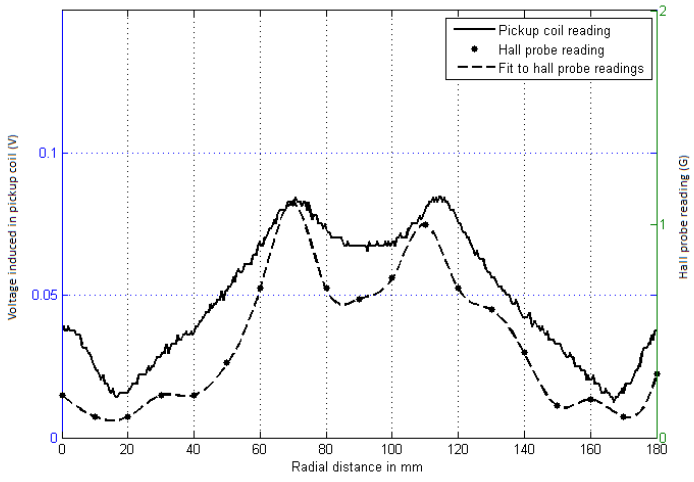

Figure 3.4: Voltage induced in the pickup coil in V (left y axis) and hall probe reading in gauss (right axis).

the pickup coil reading whereas the right y-axis show the Hall probe reading in

G (10^{-4} T). It is obvious that these two measurements are consistent and this validates our measurement method. However, if it is desired to measure the exact absolute value of the magnetic field at a point very precisely, new methods need to be adapted. In this thesis, we are interested in the dependence of magnetic field in the z-direction on various parameters rather than its absolute value. Therefore, these measurement methods fulfill our requirements. Both of the measurement techniques above can be used for both loaded and unloaded coils. Using these two techniques of measurements, we analyzed different types of coils used in induction ovens and the results are discussed in detail in the next section.

At every analysis the impedance of the system is measured using an LCR meter. LCR meters measure the impedance of the system with small signal excitations. These measurements give quite a good idea about the behavior of the system however in practice what is usually required is the impedance of the system when the coil is fed with tens of amperes current.In [31] a test bench is designed to characterize the coils used for induction under high signal excitations and differences between LCR measurements and high signal excitation result are observed due to nonlinearity of the system under high signal condition. In this thesis LCR measurements are sufficient to make our point.

3.1.2 Case study: Coil 1 (circular cross-section coil)

In this part, the magnetic analysis of a 24-turn 180 mm-diameter coil (Coil 1) shown in Figure 3.5 is performed. This coil is utilized in some of the induction ovens (used by Arelik). This coil has an inner diameter of 45 mm. The copper wires used for the windings have circular cross sections and have a thickness of about 2.5 mm. As we mentioned before, what we care about in these measurements and simulations is the magnetic field in the z-direction. Due to the symmetry of the system in the ϕ-direction, we will mostly use the measurement technique I. Measurement technique II is also used from time to time to see the whole magnetic field map of the coil.

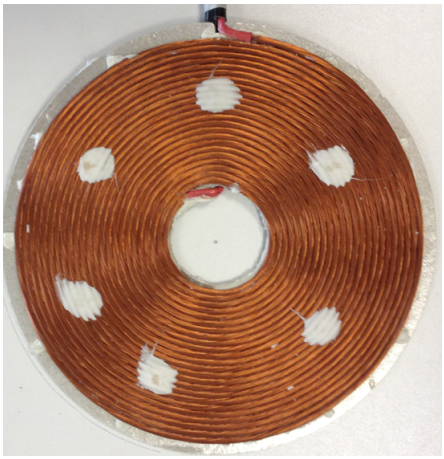

Figure 3.5: Front picture of Coil 1.

3.1.2.1 Unloaded Measurements and Simulations of Coil 1

In this part we performed simulations and measurements to analyze B_z of the coil without any load above it. In both measurements and simulations, the coil is fed at 100 kHz with a 100 V_{rms} sinusoidal voltage source. The measurements and simulations were carried out at three different distances from the coil. Figure 3.6

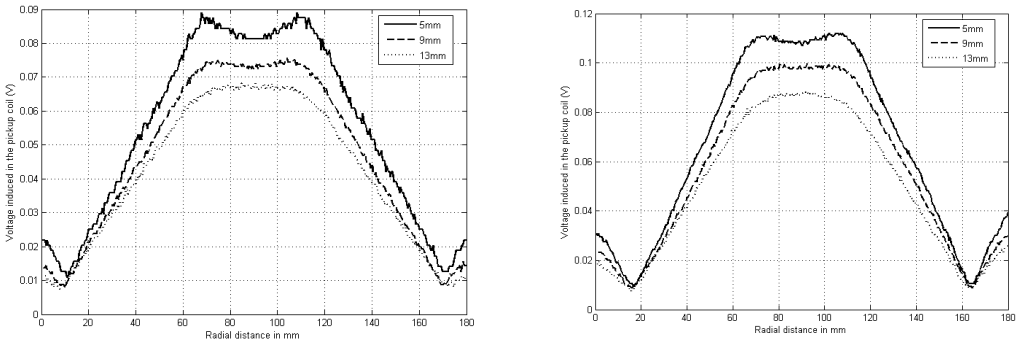

(a) (b)

Figure 3.6: Measurement results of B_z at different distances from unloaded Coil 1 (a) without ferrite and (b) with ferrite.

shows the magnetic field in the z-direction with and without ferrite. In measurements, we used ferrite bars of dimensions (5 mm $\times$ 15 mm $\times$ 60 mm) and we placed 8 of these bars under the coil. All ferrite bars were positioned aligning the longest dimension with the diameter of the coil, all pointing towards the center

of the coil and with the shortest dimension being perpendicular to the plane of the coil.

The measurement results are quite consistent with the results of the MATLAB simulations. As we further move away from the coil, the magnitude of B_z decreases as expected. Here B_z with the ferrite is about 22% larger than the case without the ferrite. The possible improvement with the ferrite is actually more than this, as we will examine in detail in Chapter 4. The reason why we obtain only a 22% improvement is due to how we feed the coil. We could drive the coil only with a constant voltage in this case. Putting ferrite under the coil increases its inductance. Without the ferrite, inductance of the coil is measured to be 59.12 μH. With ferrite bars, the inductance went up to 80 μH. The resistance of the system is due to only the resistance of the coil which is around 88 $m\Omega$. Thus, this resistance can simply be ignored in impedance calculation. Adding ferrite increased the impedance of the system by 35%, which means coil with ferrite drew 35% less current from the source since the voltage is constant. Smaller current results in smaller B_z and this limits the improvement of ferrite to only 22%. If the coil was driven with a constant current source in both cases, the improvement in B_z due to the utilization of ferrite would be around 29%.

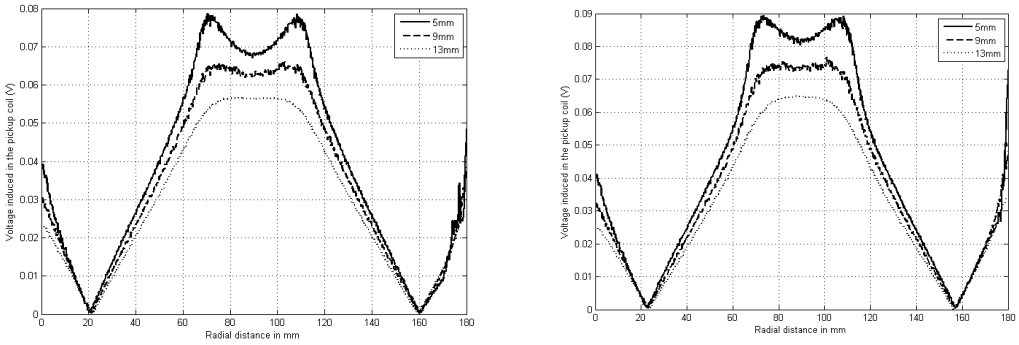

(a) (b)

Figure 3.7: Simulation results of B_z at different distances from unloaded Coil 1 (a) without ferrite and (b) with ferrite.

Figure 3.7 shows the CST EMS simulation results of the measurements above. The numerical results are quite consistent with the measurements. Ferrite bars

in the simulation were modeled with a μ_r value of 300. The gain in B_z in this case is only 12.5%. This discrepancy in the improvement is due to the real value of μ_r of the ferrite. It is most probably above 500.

Magnetic field makes a dip towards the center of the coil where there are no turns as it is obvious from the plots above. The depth of this dip gets smaller as we move away from the coil in the z-direction. As seen in Figure 3.7, B_z gets smoother around the center of the coil as the distance from the coil is increased from 5 to 13 mm. As the distance between the load and the coil is increased the effect of eddy currents to decrease the B_z in between load and coil is also decreased which results in higher inductance. This inductance change with respect to distance of the load to the coil is utilized in [32] to increase the efficiency of the power converter of the induction system.

One difference between the measurement and simulation results is that in simulations B_z towards the center of the coil makes a sharper dip than B_z in the measurements. This is because of the averaging that the pickup coil does due to its finite size during the measurement. Since the pickup coil has a finite area, it sees all the magnetic flux coupled to its area. Therefore, instead of measuring B_z at a single point in space, it measures the sum of B_z at all points inside its surface area. Being aware of this fact, this measurement technique still gives us an idea about the form of B_z.

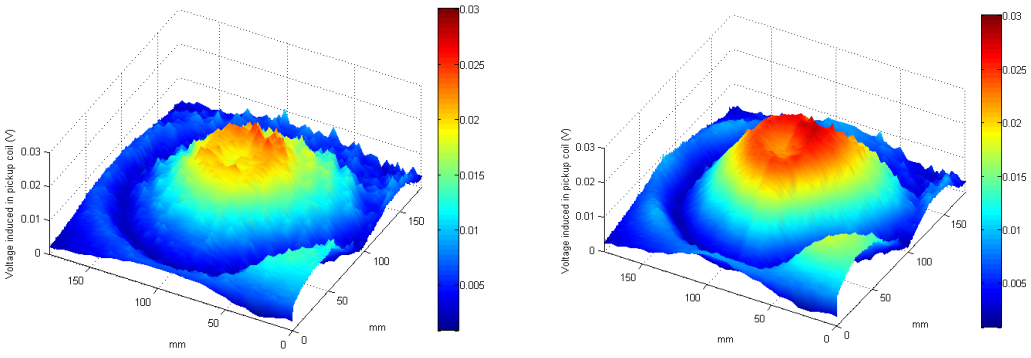

(a) (b)

Figure 3.8: All surface scan of B_z at 5 mm above unloaded Coil 1 (a) without ferrite and (b) with ferrite.

Figure 3.8 shows the all-surface scan of B_z performed using measurement technique II in Figure 3.3. Here the measurement was taken 5 mm above the coil. The symmetry of B_z in the ϕ-direction is obvious in these plots. The magnetic field around the intersection of the x and y-axes is quite large in both Figure 3.8a and 3.8b. That is where the cable goes into the coil to make the first turn.

As a result, as we move away from the center of the coil in the $+z$-direction, the magnitude of B_z decreases and becomes smoother especially in the center of the coil. We like to put the load as close to the coil as possible to heat it more efficiently.

3.1.2.2 Loaded Measurements and Simulations of Coil 1

In this part, Coil 1 is loaded with four different types of load (ferromagnetic steel, aluminum, copper, and non-ferromagnetic steel). All of the loads are 1 mm in thickness, 180 mm in diameter and placed about 15 mm above the coil. The measurements are taken between the load and the coil at three different distances from the coil, as seen in Figure 3.9. Ferrite bars used is about 5 mm in thickness and 8 ferrite bars are placed under the coil symmetric in the ϕ-direction. The coil is driven at 50 kHz with a 100 V_{rms} sinusoidal signal. Here we will only mention the results of ferromagnetic steel and aluminum since these load types are enough to make our point. The ferromagnetic steel we used in this measurement is of type 430 with $\sigma = 1.67 \times 10^6\ \Omega^{-1}m^{-1}$ and a μ_r value of 600 - 1100. The aluminum we used has $\sigma = 3.538 \times 10^7\ \Omega^{-1}m^{-1}$ and $\mu_r = 1$.

In Figure 3.9, B_z in the case of using the ferromagnetic steel load is shown. Effect of the ferrite can be seen comparing the impedance of the system with and without ferrite. The impedance of the system with the ferrite is $9.93 + j15.41\ \Omega$ whereas it is $7.89 + j14.33\ \Omega$. The increase in the impedance is 12.1%. Thus, the current drawn by the coil is decreased by this amount. That is why the increase in B_z in Figure 3.9 is not as much as the increase in the inductance of the system when the ferrite is used. Here the ferrite increased B_z by about 35%,

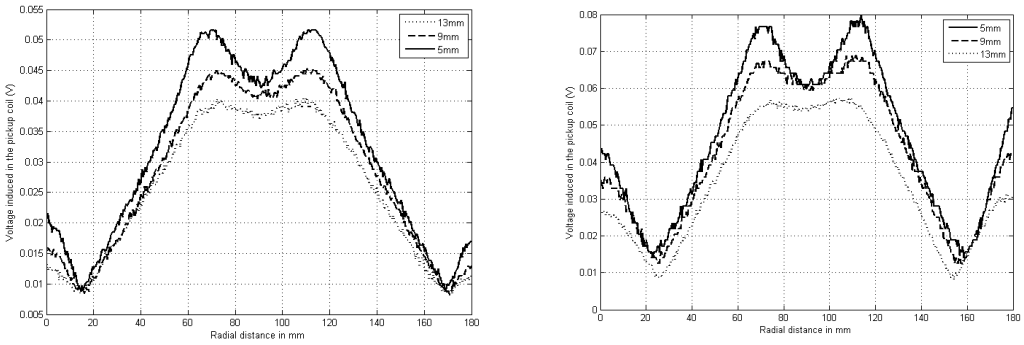

(a) (b)

Figure 3.9: Measurement results of B_z at different distances from Coil 1 loaded with the ferromagnetic steel (a) without ferrite and (b) with ferrite.

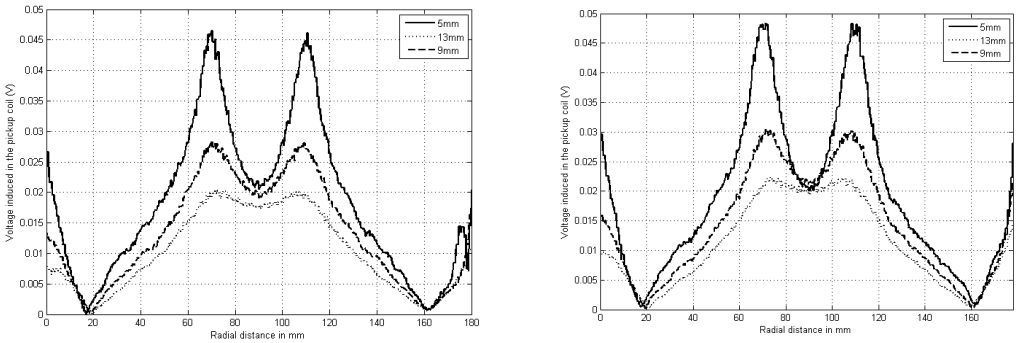

(a) (b)

Figure 3.10: Simulation results of B_z at different distances from Coil 1 loaded with the ferromagnetic steel (a) without ferrite and (b) with ferrite.

even though the coil with the ferrite drew 12% less current from the supply. If the gain in B_z due to the ferrite is normalized with current, it will become 39.2%. This improvement was 29% for the unloaded case. So it is clear that using a ferromagnetic load improves the effect of ferrite on the system. As we expected, the magnitude of B_z in the loaded case is less than B_z shown in Figure 3.6. This is due to the opposing B_z in the $-z$-direction created by the eddy currents in the load. The inductance of the system with the ferrite and the ferromagnetic steel dropped to 24.54 from 80 μH. This drop is reflected to the decrease in B_z as expected.

The simulation results for the same case is shown in Figure 3.10. Simulation

results are consistent with the measurements except for the fact that the valleys in the simulation results are deeper than the valleys in the measurement results. This is due to the averaging of B_z in the measurement since the pickup coil has finite area. This discrepancy between the measurement and simulation results can be alleviated by reducing the radius of the pickup coil. However, this would require to feed the coil with higher power since the induced voltage in the pickup coil would be smaller and more noisy as the radius of the pickup coil gets smaller.

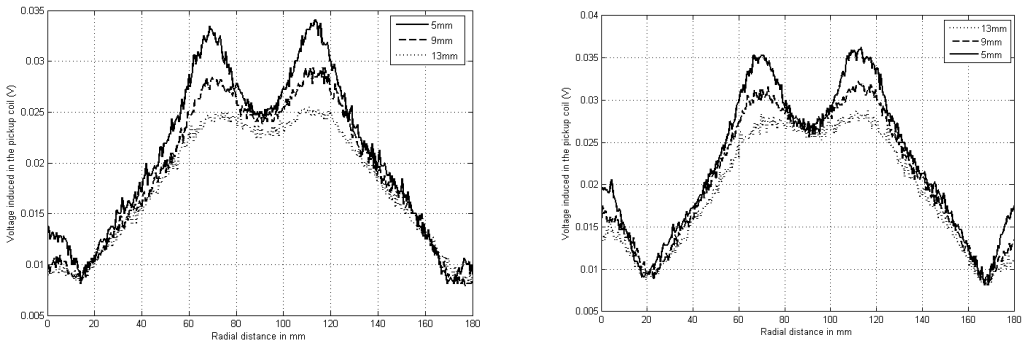

(a) (b)

Figure 3.11: Measurement results of B_z at different distances from Coil 1 loaded with aluminum (a) without ferrite and (b) with ferrite.

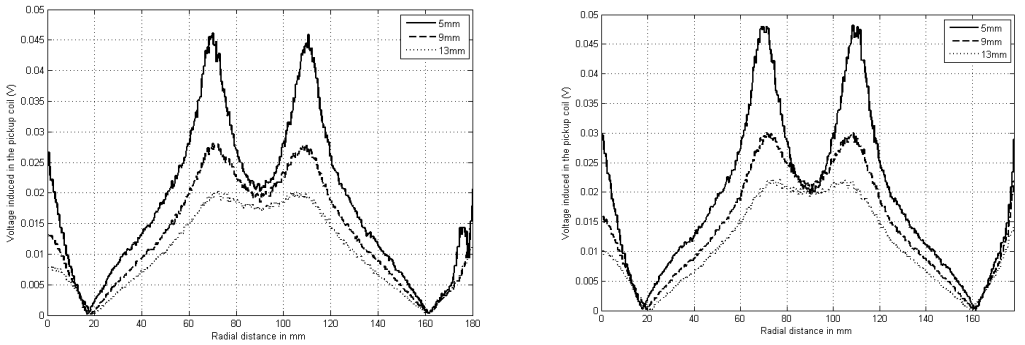

(a) (b)

Figure 3.12: Simulation results of B_z at different distances from Coil 1 loaded with aluminum (a) without ferrite and (b) with ferrite.

In Figures 3.11 and 3.12 the measurement and simulation of the magnitude

of B_z are shown, respectively, when the coil is loaded with the aluminum. As seen in these figures, when the coil is loaded with the aluminum, the magnitude of B_z drastically decreases compared to the ferromagnetic steel case. This means that the electrical loss in the aluminum is less than the electrical loss in the ferromagnetic steel case. Actually, the impedance of the system with the ferrite at 100 kHz when it is loaded with aluminum is $0.578 + j4.76\ \Omega$, whereas it is $9.93 + j15.41\ \Omega$ when loaded with the ferromagnetic steel. The inductance of the system is dropped to 7.58 from 24.54 μH. This smaller value of inductance of the system loaded with the aluminum describes why B_z is weaker when the coil is loaded with the aluminum than when it is loaded with the ferromagnetic steel. Since we drive the system with a constant voltage supply, when the coil is loaded with the aluminum, it draws more current from the supply compared to when the coil is loaded with the ferromagnetic steel. The aluminum load heats up less even though the coil with the aluminum load draws almost 4 times as much current as the coil with the ferromagnetic steel load. This is also apparent in the resistance part of the impedance. This can also be easily seen by comparing the resistive parts of the impedances. When the coil is loaded with the aluminum, the resistance of the system is only 0.578 Ω and in the ferromagnetic steel case it is 9.93 Ω. This shows that heating materials with ferromagnetic properties is more efficient than heating materials without magnetic properties (aluminum, copper, etc.) and apparently this coil will never be able to heat the aluminum.

3.1.3 Case study: Coil 2 (rectangular cross-section coil)

The coil we analyzed in this part (Coil 2) is one of the coils (which Bosch uses in its induction ovens). This coil has 26 turns and its outer diameter is 145 mm. In this part we performed the same measurements that we performed for Coil 1 in the previous part. These are unloaded with the ferrite and then without the ferrite, and are also loaded with the ferromagnetic steel and aluminum with and without ferrite. We performed the measurements by driving Coil 2 in the same way as we did Coil 1 in the previous part.

3.1.3.1 Unloaded Measurements and Simulations of Coil 2

In Figure 3.13, B_z created by Coil 2 is shown. The difference between this coil and Coil 1 is that the turns in this coil has a rectangular cross section whereas turns in Coil 1 has a circular cross section. Thus, in this coil, more turns could be stacked into a smaller coil diameter. Coil 1 is 180 mm in diameter, although it has fewer turns (24) than Coil 2. This difference in diameters substantially decreases the inductance of Coil 2. Unloaded Coil 2 without the ferrite has an inductance of 50 μH whereas it was 59 μH for Coil 1. So Coil 2 draws much more current than Coil 1 since we feed both coils with a constant voltage source. This difference can be seen when Figure 3.13 is compared with Figure 3.6. Coil 2 creates more B_z than Coil 1 even though the number of turns in both coils is very close. If it is desired to have a low inductance coil without sacrificing number of turns, the wire crosssection should be chosen rectangular instead of circular so that more turns can be squeezed in less space.

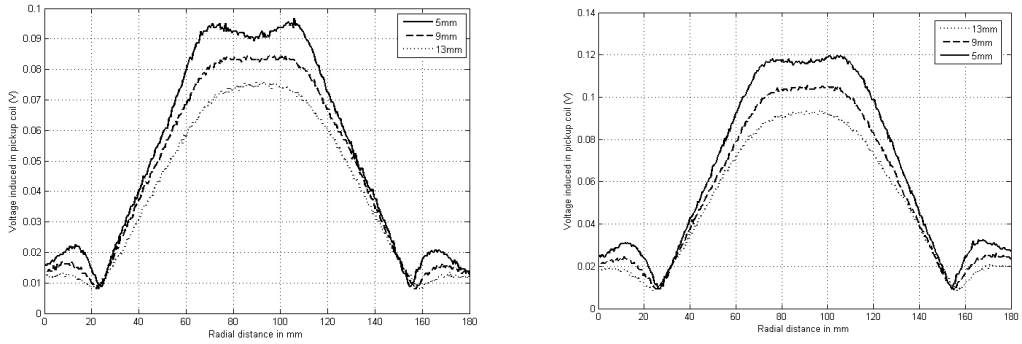

(a) (b)

Figure 3.13: Measurement results of B_z at different distances from unloaded Coil 2 (a) without ferrite and (b) with ferrite.

Figure 3.14 shows the simulation results of unloaded Coil 2. The results are consistent with the measurements. Figure 3.15 shows the all-surface scan of Coil 2. The magnetic field in the z-direction here is symmetric in the ϕ-direction as expected.

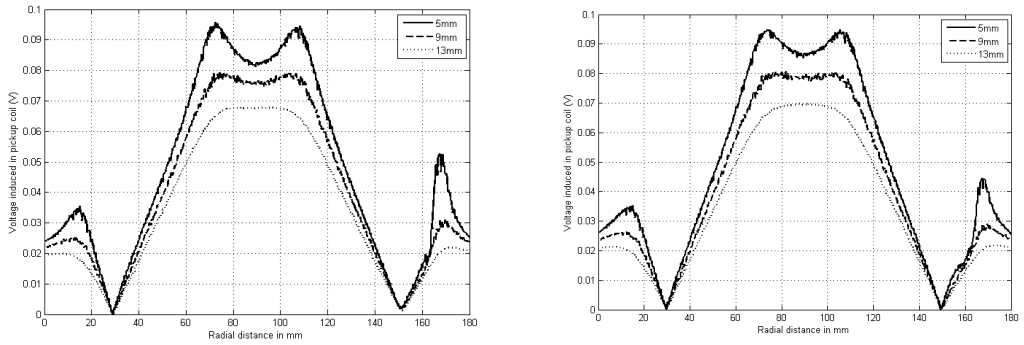

(a) (b)

Figure 3.14: Simulation results of B_z at different distances from unloaded Coil 2 (a) without ferrite and (b) with ferrite.

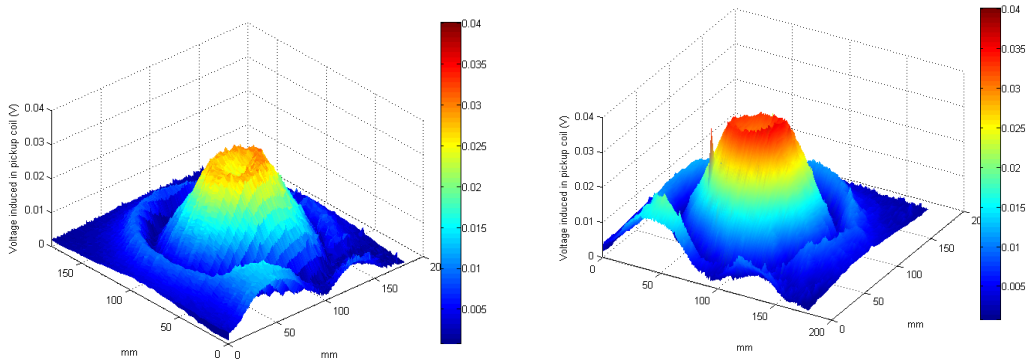

(a) (b)

Figure 3.15: All surface scan of B_z at 5 mm above unloaded Coil 2 (a) without ferrite and (b) with ferrite.

3.1.3.2 Loaded Measurements of Coil 2

For the loaded analysis, we loaded Coil 2 with the same ferromagnetic steel and aluminum as we loaded Coil 1 with. Figure 3.16 shows the magnitude of B_z when Coil 2 is loaded with ferromagnetic steel. The value of B_z is much higher than B_z when using Coil 1. For Coil 2 without ferrite, the peak value of the induced voltage in the pickup coil is around 65 mV whereas it is 50 mV for Coil 1. This shows that when we drive both coils with the same voltage source, Coil 2 will be able to heat the load better than Coil 1. The same argument holds true for the aluminum load case. As seen in Figure 3.17, the peak value of the induced

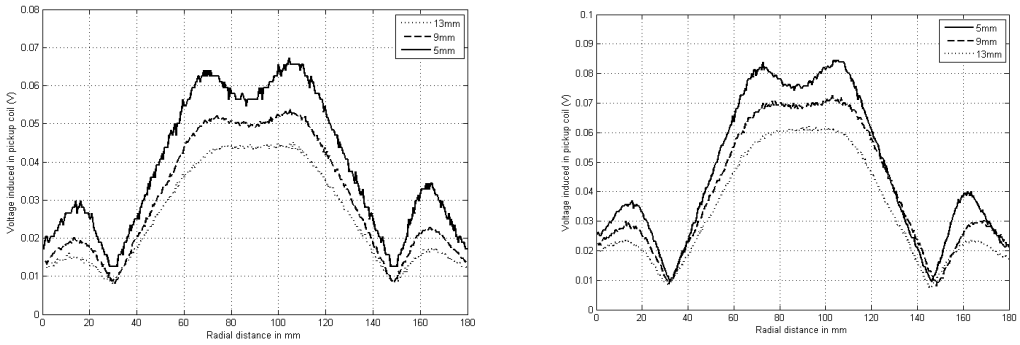

(a) (b)

Figure 3.16: Measurement results of B_z at different distances from Coil 2 loaded with ferromagnetic steel (a) without ferrite and (b) with ferrite.

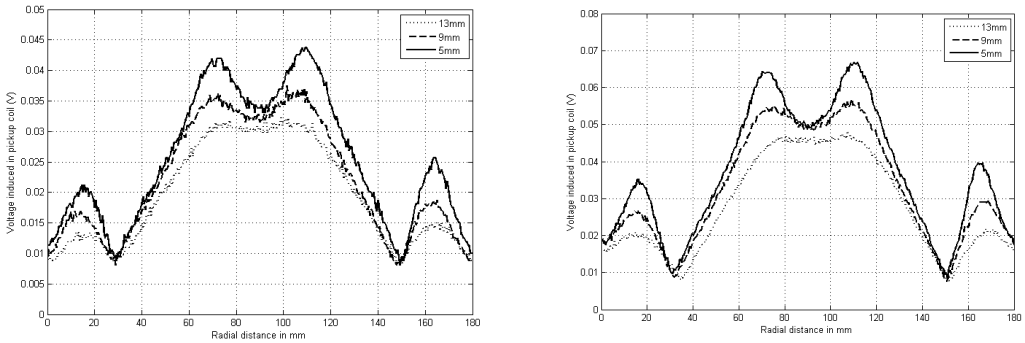

(a) (b)

Figure 3.17: Measurement results of B_z at different distances from Coil 2 loaded with aluminum (a) without ferrite and (b) with ferrite.

voltage in the pickup coil is around 45 mV whereas this value for the Coil 1 is around 35 mV.

3.1.4 Case study: Coil 3 (multi-layer, high-turn coil)

The coil we have analyzed in this part is employed for all metal heating purposes in induction ovens (used by Hitachi). By all-metal, we mean coils that are able to heat non-magnetic materials like aluminum and copper. As we have seen in previous analysis, it is hard to heat these metals since they do not enhance the

magnetic field in the z-direction like ferromagnetic steel does. To heat metals like copper and aluminum, B_z and/or frequency of operation must be increased so that the time-varying magnetic flux linked to the load is increased. One way of increasing the magnitude of B_z coupled to the load is to use large number of turns and/or large current values. A smart way of utilizing ferrite also increases B_z.

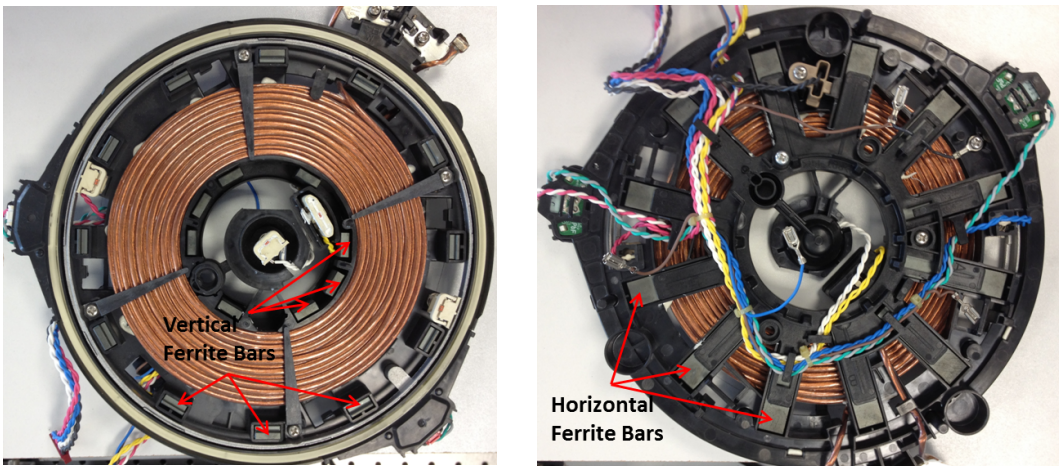

(a) (b)

Figure 3.18: Pictures of Coil 3 (a) front view and (b) back view.

For this purpose, the coil shown in Figure 3.18 can be used. This coil has an inner radius of 45 mm and an outer radius of 80 mm. Note that this coil is smaller in diameter than Coil 1 we analyzed in the previous part but still has about 40 turns squeezed in three layers. Usual operating frequency of such coils is around 100 kHz. Although this coil is able to heat metals like copper and aluminum the efficiency of this heating is around 30% to 40% whereas the efficiencies for heating a ferromagnetic steel is above 90%.

Figure 3.19 shows the magnitude of B_z when the coil is driven with constant voltage source at 100 kHz. The coil is unloaded and measurement is taken at a distance of 8 mm above the coil. The impedance of the coil is measured to be $0.77 + j196\ \Omega$. Due to high number of turns, inductance of the unloaded Coil 3 is quite large compared to other coils we analyzed before. It has an inductance of 312 μH whereas it is 59 μH for Coil 1. To heat non-ferromagnetic materials,

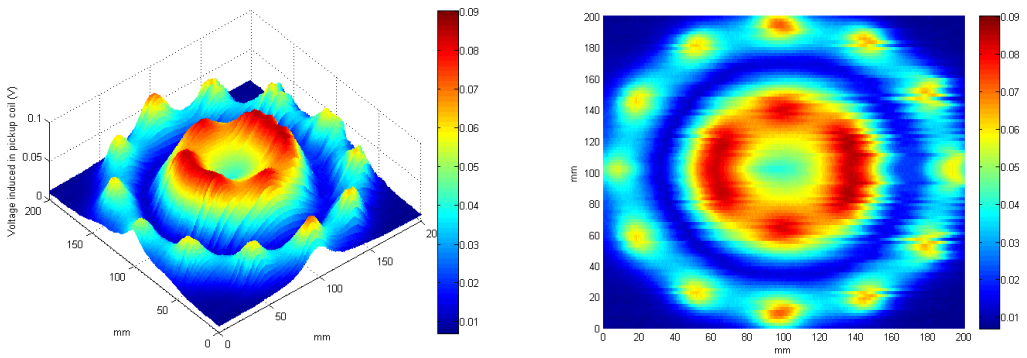

(a) (b)

Figure 3.19: All-surface scan of B_z at 8 mm above unloaded Coil 3 (a) profile view and (b) top view.

such high inductances are necessary. Since the inner radius of this coil is quite large compared to Coil 2 and Coil 1, the valley in the middle of the coil is deeper and more visible here.

The ferrite placement is seen in Figure 3.18. Ferrite bars around the inner and outer edges of the coil are placed perpendicular to the plane of the coil. Ferrite bars placed under the coil are parallel to the plane of the coil. Ferrite placement is such that B_z is trapped in the coil geometry. The magnetic field right where the first turn starts is not symmetric in the ϕ-direction. This is due to the asymmetric ferrite placement (Figure 3.18a) in the inner part of the coil. All the peaks around the outer edge of the coil are due to the perpendicular ferrite placements. This type of ferrite placement has indeed some advantages. First of all, ferrite bars placed perpendicular around the outer edge of the coil attracts B_z otherwise leaking from the edges of the coil and redirects it toward the load. Thus, this avoids magnetic field leakage.

Secondly, this perpendicular ferrite placement helps to heat up the load more homogeneously. Wherever B_z makes a peak at the boundary of the load, there occurs the largest flux change in that region. The strongest eddy currents can be observed to start flowing around that peak to oppose that magnetic field. This, we can see that the regions of the load that first heat up are the regions of circles around where these magnetic field peaks occur. Such a ferrite placement enables

the load to start heating up at multiple locations simultaneously. This results in a more homogeneous heating of the load than both Coil 1 and Coil 2 would offer. Because in the latter ones magnetic field only peaks around the middle of the coil.

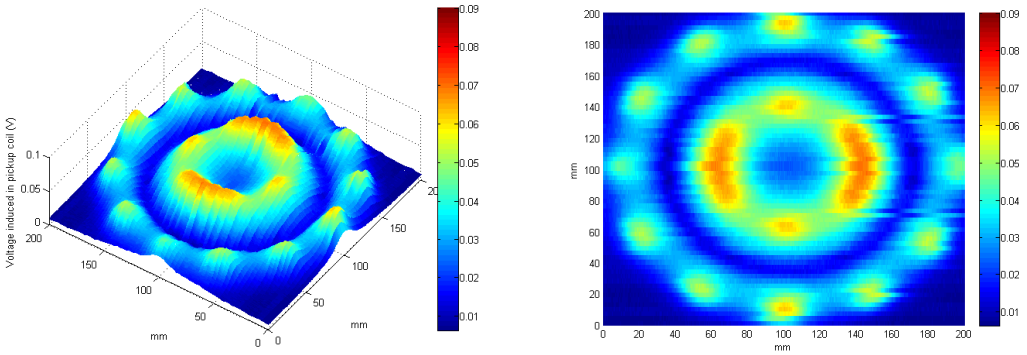

(a) (b)

Figure 3.20: All surface scan of B_z at 8 mm above Coil 3 loaded with ferromagnetic steel (a) profile view and (b) top view.

Figures 3.20 and 3.21 show B_z at the surface of a plane 8 mm above the coil when the coil is loaded with the ferromagnetic steel and the aluminum, respectively. The loads are placed about 15 mm above the coil. The results are as expected and consistent with the findings of previously analyzed coils. The ferromagnetic steel enhances B_z between the coil and the load so we observe a stronger B_z in the ferromagnetic steel case than the aluminum case. The impedance of the system when loaded with the ferromagnetic steel is measured to be $25 + j125$ Ω and it is $1.17 + j96$ Ω when loaded with the aluminum. When Coil 3 is loaded with the aluminum, the system (coil+load) has a resistance of 1.17 Ω, which is much higher than the resistance of the Coil 1 which is 0.578 Ω when loaded with the aluminum. This difference indicates that Coil 3 is more capable of heating aluminum than Coil 1. One crucial point here is that when a coil is designed to heat non-ferromagnetic metals like aluminum, they can not be used to heat ferromagnetic metals. To heat aluminum, coil needs significantly more turns and need to be operated at resonance at higher frequencies. Higher turns mean much more inductance than a typical coil used to heat a ferromagnetic material. When

a ferromagnetic metal is placed above a coil of which inductance is already very high when loaded with aluminum, the inductance becomes even higher. In practice induction ovens use a constant capacitor value and the resonance frequency is predetermined and hard-coded in programmable interrupt controller (PIC). Thus, when a ferromagnetic load is placed on a coil system that is intended to heat an aluminum load, due to high inductance change, either the frequency or the tuning capacitance value should be changed during the run time for the system to still operate. Since both of these values are preset, the system will walk off the resonance and not be able to deliver power to the load efficiently.

To sum up, induction ovens with fixed operating frequency are usually designed to work with either ferromagnetic or non ferromagnetic loads. However, systems that have hardware to change the frequency of operation or tuning capacitance used to keep the system in resonance during the runtime are capable of working with either type of the load.

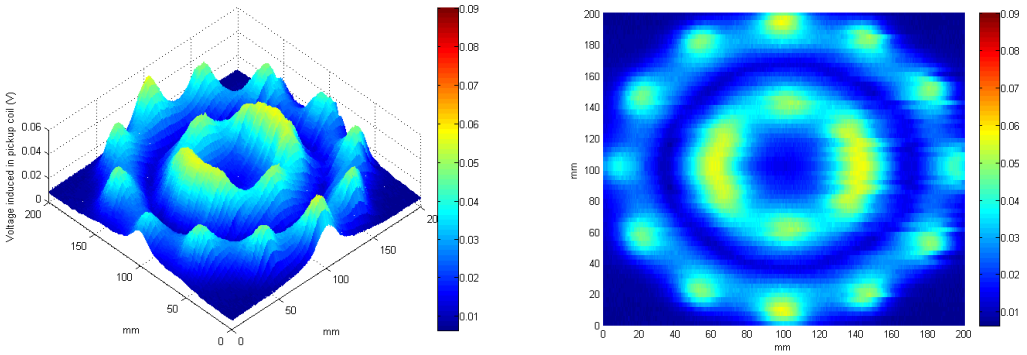

(a) (b)

Figure 3.21: All surface scan of B_z at 8 mm above Coil 3 loaded with aluminum: (a) profile view and (b) top view.

3.1.5 Case study: Coil 4 (pancake coil)

Another type of coil that is used in induction ovens is what is called pancake type. This kind is indeed a combination of two coils. As seen in Figure 3.22, a coil with a smaller outer diameter is enclosed within another coil of a larger

diameter. For example, here the inner radius of the inner coil is 25 mm while the outer coil has inner radius of 60 mm. In this structure two coils are connected in series forming a single coil. In various applications [33], by using these two coils separately adaptable diameter burners for induction ovens are made. In other words, either the inner or the outer coil is powered up depending on the size of the load put on it. As shown in Figure 3.22a ferrite bars are horizontally placed below the coil which is usually the common intuition in ferrite placement. In our

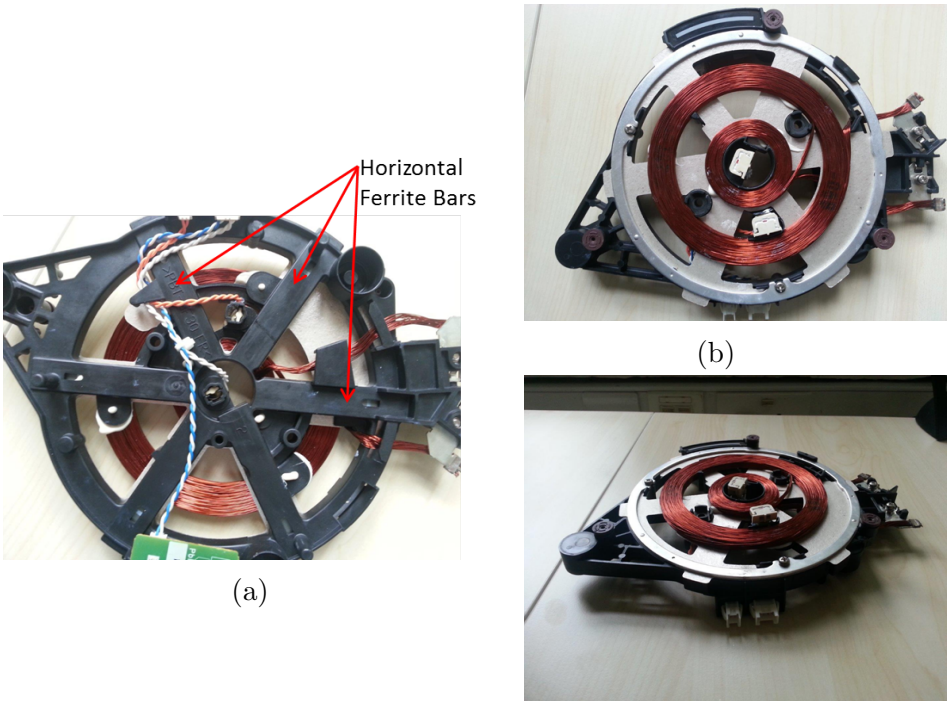

(a)

(b)

(c)

Figure 3.22: Analyzed Coil 4:(a) rear view, (b) front view and (c) side view.

analysis of this coil, Coil 4 was driven 100 kHz with a constant voltage supply. We took measurements of B_z when the coil was unloaded and then loaded with the ferromagnetic steel and aluminum.

Figure 3.23 shows magnitude of B_z for the unloaded case. The measurement was taken 8 mm above the coil. One advantage of using this type of coil is immediately apparent in this figure. The main advantage of using this type of coil is that the magnetic field in the z-direction for this coil is quite homogeneous in the center of the coil. In other words, there is no a deep valley in the middle of

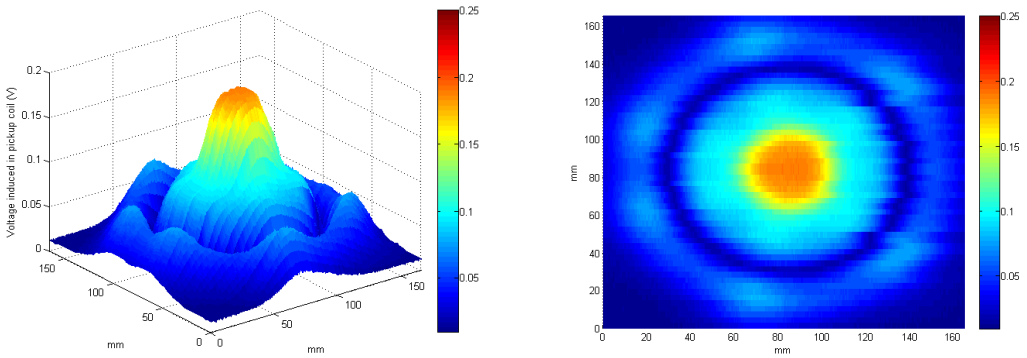

(a) (b)

Figure 3.23: All surface scan of B_z at 8 mm above unloaded Coil 4(a) profile view and (b) top view.

the coil as it was the case for the rest of the coils we analyzed in previous parts. This coil type heats up the load more homogeneously than other coils. The small peaks around the outer diameter are due to the ferrite bars seen in Figure 3.22a. As we mentioned before this type of ferrite placement avoids leakage of magnetic field.

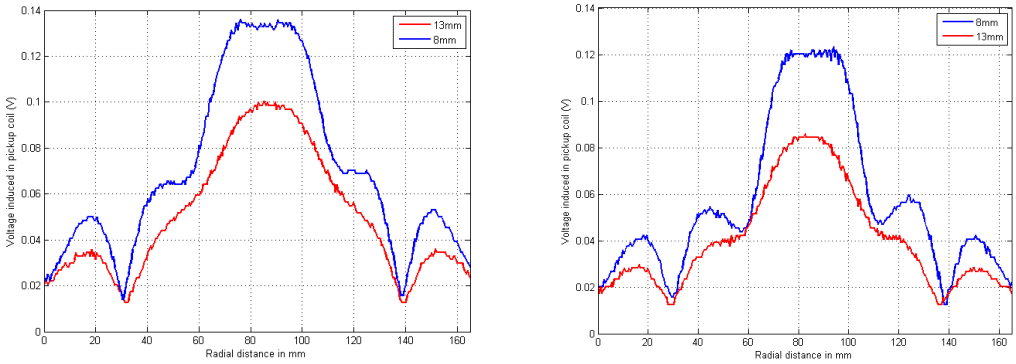

(a) (b)

Figure 3.24: Measurement results of B_z at different distances from Coil 4 loaded with(a) ferromagnetic steel and (b)aluminum.

Figure 3.24 shows measurement of B_z when the coil is loaded with the ferromagnetic steel and aluminum. The measurements were taken between the coil and the load at a distance of 8 and 13 mm above the coil. The magnetic field in

the case of the ferromagnetic steel loading is larger than the aluminum case as we expect. One point to notice here is that, in other coil structures when loaded, B_z in the center of the coil makes a larger dip than it makes in the unloaded case. However, we do not observe this effect here. Around the center of the coil, the resulting magnetic field is still uniform despite the load. This is an important advantage of this type of coils. The distance between the inner coil and outer coil makes B_z uniform around the center. One disadvantage is the gap between the two coils forming the structure. In some cases where larger turns are required, it may not be possible to leave a gap between the inner and outer parts. This is simply a compromise between heating more uniformly and delivering more power to the load.

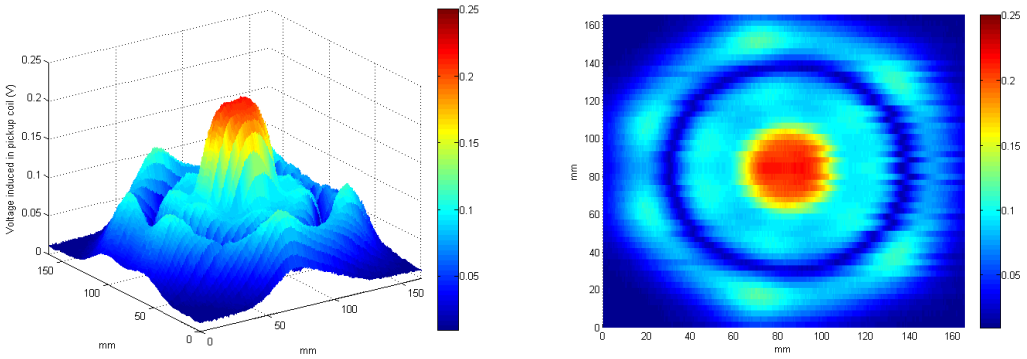

(a) (b)

Figure 3.25: All surface scan of B_z at 8 mm above Coil 4 loaded with ferromagnetic steel (a) profile view and (b) top view.

Finally, Figure 3.25 shows B_z on a plane parallel to the coil plane at 8 mm above it. The magnetic field is symmetric in the ϕ-direction as we expected.

Here note that all the coils we have analyzed so far are circular in shape. Indeed the shape does not have to be circular. In Chapter 5 we will talk about coils in geometric shapes other than the circle and summarize a unique design of ourselves for all surface induction ovens.

3.2 Effects of Inner and Outer Radii of Coils on Magnetic Field and Efficiency of the System

In this part we analyzed the effects of the inner and outer radii of coils on the magnetic field in the z-direction and efficiency of the coil. For this purpose we prepared a prototype structure as shown in Figure Figure 3.26 which enabled us to make coils with different inner and outer radius values. For the experimental characterization we used the setup given in Figure 3.1 and employed measurement technique II illustrated in Figure 3.3. For the numerical study we used CST EM studio.

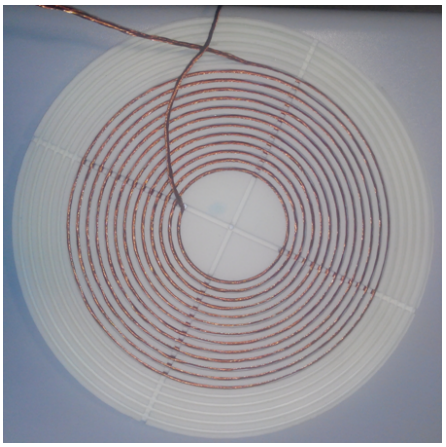

Figure 3.26: Prototype structure.

To study the effect of the inner and outer radius of the coil on magnetic field and efficiency, we made two sets of measurements. In the first set, we changed the inner radius of the standard circular coil we designed keeping the number of turns constant and in the second set we changed the inner radius of the coil keeping the length of the wire constant and observed how the magnetic field strength changes in response.

3.2.1 Constant Number of Turns

In this part using the prototype structure we designed, we created a 15-turn coil in three different inner radii values. These are 19.0, 30.5 and 39.7 mm. The magnetic field in the z-direction is measured for all these three cases with surface scans and these results are supported with the numerical results obtained using CST EM Studio.

For the measurements and simulations we drived the coil at 50 kHz with a sine wave of 100 V_{rms}. All of the coils are loaded with the ferromagnetic steel placed about 10 mm above the coil plane and the measurements were taken at 5 mm above the coil. The measurements and simulations were done without ferrite.

The surface scan of B_z is seen in Figures 3.27, 3.28 and 3.29 for the inner radius 19.0, 30.5 and 39.7 mm respectively. In each of the presented measurement scans there are two circles drawn in dashed black line. The inner circle indicates the inner radius of the coil and the outer circle, the outer radius. As the radius increases, B_z spreads out while the peak gets smaller, as seen in Figure 3.30. This is due to the increase in the inductance of the coil as the radius increases. Since we feed the coil with a voltage source as the inductance increases (as the radius increases keeping the number of turns fixed), the amount of current the coil draws from the supply decreases. However, increase in the inductance is much more than the decrease in the current drawn from the coil as a result of which the magnetic flux coupled to the load is increased, in turn increasing the ohmic loss heating in the load as seen in Figure 3.31.

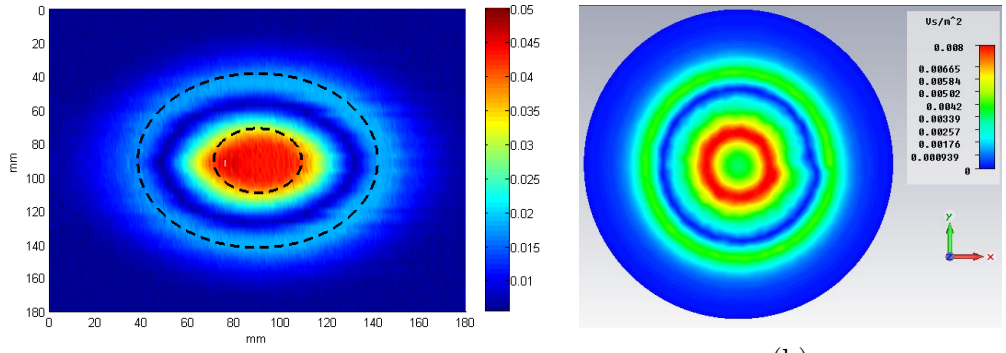

(a) (b)

Figure 3.27: All surface scan of B_z at 5 mm above the prototype coil with an inner radius of 19.0 mm and loaded with the ferromagnetic steel: (a) measurement and (b) simulation.

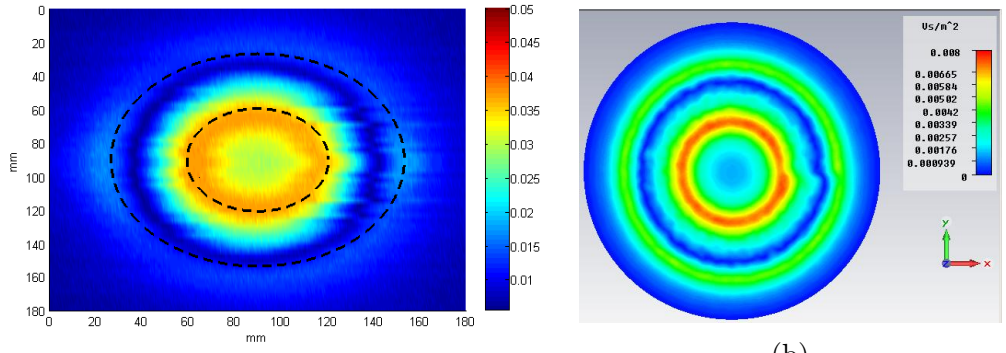

(a) (b)

Figure 3.28: All surface scan of B_z at 5 mm above the prototype coil with an inner radius of 30.5 mm and loaded with the ferromagnetic steel: (a) measurement and (b) simulation.

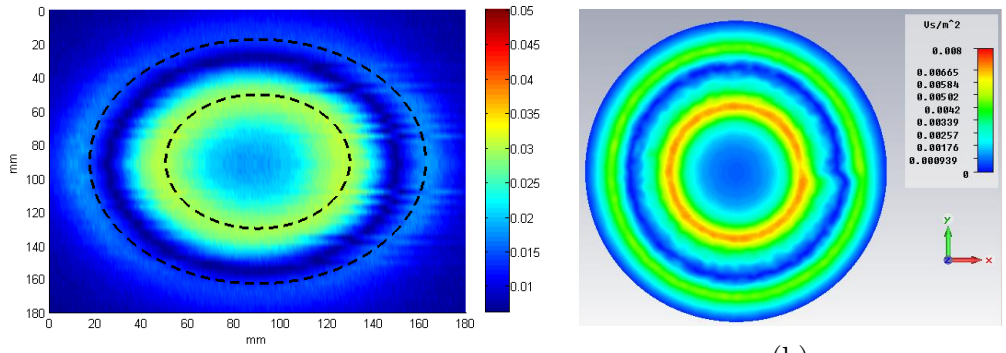

(a) (b)

Figure 3.29: All surface scan of B_z at 5 mm above the prototype coil with an inner radius of 39.7 mm and loaded with the ferromagnetic steel: (a) measurement and (b) simulation.

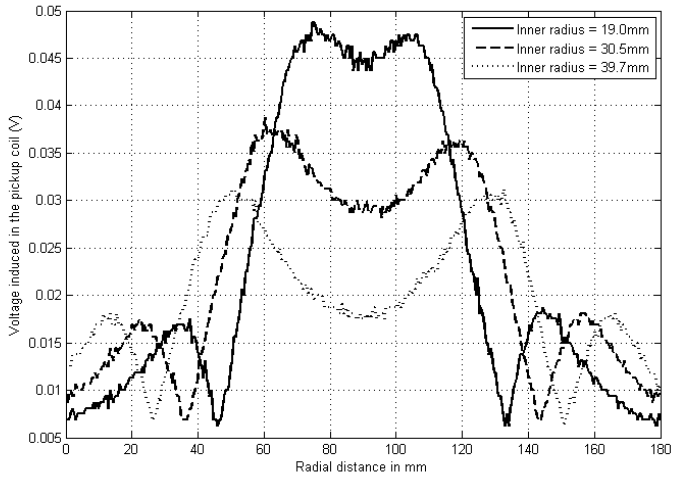

Figure 3.30: Measurement of B_z at 5 mm above the prototype coil with different inner radius values loaded with the ferromagnetic steel.

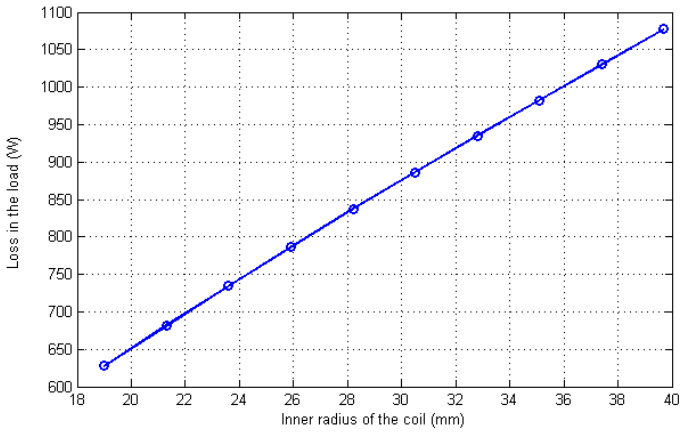

Figure 3.31: Change in the electrical loss in the load.

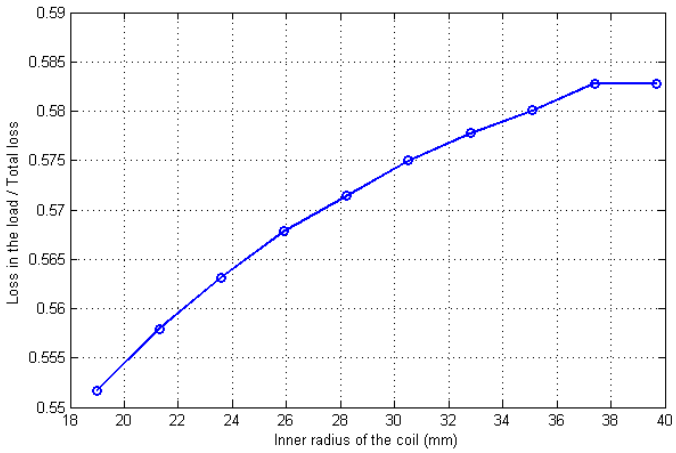

Figure 3.32: Change in efficiency as a function of the inner radius.

However, here since we kept the number of turns constant, the length of the wire also increases with the increasing radius. In other words, the loss in the wire also increases with the loss in the load. As seen in Figure 3.32, the efficiency increases up to a point and then saturates. This is where the diameter of the coil is equal to the diameter of the load. Further increase in the radius of the coil decreases the efficiency because part of the coil would not be covered by the load and magnetic field would leak into the air. This shows that, given a certain number of turns, one should design a coil as large as the diameter of the load desired to be heated. As long as the number of turns is constant, the larger the inner radius as the load permits the better the efficiency is. We normally expect an efficiency of above 90% when the load used is ferromagnetic steel; however, as seen in Figure 3.32, the efficiency of the coil can only go up to around 58%. This is mainly due to how we model the wires in CST. Due to computational limitations we define the wire as a solid copper wire of diameter in the order of mm. Due to skin effect, ac resistance of the wire becomes too large since at high frequencies current flows close to the surface of the wire. To decrease this resistance, Litz-wire is used instead of a single solid wire. This substantially drops the resistance of the coil. In [34, 35] frequency dependence of the ac resistance of the wires is explained in detail and depending on the current with which the coil is driven using an optimum number of Litz strands is calculated.

3.2.2 Constant Wire Length

In this part we kept the length of the wire constant at 5400 mm and analyzed B_z and efficiency of the system using four different inner radius values. These are 31, 41, 51 and 61 mm. This time in simulations coils are driven with a constant current source at 50 kHz. Coils are loaded with the ferromagnetic steel. Since we drive the coils with a constant current source this time, the comparison of B_z in Figures 3.33 and 3.34 directly gives us the comparison between inductances of the system.

As the inner radius is increased while keeping wire length constant, the number of turns that can be wound decreases. This decreases the inductance and

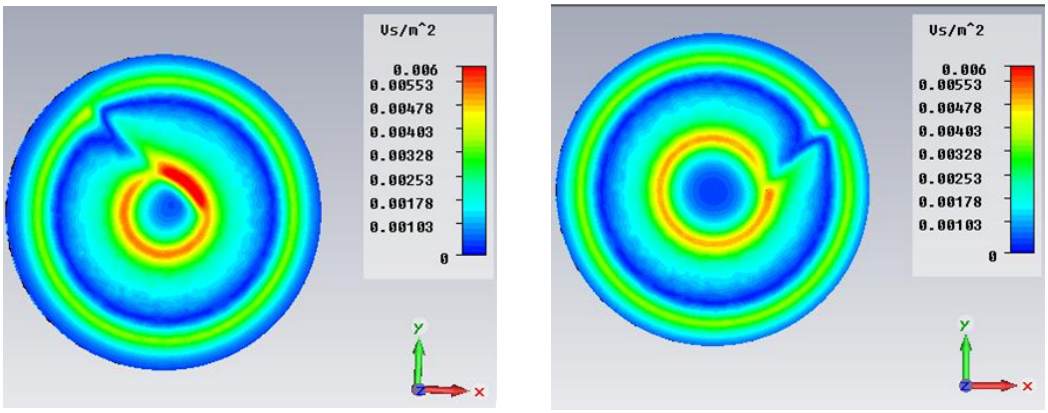

(a) (b)

Figure 3.33: All surface scan of B_z at 5 mm above the prototype coil loaded with the ferromagnetic steel when (a)the radius is 31 mm and (b) the radius is 41 mm.

the magnetic flux linked to the load since the inductance is proportional to the square of the number of turns. This decrease in magnetic flux then decreases the electrical loss in the load because the loss in the load is solely due to the magnetic flux change the load is exposed to. Since the wire length is constant, the loss in the wire can be assumed to be constant as the inner radius increases; however, the loss in the load decreases at the same time. As a result, as the inner radius increases, the efficiency decreases. These two points are illustrated in Figures 3.35 and 3.36.

When the length of the wire to be used for a coil is constant, it is better to keep the inner radius as small as possible. This way the highest efficiency can be attained. When we combine the results of previous section with the results of this section, we can conclude that if there is no restriction on either the number of turns or the wire length, the best design strategy is to keep the inner radius the smallest and outer radius as large as the radius of the load so that the coil would totally be covered by the load.

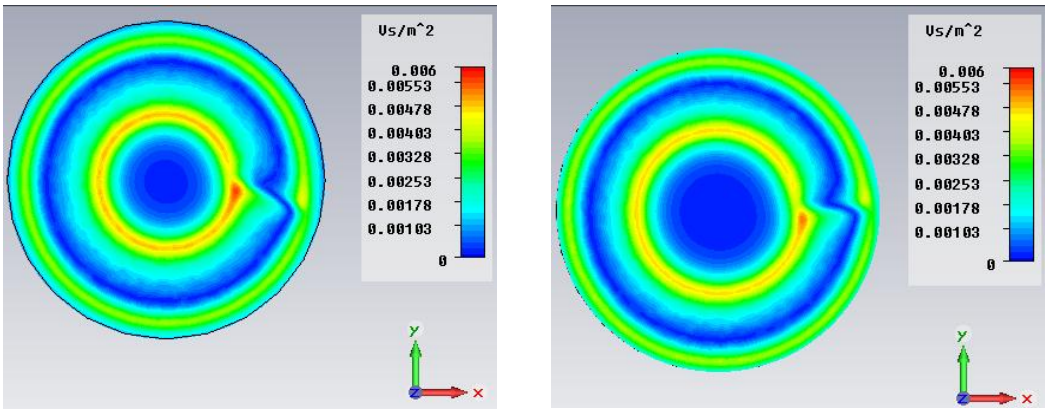

(a) (b)

Figure 3.34: All surface scan of B_z at 5 mm above the prototype coil loaded with the ferromagnetic steel when (a)the radius is 51 mm and (b) the radius is 61 mm.

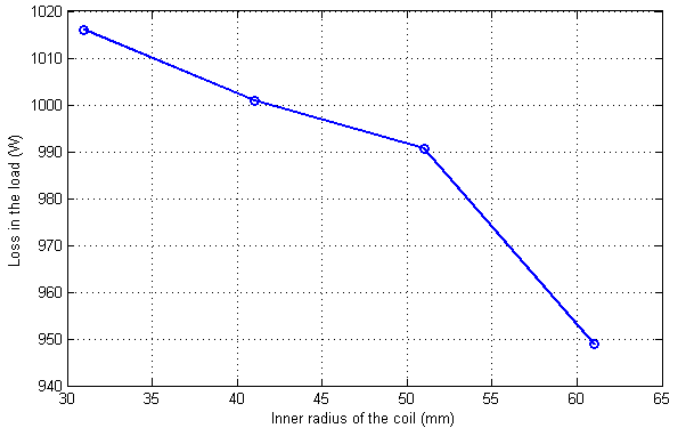

Figure 3.35: Change in the electrical loss in the load.

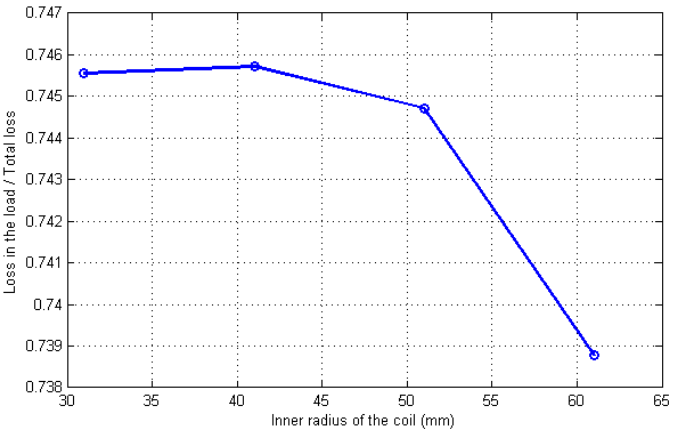

Figure 3.36: Change in efficiency as a function of the inner radius.

Chapter 4

Utilization of Ferrite for Inductive Heating

A typical assembly of the inductive heating system is shown in Figure 2.1. Underneath the coil is totally covered by ferrite. There are two advantages of using ferrite in such a system. The first one is that the electronics below the coil is shielded from the fields generated by the coil. The second one is that ferrite enhances the magnetic field in the z-direction created by the coil. This enhancement increases the electrical loss in the load. Therefore, by utilizing ferrite in induction ovens, higher electrical loss in the load can be achieved with smaller currents injected into the coil. At the frequency range of interest (20 to 100 kHz), the ferrite plane can be considered as a lossless medium. This way efficiency of the system is increased substantially by utilization of ferrite.

There are two important features of ferrite to be considered to determine what ferrite parameters to use. These are thickness and relative permeability. To understand the relation between the thickness and permeability of ferrite bars we reproduced the results of [36] using CST EMS. The coil we used in our analysis is a 23-turn coil of 25 mm in inner radius and 105 mm in outer radius . The load we used has $\sigma = 8 \times 10^6\ \Omega^{-1}m^{-1}$ and $\mu_r = 500$. The load is placed 5 mm above the coil and coil is fed at 50 kHz.

In [37] by using the method of current images it is shown that, for an unloaded planar spiral inductor, ferrite of infinite thickness increases the inductance of the coil by 100% for $\mu_r \gg 1$. Here with the finite thickness ferrite and loaded coils as shown in Figure 4.1, a total gain of about 60% is achievable with the utilization of ferrite in the frequency range of interest (20-100 kHz). These figures show that the maximum gain is achievable with high μ_r and thin ferrite or with low μ_r and thick ferrite. In other words, if the μ_r of the ferrite to be used is above 1000, there is no need to use a ferrite thicker than a couple of mm's.

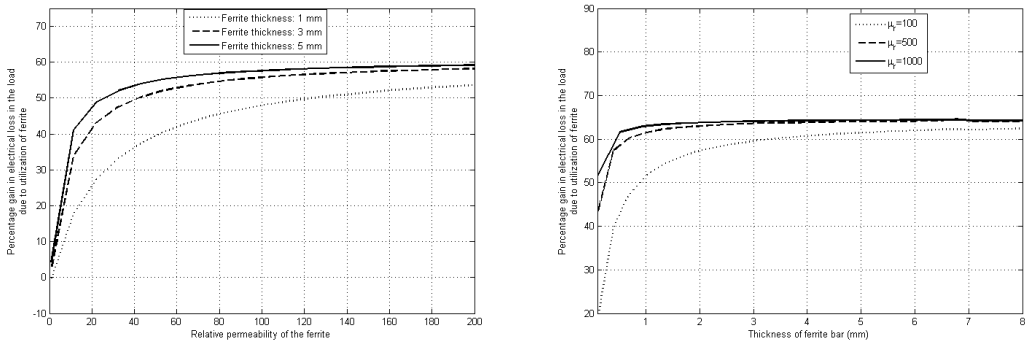

(a) (b)

Figure 4.1: Gain in the electrical loss (a) for different ferrite μ_r and (b)for different ferrite thicknesses.

To understand the effects of ferrite on the fields in the system we used CST EM studio for numerical analysis. In this analysis we simulated the 24-turn standard coil used by Arçelik (Coil 1). The coil is loaded with a 1 mm thick ferromagnetic steel of $\sigma = 1.6 \times 10^6\ \Omega^{-1}m^{-1}$, $\mu_r = 200$ and is placed 10 mm above the coil. The coil is driven at 35 kHz with a constant current source of amplitude 40 A. A ferrite film with thickness of 5 mm and $\mu_r = 500$ is placed 3 mm below the coil. The coil is modeled as a round copper wire of diameter 1.3 mm. The fields are analyzed in three regions. The first region is between the coil and the load and 2 mm above the coil, the second region is between the coil and the ferrite and 2 mm below the coil. The third region is below the ferrite and 11 mm below the coil. The r-and z-components of magnetic fields are investigated in these three regions.

Figure 4.2 shows B_r and B_z at 2 mm above the coil between the coil and the load. As expected, ferrite placed under the coil enhances each component of the magnetic field between the coil and the load. However, the situation is quite different in Region 2, in this example at 2 mm below the coil between the coil and the ferrite. As shown in Figure 4.3, ferrite weakens the magnetic field in the r-direction whereas it enhances the magnetic field in the z-direction below the coil. This is also an expected result. In planar coils used in induction ovens, r component of magnetic field above the coil is in the +r-direction whereas the same component below the coil is in the -r-direction. In an ideal ferrite, no H_r can exist. Due to the continuity of H_r, H_r is zero right at the border of ferrite and air. To satisfy the boundary condition ferrite reflects the r component magnetic field with a 180° degrees phase difference and this results in a reduced B_r between the coil and the ferrite due to the destructive interference. B_z is still enhanced in this region since B_z is continuous throughout the system. Finally, Figure 4.4 shows the fields below the ferrite about 11 mm away from the coil. In Region 3, both components of the magnetic field is blocked by the ferrite. In other words, very little amount of the magnetic field can pass through the ferrite to the other side. If it were a perfect magnetic conductor with $\mu_r = \infty$, there would be absolutely no field on the other side of the ferrite. However, in our case we have a ferrite with $\mu_r = 200$, and that is why some part of the fields can make it to the other side of the ferrite. As seen in Figure 4.4, fields were substantially reduced by a factor of more than 16 and indeed this is enough shielding for the electronics below the coil.

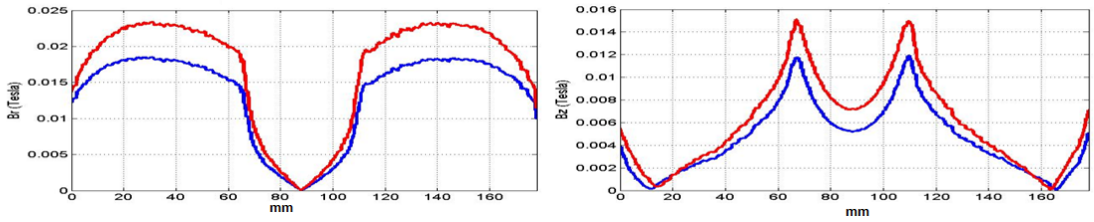

(a) (b)

Figure 4.2: Simulation results of magnetic field components in Region 1 with ferrite (red plot) and without ferrite (blue plot): (a) B_r and (b)B_z.

Covering the coil underneath totally with the ferrite and keeping this ferrite

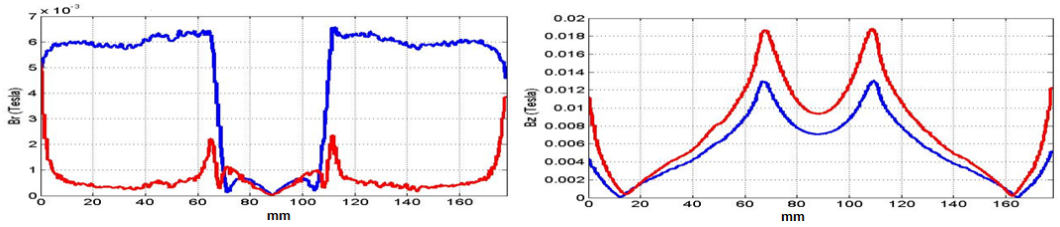

(a) (b)

Figure 4.3: Simulation results of magnetic field components in Region 2 with ferrite (red plot) and without ferrite (blue plot): (a) B_r and (b)B_z.

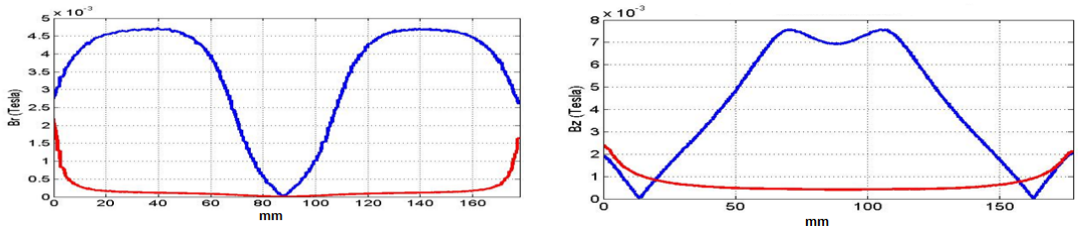

(a) (b)

Figure 4.4: Simulation results of magnetic field components in Region 3 with ferrite (red plot) and without ferrite (blue plot): (a) B_r and (b)B_z.

as close to the coil as possible may seem to be the optimum way of utilizing the ferrite. However, covering under the coil with ferrite adds to the cost of the system significantly. Thus, optimum ferrite placement and deciding on the amount of the ferrite to be used are crucial. In the following sections, we analyzed different ferrite placements both numerically and experimentally and worked on an optimum ferrite placement.

4.1 Change in the field enhancement with different ferrite coverages

It is not easy to have ferrite produced in any desired shape or size. It adds to the cost of the system substantially when the ferrite is required in a specific geometry. In induction ovens this problem is overcome by using ferrite bars. It is cheap and easy to obtain ferrite bars. In this part we used ferrite bars supplied to us by

Arçelik. These ferrite bars have sizes of 15 mm × 5 mm × 60 mm. To observe the dependence of the field enhancement on the area covered by the ferrite we analyzed the structures shown in Figure 4.5. In this figure backside of the coil

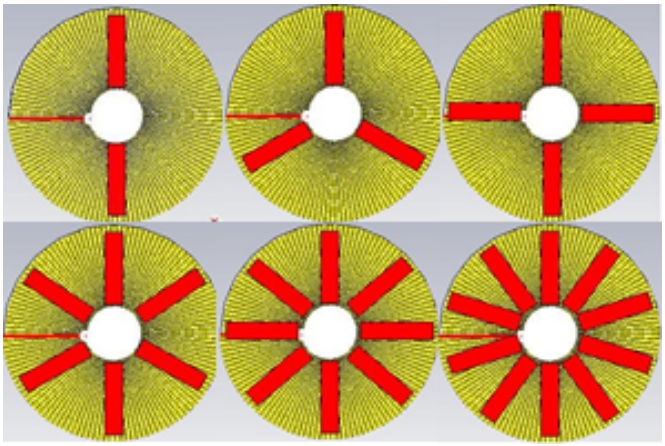

Figure 4.5: Generic illustration of the analyzed structures.

covered with different amounts of ferrite bars is shown. Red bars are the ferrite bars used for this analysis. The measurements and simulations were performed when the coil is loaded with both the aluminum and ferromagnetic steel with properties mentioned in the previous sections. Change in B_z and electrical loss in the load are recorded for all 6 cases shown above. The coil is driven at 100 kHz and the field measurements are taken below the load and 5 mm above the coil.

Figures 4.6- 4.11 show numerical and experimental measurement of B_z for different ferrite coverage of the coil. The color scales of all these figures are the same so that a direct comparison of colors indicates the relative magnitude of B_z in each situation. Each ferrite bar added under the coil enhances both B_z and the electrical loss in the load around the location where it is placed.

As the number of ferrite bars used increases, the enhancement of B_z becomes more homogeneous around the center of the coil. The improvement in the electrical loss in the load is not linearly proportional with the number of ferrite bars used. Figure 4.12 shows the change in average induced voltage in the pickup coil with respect to the number of ferrite bars used both in the aluminum and ferromagnetic steel cases. The improvement in the average magnetic field when

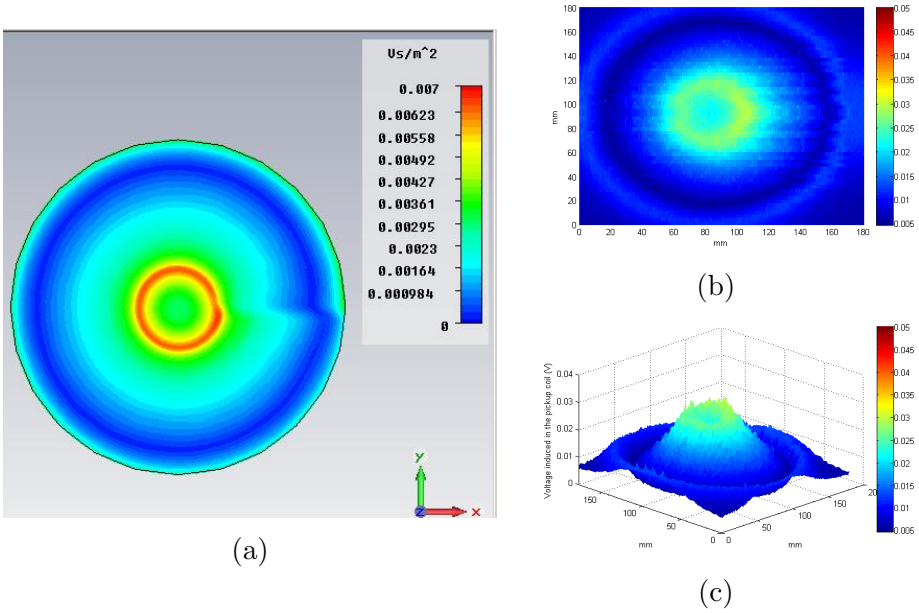

(a) (b) (c)

Figure 4.6: Surface scan of B_z at 5 mm above Coil 1 loaded with the ferromagnetic steel, **no ferrite bar is used**: (a) simulation, (b) measurement top-view and (c) measurement perspective-view.

10 ferrite bars are used is about 40% for the ferromagnetic steel case. As we have shown in Figure 4.1, the maximum gain attainable is around 60% and 10 ferrite bars only cover 36% of the coil area. This shows that as the number of ferrite bars increases, the differential improvement in the B_z diminishes and the overall improvement is saturated. To benefit almost full improvement from the ferrite bars we need to use approximately 27 ferrite bars for 60% improvement. When we consider the ferrite cost versus the benefit we obtain from the ferrite, using excessively more than 10 ferrite bars simply increases the cost of the system unnecessarily.

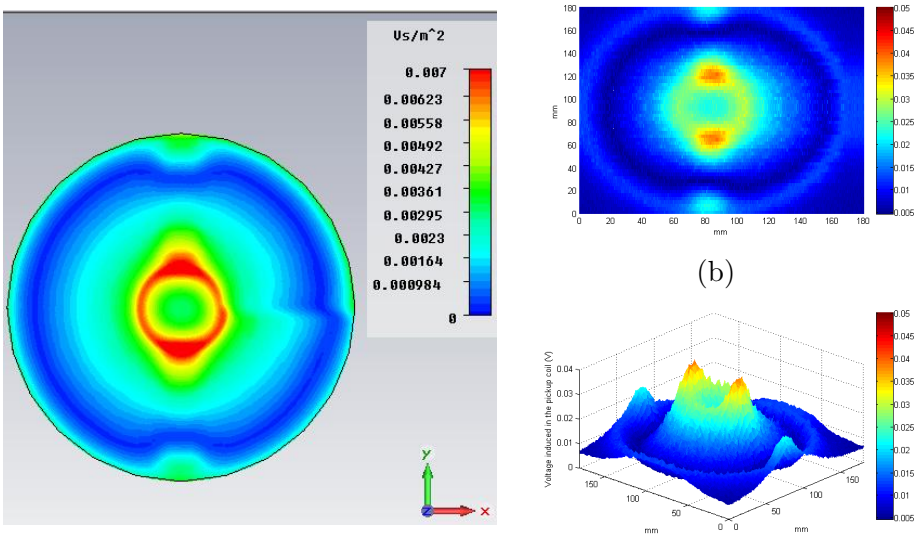

(a) (b) (c)

Figure 4.7: Surface scan of B_z at 5 mm above Coil 1 loaded with the ferromagnetic steel, **2 ferrite bars are used**: (a) simulation, (b) measurement top-view and (c) measurement perspective-view.

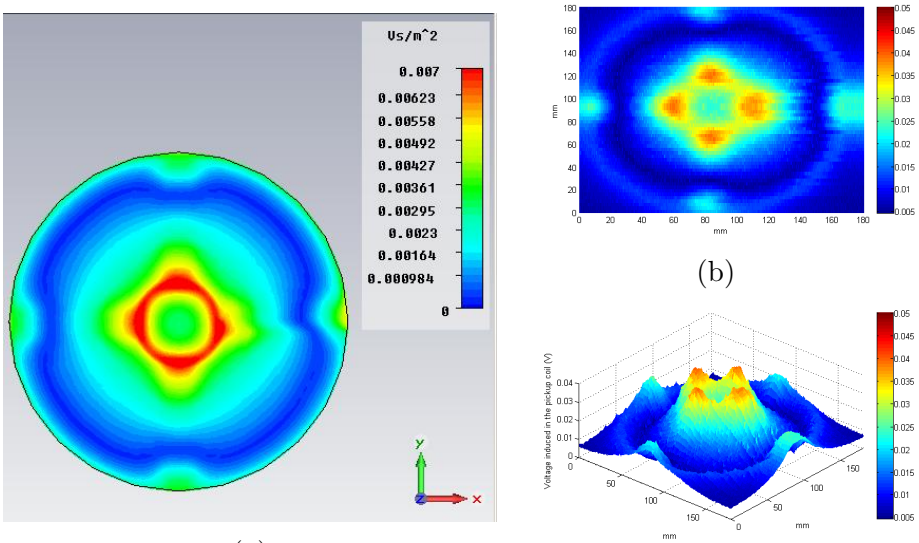

(a) (b) (c)

Figure 4.8: Surface scan of B_z at 5 mm above Coil 1 loaded with the ferromagnetic steel, **4 ferrite bars are used**: (a) simulation, (b) measurement top-view and (c) measurement perspective-view.

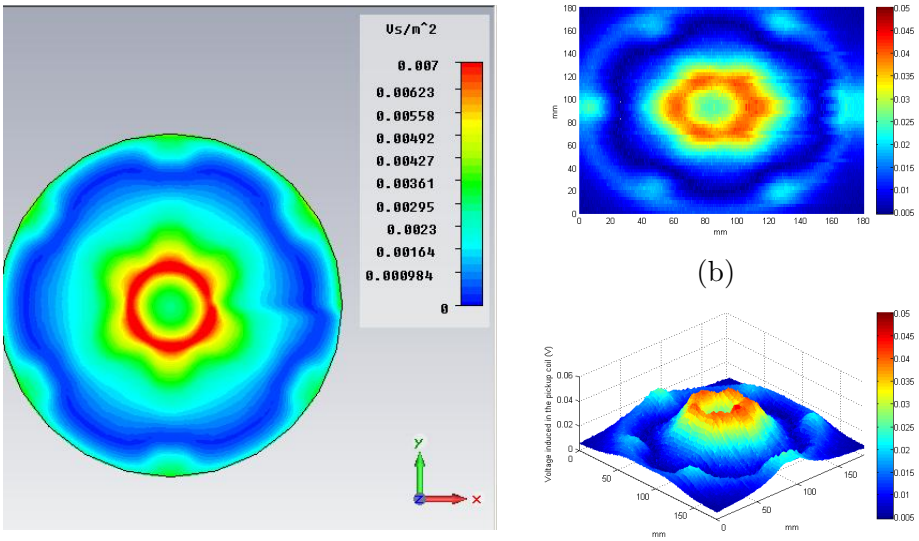

(a) (b) (c)

Figure 4.9: Surface scan of B_z at 5 mm above Coil 1 loaded with the ferromagnetic steel, **6 ferrite bars are used**: (a) simulation, (b) measurement top-view and (c) measurement perspective-view.

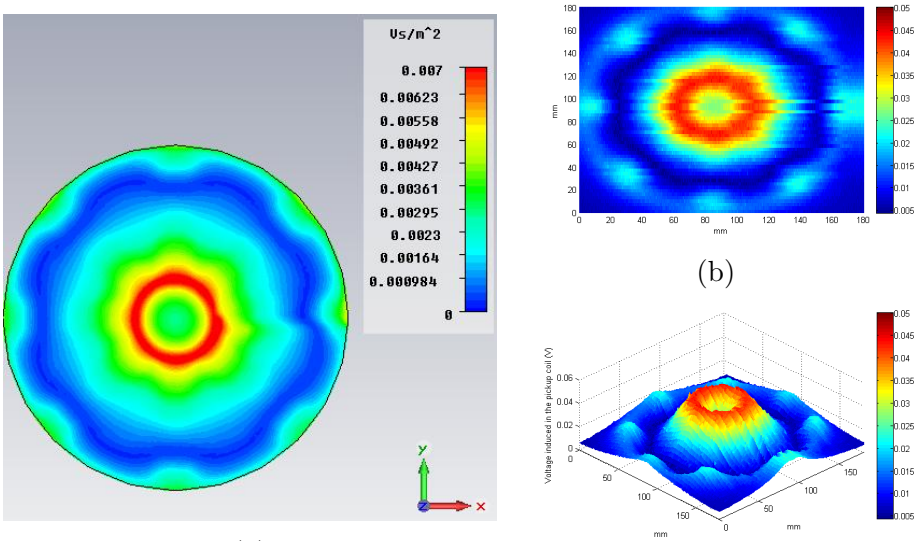

(a) (b) (c)

Figure 4.10: Surface scan of B_z at 5 mm above Coil 1 loaded with the ferromagnetic steel, **8 ferrite bars are used**: (a) simulation, (b) measurement top-view and (c) measurement perspective-view.

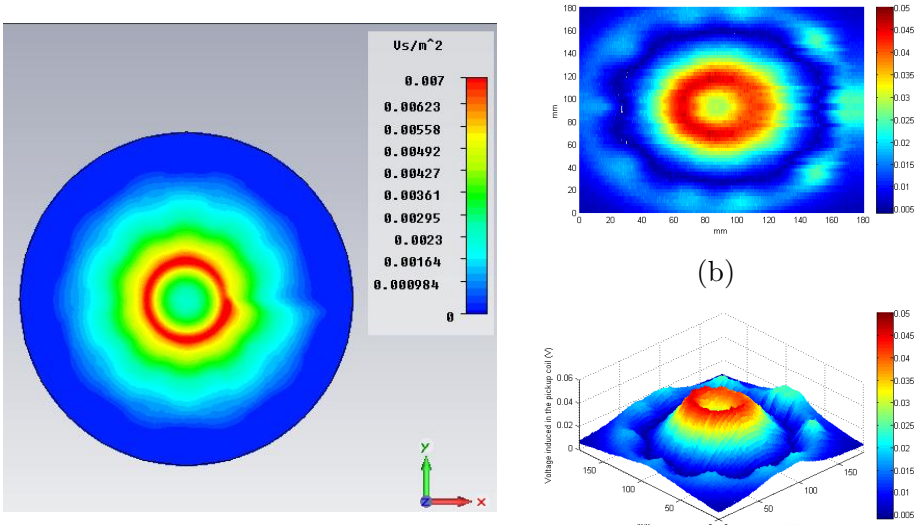

(a) (b) (c)

Figure 4.11: Surface scan of B_z at 5 mm above Coil 1 loaded with the ferromagnetic steel, **10 ferrite bars are used**: (a) simulation, (b) measurement top-view and (c) measurement perspective-view.

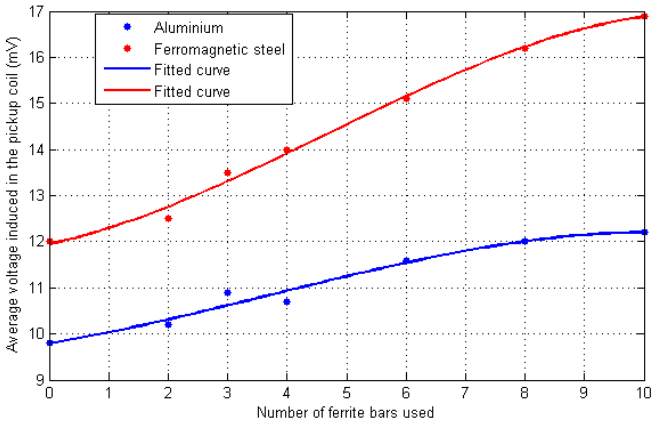

Figure 4.12: Change in the average induced voltage in pickup coil as a function of the number of ferrite bars.

Figure 4.13 shows the simulations results of the electrical loss in the load for the aluminum and ferromagnetic steel cases. The loss also tends to saturate as the number of ferrite bars increases. This result is totally consistent with our measurement results.

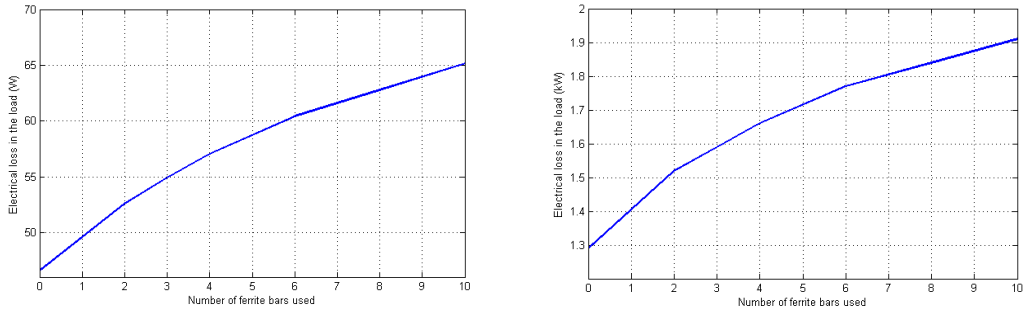

(a) (b)

Figure 4.13: Simulation results of change in the electrical loss in the load with increasing number of ferrite bars used with (a) aluminum load and (b)ferromagnetic steel load.

In the light of this analysis, if the cost of the ferrite is ignored, it is better to cover under the coil fully with ferrite. However, if the cost of ferrite is an issue, a compromise between the amount of ferrite to be used and the desired level of improvement in the heating must be made. This may change from system to system depending on the application. If an induction oven is designed to heat only ferromagnetic loads it may not be necessary to fully cover under the coil with ferrite because the efficiency of induction ovens when loaded with the ferromagnetic steel is already high above 90% and adding extra ferrite bars (more than 8 to 10) does not improve the efficiency significantly. On the other hand, if the system is to heat non ferromagnetic materials like aluminum and copper, then every bit of improvement in the efficiency is crucial and regardless of the cost full ferrite coverage of the coil may be a good choice. As mentioned above, another benefit of using ferrite is shielding the electronics below from the magnetic fields generated by the coil. Using a number of ferrite bars may not fully cover under the coil. In such cases magnetic fields may leak between the ferrite bars and harm the operation of the electronics beneath the coil. To prevent this, in such systems a couple of mm thick aluminum must be placed under the ferrite bars to avoid

this leakage.

4.2 Different ferrite placements with the same ferrite coverage

In the previous section we analyzed the effects of increasing ferrite coverage under the coil. The enhancement in the magnetic field and electrical loss in the load do not increase linearly, i.e.,the overall improvement saturates after about 8-10 ferrite bars. In this section, different ferrite placement schemes are investigated to obtain a better performance by keeping the number of ferrite bars constant. As

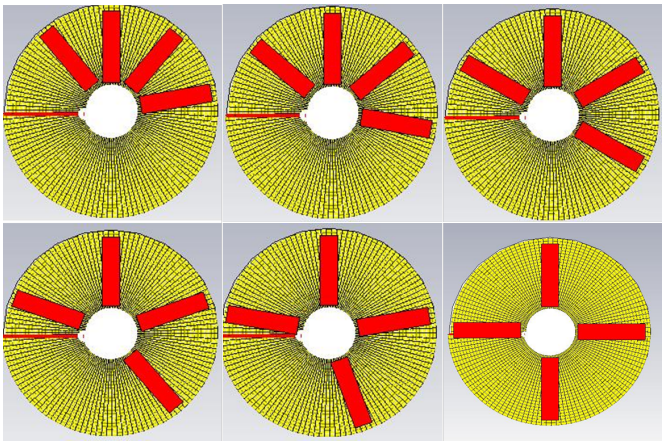

Figure 4.14: Generic illustration of the analyzed structures.

seen in Figure 4.14, four ferrite bars are used and the angle between ferrite bars is changed from 40°to 90°. Measurements and simulations are made with the same parameters as in the previous section. Coil 1 is driven at 100 kHz. Simulations and measurements are repeated for both the aluminum and ferromagnetic steel loads and we will only mention the results with the aluminum load since this is sufficient to make our point.

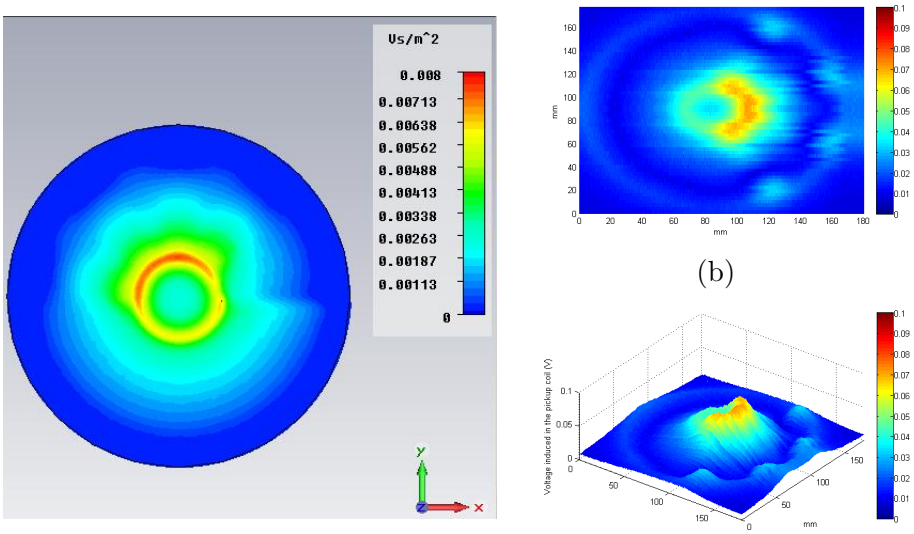

(a) (b) (c)

Figure 4.15: Surface scan of B_z at 5 mm above Coil 1 loaded with the aluminum when the **angle between the ferrite bars is 40°**: (a) simulation, (b) measurement top-view and (c) measurement perspective-view.

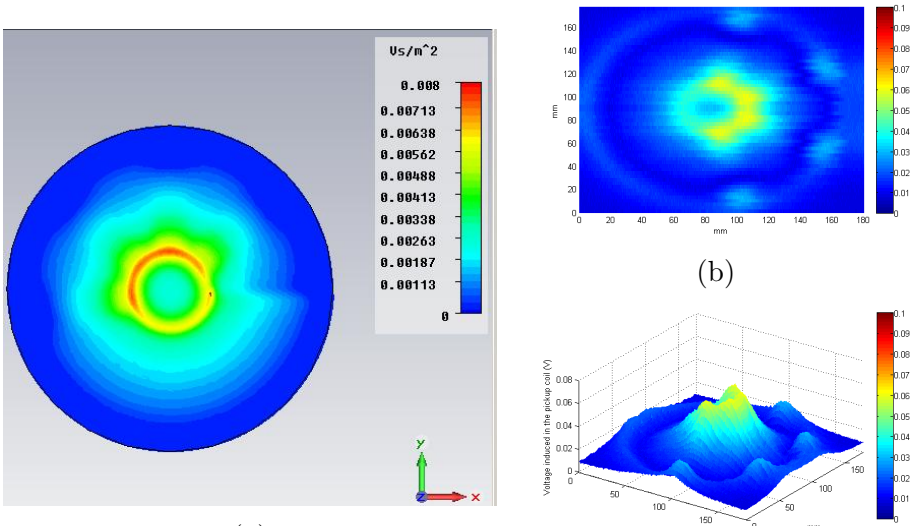

(a) (b) (c)

Figure 4.16: Surface scan of B_z at 5 mm above Coil 1 loaded with the aluminum when the **angle between the ferrite bars is 50°**: (a) simulation, (b) measurement top-view and (c) measurement perspective-view.

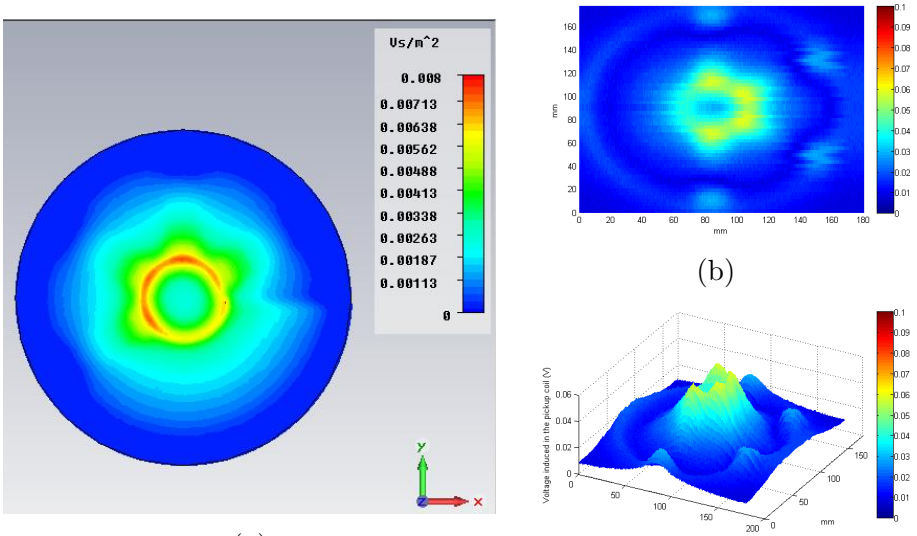

(a) (b) (c)

Figure 4.17: Surface scan of B_z at 5 mm above Coil 1 loaded with the aluminum when the **angle between the ferrite bars is 60°**: (a) simulation, (b) measurement top-view and (c) measurement perspective-view.

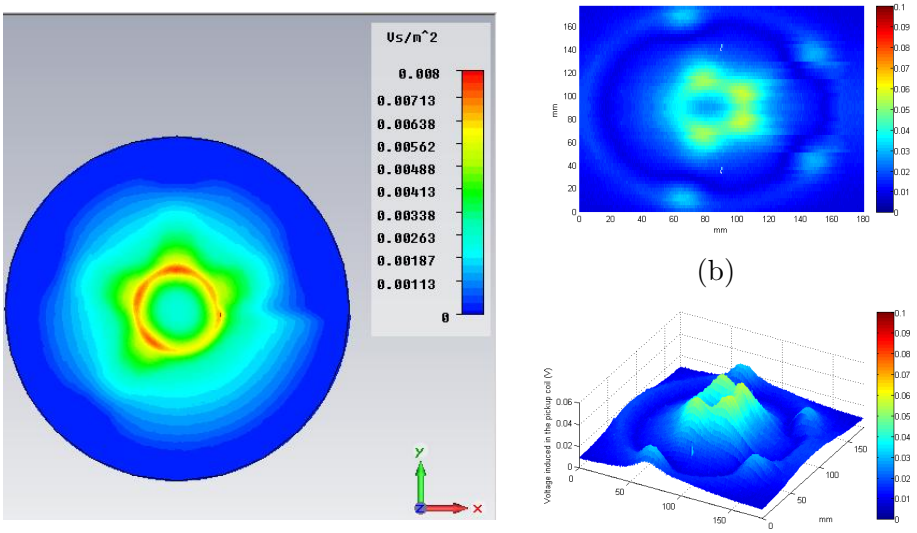

(a) (b) (c)

Figure 4.18: Surface scan of B_z at 5 mm above Coil 1 loaded with the aluminum when the **angle between the ferrite bars is 70°**: (a) simulation, (b) measurement top-view and (c) measurement perspective-view.

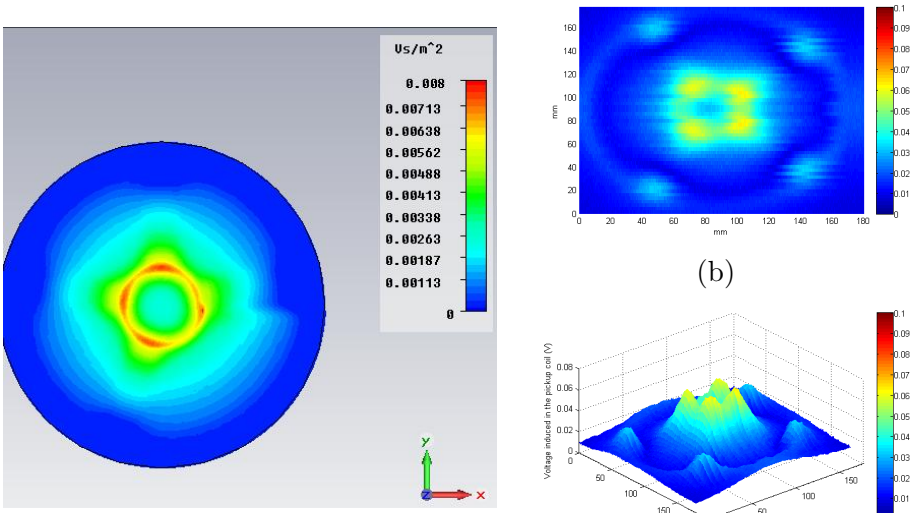

(a) (b) (c)

Figure 4.19: Surface scan of B_z at 5 mm above Coil 1 loaded with the aluminum when the **angle between the ferrite bars is 80°**: (a) simulation, (b) measurement top-view and (c) measurement perspective-view.

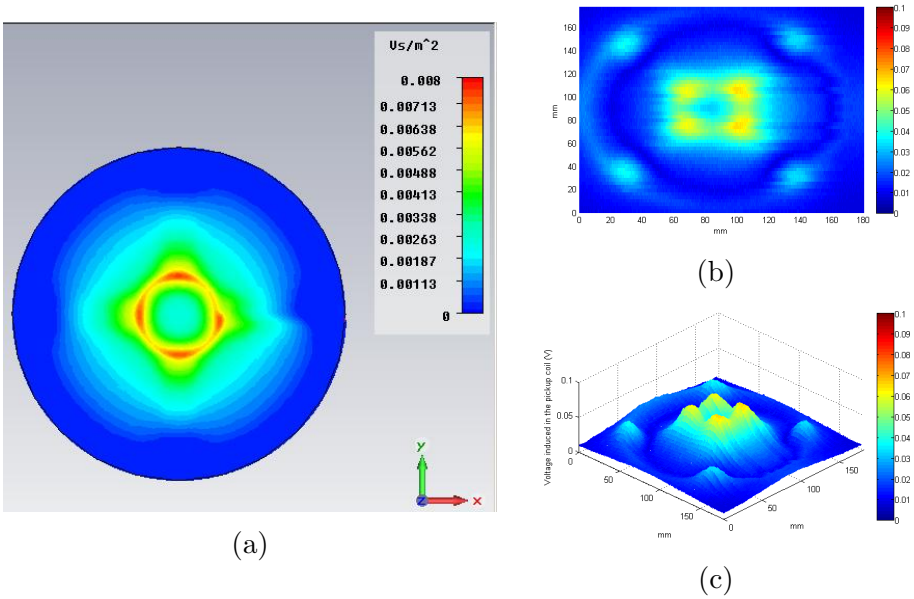

(a) (b) (c)

Figure 4.20: Surface scan of B_z at 5 mm above Coil 1 loaded with the aluminum when the **angle between the ferrite bars is 90°**: (a) simulation, (b) measurement top-view and (c) measurement perspective-view.

Figures 4.15 to 4.20 present measurement and simulation results for all 6 cases shown in Figure 4.14. Scales of color bars for all figures are set to the same level for a fair comparison between the figures. As the ferrite bars get further away from each other, the peak value of B_z becomes smaller; however, the average B_z throughout the structure increases. This is clearly seen in Figure 4.21. Due

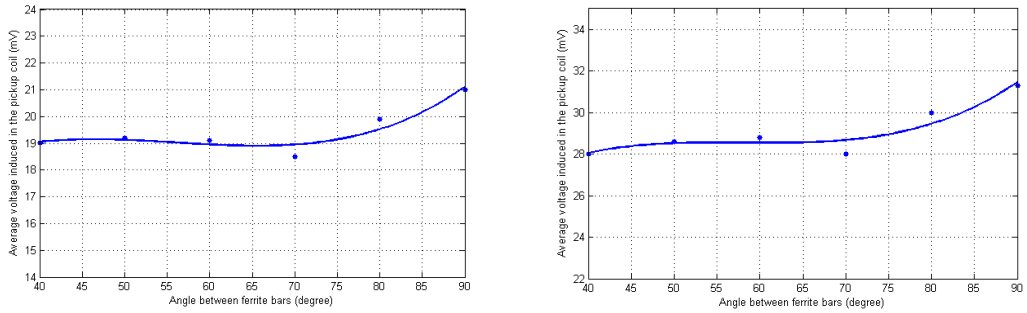

(a) (b)

Figure 4.21: Average voltage induced in the pickup coil at 5mm above Coil 1 loaded with the (a) aluminum and (b)ferromagnetic steel.

to experimental limitations, we could not drive the system with high enough current to see the increase in the average B_z as the angle between the ferrite bars is increased. This is due to the fact that improvement in B_z that we obtain from the placement of ferrite bars is very close to the measurement error we make. Still it is clear from the above figure that, when the ferrite bars are placed as far away from each other as possible (which is 90°for four ferrite bar case), B_z is improved the most.

Figure 4.22 shows the simulation results of electrical loss in the load when Coil 1 is driven at 100 kHz with a 20A constant current source. The improvement in the electrical loss in the load is more precisely seen here than in the measurement results since we could drive the coil with sufficiently high current in the simulation. The gain in the electrical loss is minor (2.7%) as mentioned above and that is why the coil is needed to be driven at sufficiently high current levels so that the improvement is above measurement error.

This proves the point that given a number of ferrite bars to be placed under the coil, ferrite bars need to be placed as far away from each other as possible and

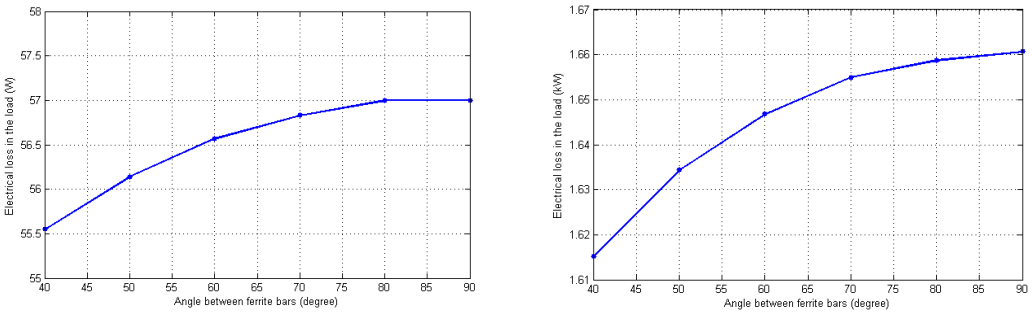

(a) (b)

Figure 4.22: Electrical loss in the load changing with the angle between the ferrite bars when Coil 1 is loaded with the (a) aluminum and (b)ferromagnetic steel.

this is true only when the ferrite bars are placed symmetric in the ϕ-direction given that the coil itself is symmetric. Given this, the next step for optimum ferrite placement is to check the effect of ferrite placement when the longest side of the ferrite bar is not aligned with the radial axis of the coil. To understand this, we analyzed three structures given in Figure 4.23. In these three analyzed structures, the angle that the longest side of the ferrite bar makes with the radial axis of the coil is 0°, 45°and 90°from left to right, respectively.

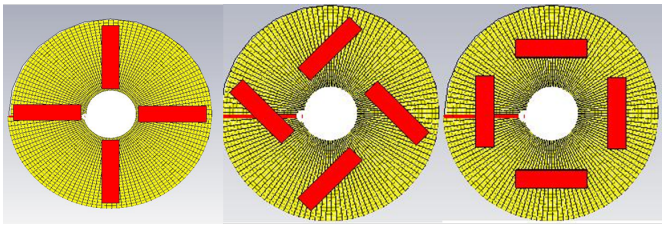

Figure 4.23: Generic illustration of the analyzed structures.

To observe the effects of such ferrite placement on B_z and electrical loss in the load we performed measurements and simulations using the exact setup and parameters that we used in the previous sections. Figures 4.24 to 4.26 show B_z for different angle values when the coil is loaded with the ferromagnetic steel.

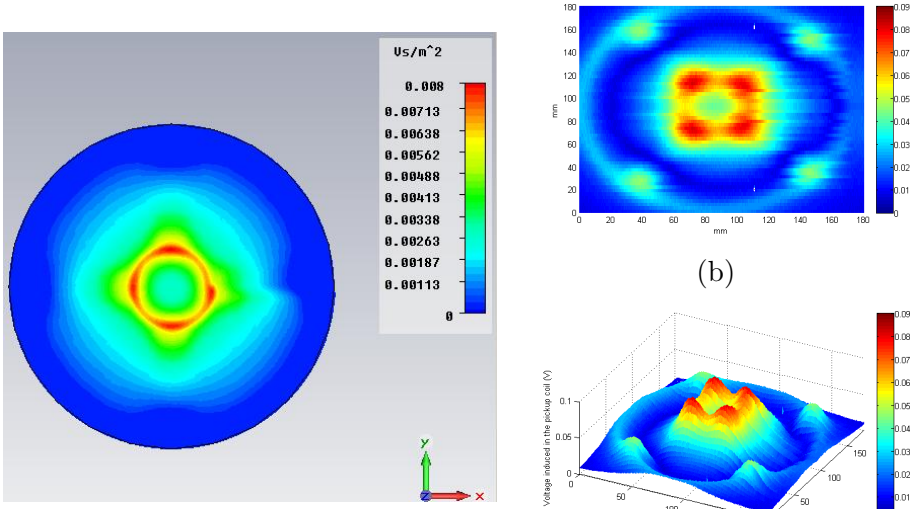

(a) (b) (c)

Figure 4.24: Surface scan of B_z at 5 mm above Coil 1 loaded with the ferromagnetic steel when the **angle between the longest side of the ferrite bar and coil radial axis is 0°**:(a) simulation, (b) measurement top view and (c) measurement perspective view.

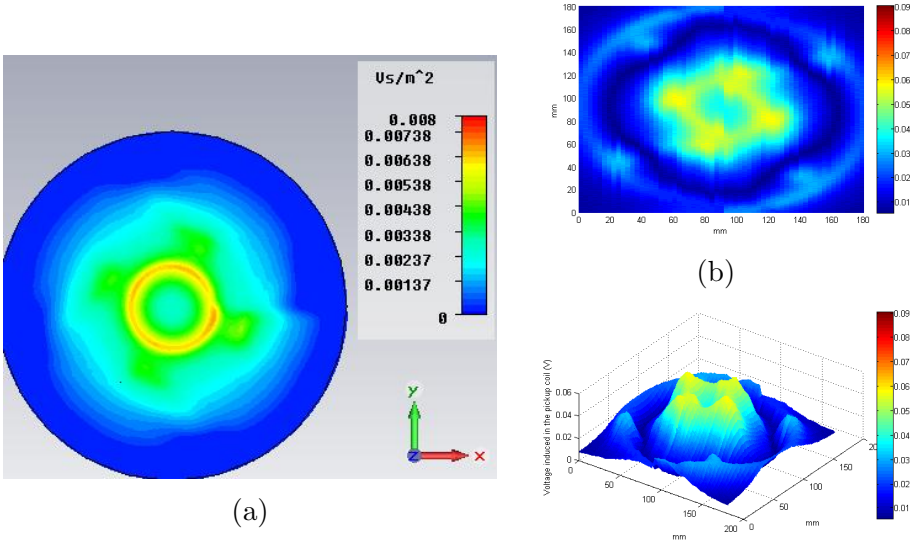

(a) (b) (c)

Figure 4.25: Surface scan of B_z at 5 mm above Coil 1 loaded with the ferromagnetic steel when the **angle between the longest side of the ferrite bar and coil radial axis is 45°**:(a) simulation, (b) measurement top view and (c) measurement perspective view.

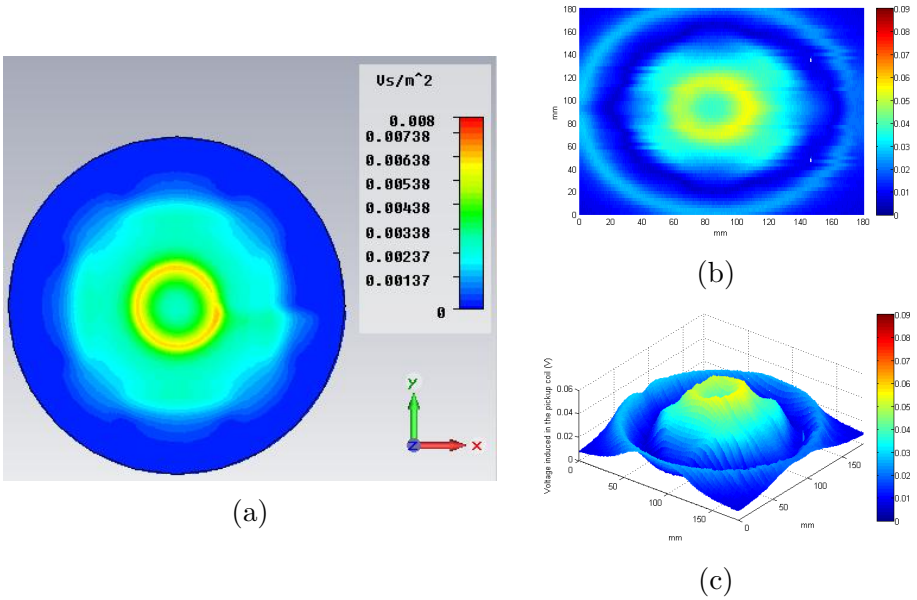

(a)

(b)

(c)

Figure 4.26: Surface scan of B_z at 5 mm above Coil 1 loaded with the ferromagnetic steel when the **angle between the longest side of the ferrite bar and coil radial axis is 90°**:(a) simulation, (b) measurement top view and (c) measurement perspective view.

It is clear from Figure 4.24 that, when ferrite bars are aligned with the radial axis of the coil, the most improvement in B_z is achieved. Figure 4.27 gives the measurement result of average voltage induced in the pickup coil for both the aluminum and ferromagnetic steel loads. It is apparent in this figure that the improvement when the coil is loaded with ferromagnetic steel is substantial. When the ferrite bars are aligned with the radial axis of the coil, the improvement in B_z with respect to the worst case (when the angle is 90°) is around 13.6% and 13% for the ferromagnetic steel and aluminum loads, respectively.

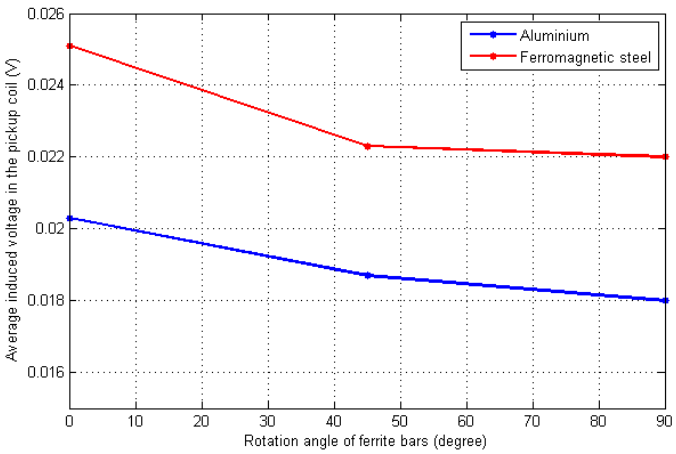

Figure 4.27: Average voltage induced in the pickup coil for different ferrite placements.

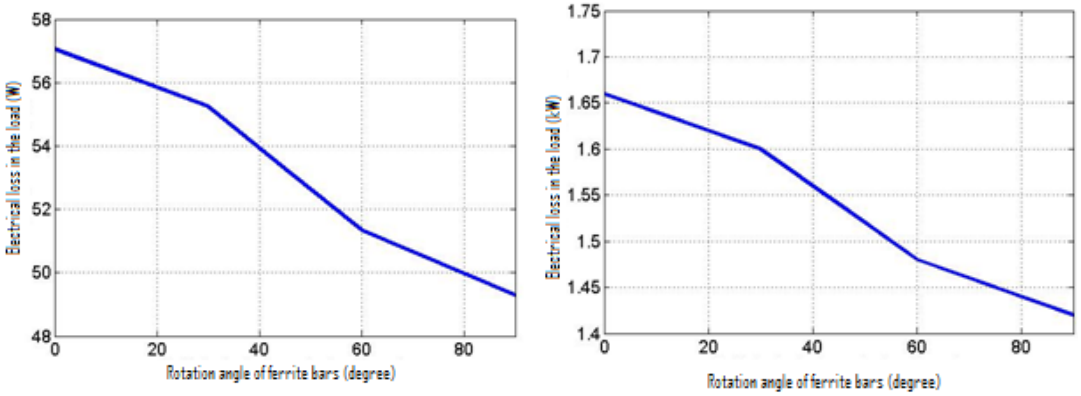

(a) (b)

Figure 4.28: Change in the electrical loss in the load with angle between the longest side of ferrite bar and coil radial axis when the coil is loaded with the (a) aluminum and (b)ferromagnetic steel.

Figure 4.28 shows the electrical loss in the load for different angles using both aluminum and ferromagnetic steel loads. Here as expected the improvement in the electrical loss for aluminum is about 15%, whereas it is 16.5% for the ferromagnetic steel.

As a result, to obtain the maximum improvement from utilization of ferrite bars, we have shown that ferrite bars should be placed symmetric in the ϕ-direction and their longest side should align with the radial axis of the coil. In the next section the effect of the ferrite thickness will be analyzed to see how it changes performance improvement.

4.3 Effect of ferrite thickness on electrical loss in the load and B_z

In the previous section we have shown that, when only four ferrite bars are to be placed under the coil, these ferrite bars need to be placed symmetric in the ϕ-direction and the longest side of these ferrite bars need to be aligned with the radial axis of the coil to obtain the most improvement out of ferrite. To understand the effect of the thickness of the ferrite bars on performance improvement of the coil, we analyzed three structures shown in Figure 4.29. Since we have

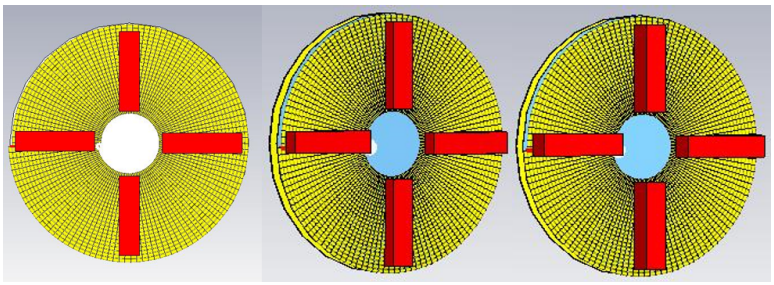

Figure 4.29: Generic illustration of the analyzed structures.

only one type of ferrite bar of thickness 5 mm, in our measurements we could test ferrite thicknesses in integer multiples of 5 mm. Figure 4.29 shows ferrite thicknesses of 5, 10 and 15 mm from left to right, respectively. The measurements

and simulations are performed using the same setup and parameters used in the previous parts.

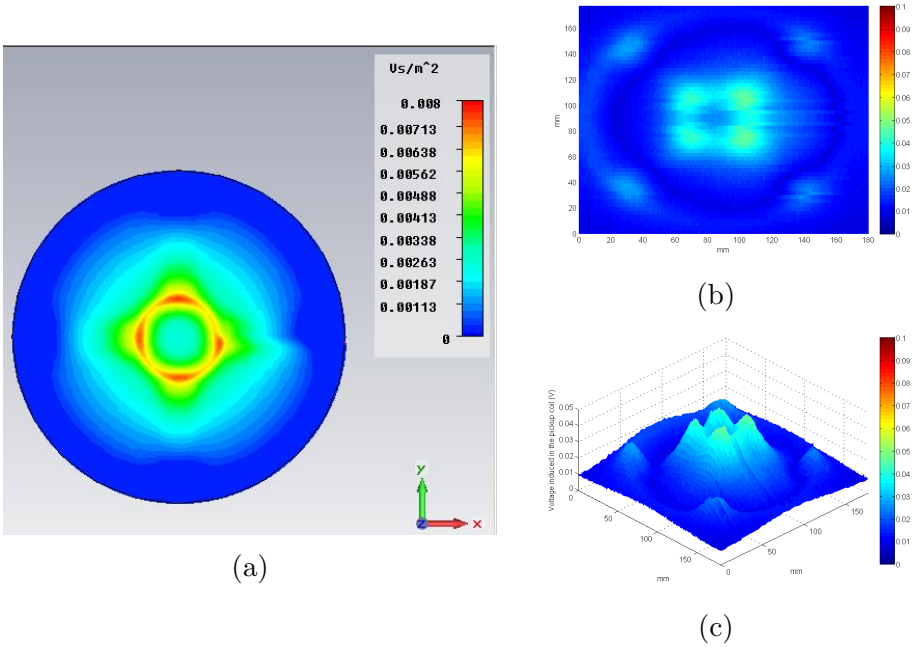

(a)

(b)

(c)

Figure 4.30: Surface scan of B_z at 5 mm above Coil 1 loaded with the aluminum, when the **ferrite thickness is** 5 **mm**: (a) simulation, (b) measurement top-view and (c) measurement perspective-view.

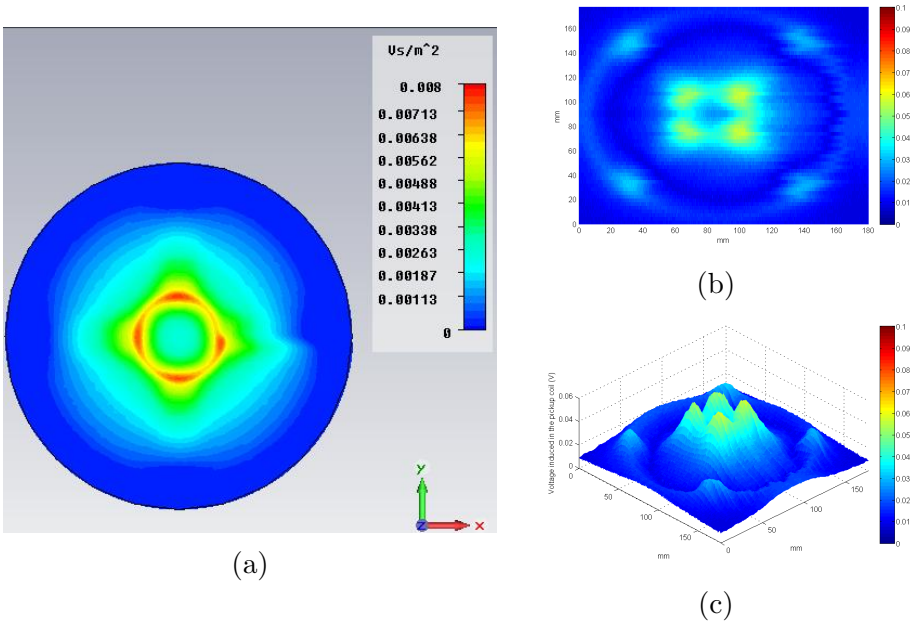

(a)

(b)

(c)

Figure 4.31: Surface scan of B_z at 5 mm above Coil 1 loaded with the aluminum, when the **ferrite thickness is** 10 **mm**: (a) simulation, (b) measurement top-view and (c) measurement perspective-view.

Figures 4.30 to 4.32 show B_z at 5 mm above the coil when loaded with the aluminum for different ferrite thicknesses. When the ferrite thickness is increased from 5 to 10 mm, the improvement in the B_z is much more significant than the improvement in B_z when the ferrite thickness is increased from 10 to 15 mm. This suggests that for the specific type of ferrite bars we used in our measurements, the ferrite thickness somewhere in the range of 5 to 10 mm is reasonable. This can be clearly seen in Figure 4.33 where average voltage induced in the pickup coil throughout the whole structure is calculated. The improvement in B_z is about 6% when the ferrite thickness increased from 5 to 10 mm, whereas this is only 0.5% for the thickness increase from 10 to 15 mm.

The numeric results shown in Figure 4.34 confirm the measurement results. In Figure 4.34 the electrical loss in the load is shown for varying ferrite thickness. Here since we could vary the ferrite thickness in small intervals, the resulting resolution is much better than that in the measurements. The electrical loss in the aluminum is increased by 2.42% when the ferrite thickness is increased from 5 to 10 mm. The same improvement is only 0.8% for the thickness increased from

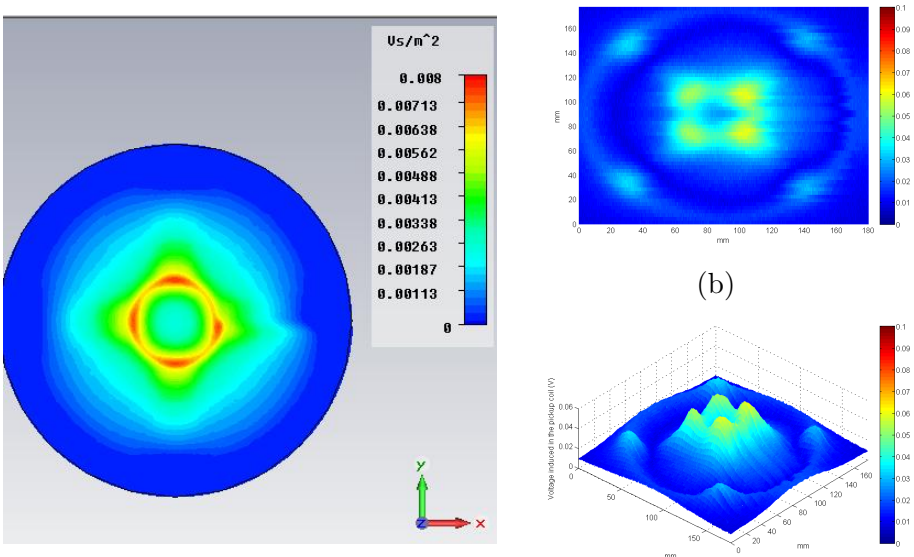

(a) (b) (c)

Figure 4.32: Surface scan of B_z at 5 mm above Coil 1 loaded with the aluminum, when the **ferrite thickness is** 15 **mm**: (a) simulation, (b) measurement top-view and (c) measurement perspective-view.

10 to 15 mm. The reason for the difference in the improvement in measurements and numerical analysis is due to the assumed μ_r of ferrite bars. In the numerical analysis as mentioned in the beginning of this chapter we took $\mu_r = 500$, however we do not exactly know μ_r of the ferrite bars. As it is described in the beginning of this chapter, for the same thickness increase, ferrite bars with lower μ_r value improves the loss in the load more. This means the ferrite bars we used in our measurements have μ_r smaller than the assumed value of 500.

Thus far we have analyzed ferrite placement under the coil and determined that totally covering the coil with ferrite is not necessary for the maximum performance improvement/cost ratio. In addition, the ferrite bars to be placed under the coil should be symmetrically placed in the ϕ-direction with their longest side being parallel to the radial axis of the coil. Since ferrite is not transparent to magnetic fields, ferrite placement between load and the coil is not a good idea and ferrite would degrade the performance instead of increasing it as shown in the next section.

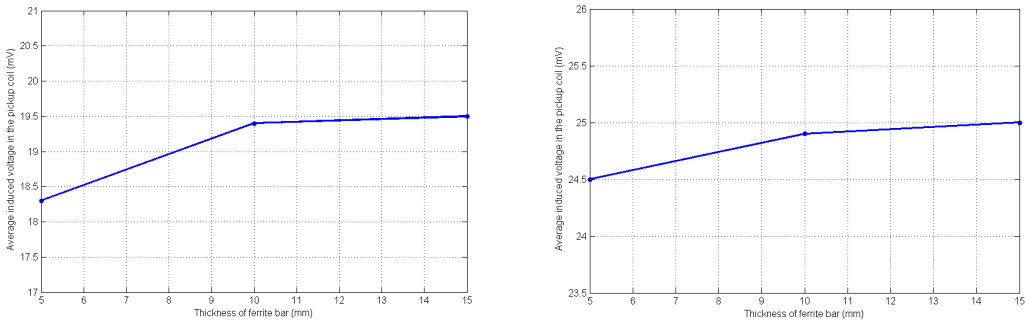

(a) (b)

Figure 4.33: Experimentally measured average voltage induced in the pickup coil using different ferrite thicknesses when the coil is loaded with the (a) aluminum and (b)ferromagnetic steel.

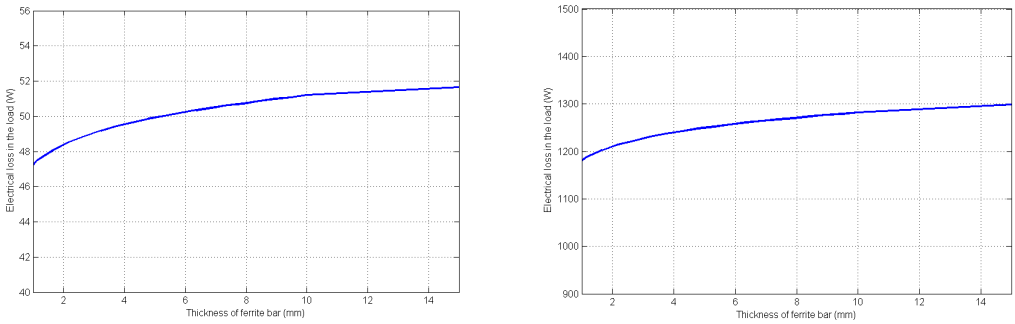

(a) (b)

Figure 4.34: Numerically simulated change in the electrical loss in the load as a function of ferrite thickness when the coil is loaded with the (a) aluminum and (b)ferromagnetic steel.

In the next section we will analyze ferrite placement around the outer and inner peripheral of the coil by putting the largest cross section of the ferrite perpendicular to the plane of the coil.

4.4 Analysis of different ferrite stacking techniques in three dimensions

Up to this point we only considered ferrite placement under the coil and obtained the optimum placement of ferrite bars for maximum performance enhancement. In this part we analyzed different ferrite stacking schemes as shown in Figure 4.35. There are three different stacking techniques given in Figure 4.35. In all these

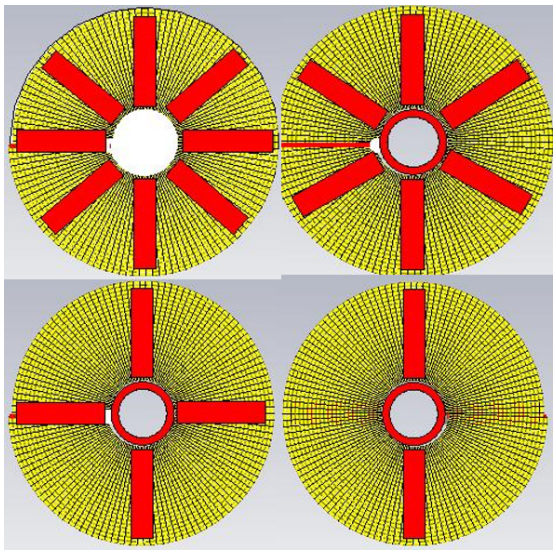

Figure 4.35: Generic illustration of the analyzed structures.

different stacking techniques we kept the number of ferrite bars used constant at 8. The top left stacking is the reference where all 8 bars are placed under the coil symmetrically in the ϕ-direction. In the top right stacking, 6 ferrite bars are put under the coil and two of them placed around the inner peripheral. The bottom two figures show back and front views of the same coil. The bottom left figure is the back-view showing the ferrite bars under the coil whereas the bottom right one is the front-view showing the two ferrite bars placed above the coil between load and the coil. In measurements we loaded the coil with both the aluminum and ferromagnetic steel and drived the coil at 100 kHz.

B_z measured in all these three ferrite stacking is shown in Figures 4.36 to 4.38. As it is immediately clear from Figure 4.38 the ferrite bars placed above the coil

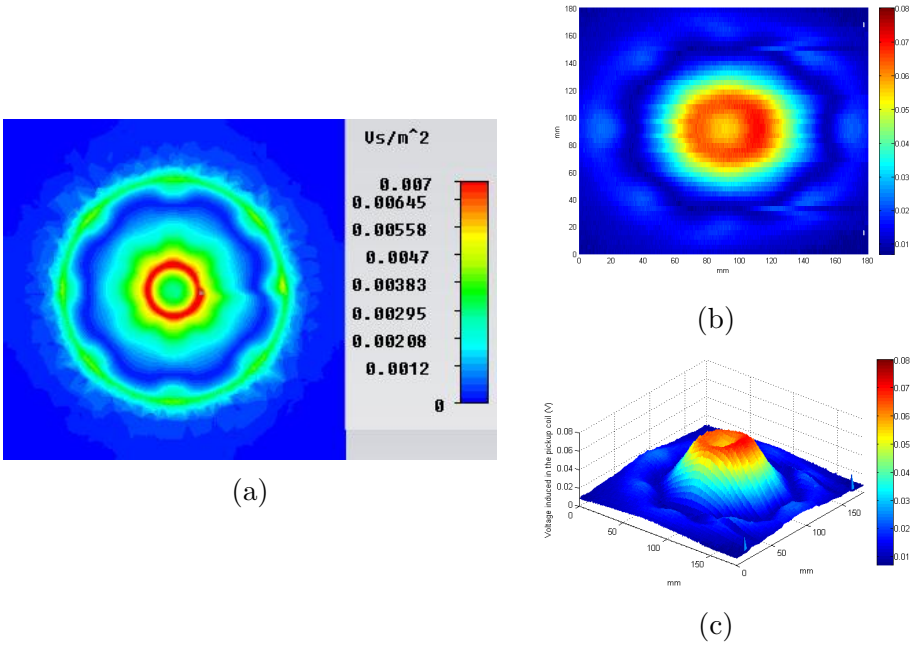

(a)

(b)

(c)

Figure 4.36: Surface scan of B_z at 5 mm above Coil 1 loaded with the ferromagnetic steel when **all** 8 **ferrite bars are placed under the coil**:(a) simulation, (b) measurement top-view and (c) measurement perspective-view.

block B_z and this degrades the performance. The ferrite bars placed around the inner peripheral of the coil increases the magnetic field around the inner radius of the coil at the expense of nonuniform heating because the magnetic field right where the ferrite is placed peaks locally compared to its surrounding, which in turn results in a nonuniform heating pattern.

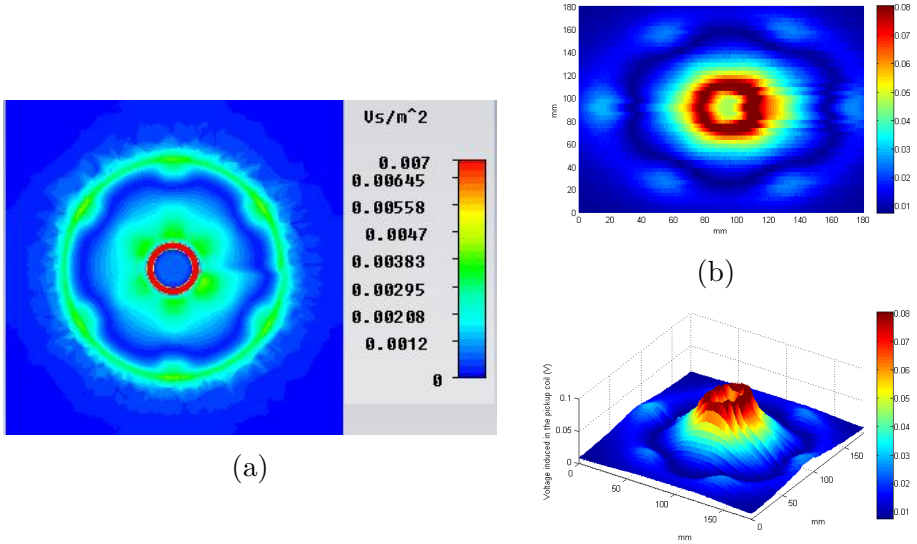

(a) (b) (c)

Figure 4.37: Surface scan of B_z at 5 mm above Coil 1 loaded with the ferromagnetic steel when 6 **ferrite bars are placed under the coil and** 2 **are placed around the inner peripheral**:(a) simulation, (b) measurement top-view and (c) measurement perspective-view.

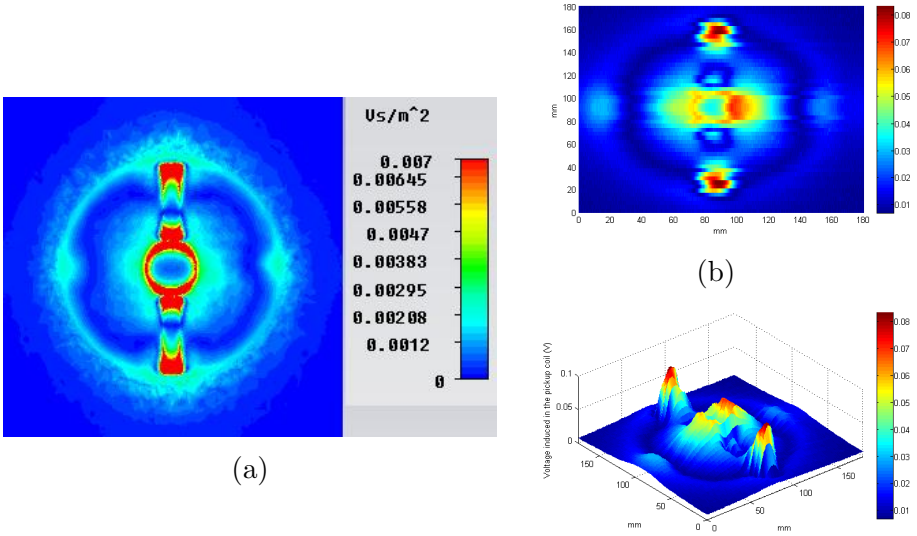

(a) (b) (c)

Figure 4.38: Surface scan of B_z at 5 mm above Coil 1 loaded with the ferromagnetic steel when 4 **ferrite bars are placed under the coil,** 2 **are placed around the inner peripheral and** 2 **are placed above the coil**:(a) simulation, (b) measurement top-view and (c) measurement perspective-view.

Table 4.1: Average voltage induced in the pickup coil.

Case	Aluminum loading(mV)	Ferromagnetic steel loading (mV)
1^{st} ferrite stacking	15.5	21.2
2^{nd} ferrite stacking	16.3	22.5
3^{rd} ferrite stacking	11.6	14.4

Table 4.1 shows the measurement results as the average voltage induced in the pickup coil. It is obvious that the 2^{nd} stacking where we placed 6 ferrite bars under the coil and 2 ferrite bars around the inner peripheral performs the best. It is also clear from these results that placing ferrite above the coil between coil and the load degrades the performance of the system substantially. This ferrite placement confines the magnetic field between the top ferrite placed above the coil and the bottom ferrite placed under the coil and this undesirably heats up the coil instead of the load.

Two other ferrite placements we analyzed is shown in Figure 4.39. In the left figure, four ferrite bars are placed under the coil and the remaining four ferrite bars are placed in the inner part of the coil where there are no windings. In the right figure, five ferrite bars are placed under the coil, two are placed around the inner peripheral of the coil, and the remaining one ferrite is split into small pieces and placed around the outer peripheral. The coil is loaded with both the

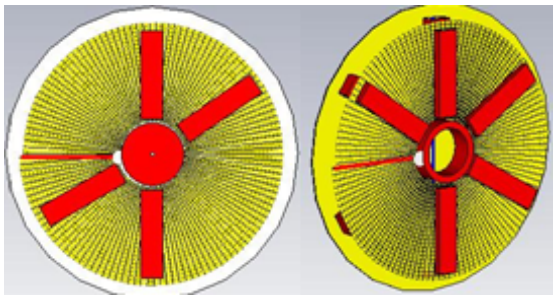

Figure 4.39: Generic illustration of the analyzed structures.

ferromagnetic steel and aluminum. We obtained the following results summarized in Table 4.2. The 4^{th} stacking scheme is the one shown on the left in Figure 4.39 while the 5^{th} stacking is the one on the right in the same figure. As seen in Table 4.2, 5^{th} stacking performs the best. Thus, instead of putting all the ferrite bars

Table 4.2: Electrical loss in the load.

Case	Aluminum loading(W)	Ferromagnetic steel loading (kW)
1^{st} ferrite stacking	62.79	1.84
2^{nd} ferrite stacking	66.43	1.98
3^{rd} ferrite stacking	61.95	1.64
4^{th} ferrite stacking	64	1.93
5^{th} ferrite stacking	68	2

under the coil, covering the inner and outer peripheral of coils with the ferrite bars first enhances the performance of the system the most. However, placing ferrite bars around the outer peripheral of the coil perpendicular to the coil requires some mechanical parts to hold the ferrite bars still. This may add to the cost of the system.

To sum up, if the number of ferrite bars to be used is constant or predetermined due to the cost concerns, the optimum way to place the ferrite bars is first to cover inner and outer peripheral of the coil and then place the remaining ferrite bars under the coil symmetric in the ϕ-direction with the longest side being parallel to the radial axis of the coil.

Chapter 5

High-Efficiency Coil Array Design for Inductive Heating

In induction cook tops, a common practice is to split the top of the oven into separate regions where only one vessel can be put and heated up on one of these regions. Each of these regions has only one coil beneath it. If the number of the coils can be increased and the electronics is adapted to many coils working together or separately, the whole surface of the cook top can be used for cooking. In other words, user does not have to put the vessel to be heated on any predetermined region for cooking. This is known as all-surface induction oven and it gives the user flexibility to use all of the top of the oven. This type of induction ovens is the new trend nowadays. In this type of ovens most of the time more than one coil powers up depending on the size of the vessel to be heated. Therefore, stacking of these coils is as important as the shape of the coils designed.

In this part we analyzed the first generation of coils used by Arçelik for all-surface heating purposes. Experimental measurements and numerical analyses are performed for one coil running by itself as well as two coils running next to each other. As we will mention shortly, due to the large size of these elliptic coils, the user is not provided with as much flexibility as expected from an all-surface oven. In addition, the efficiency of the oven could be increased with a better

design. In this part with the knowledge we gained in our studies described in previous chapters this thesis, we designed and implemented a high-efficiency coil array for all-surface induction heating.

5.1 Analysis of a single elliptic coil

Figure 5.1 shows the elliptic coil we analyzed in this part. This coil has 24-turns. The inner diameters along the major and minor axes are 137 and 25 mm, respectively. The outer diameter along the major and minor axes are 180 and 76 mm, respectively.

(a) (b)

Figure 5.1: Pictures of the elliptic coil:(a) front-view and (b) back-view.

We performed measurements and simulations with a single coil only at 100 kHz with 100 V_{rms} sine wave when the coil is unloaded and loaded with the ferromagnetic steel of $\sigma = 1.67 \times 10^6\ \Omega^{-1}m^{-1}$ and $\mu_r = 130$. The load has a thickness of 1 mm and it is placed 9 mm above the coil and measurements are always taken 5 mm above the coil for both the loaded and unloaded cases. The ferrite bars are modeled with $\mu_r = 500$ in simulations.

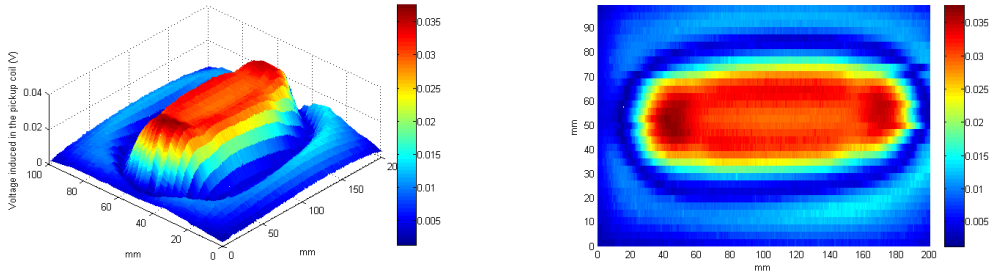

(a) (b)

Figure 5.2: All surface scan of B_z at 5 mm above the single unloaded elliptic coil:(a) measurement perspective-view and (b) measurement top-view.

Figure 5.2 shows B_z at 5 mm above the coil when the coil is unloaded. One point to notice in the figure is that around the tips of the ellipse B_z is the strongest. This is due to the fact that the windings around the tip of the ellipse are much densely wound than in any other region. The impedance of elliptic coil when unloaded is $0.813 + j76.46\ \Omega$ with an inductance value of 121.69 μH and an internal wire resistance of 0.813 Ω. The coil has its own ferrite placement as shown in Figure 5.1b, so all measurements are performed with this ferrite placement.

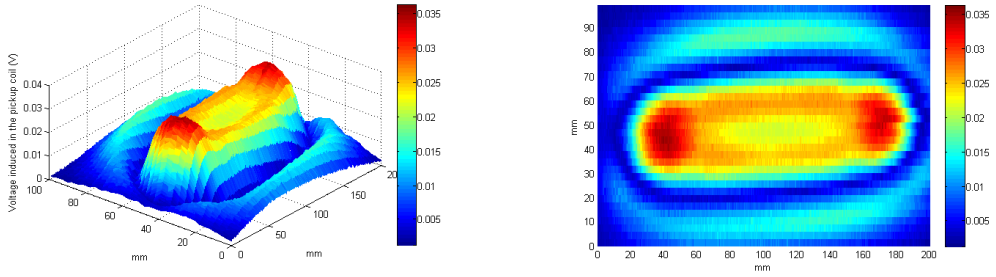

(a) (b)

Figure 5.3: All surface scan of B_z at 5 mm above the single elliptic coil loaded with the ferromagnetic steel:(a) measurement perspective-view and (b) measurement top-view.

Figure 5.3 shows surface scan of B_z at 5 mm above the coil when the coil is loaded with the ferromagnetic steel. Compared to the unloaded case, the magnetic field in the z-direction decreases substantially and the depth of the valley increases as expected. The impedance of the elliptic coil when loaded with

the ferromagnetic steel is $22.88 + j39.87\ \Omega$ with an inductance value of 63.49 μH and resistance of 22.88 Ω. The high value of resistance with respect to the internal resistance of the wire itself tells us that this coil is capable of heating up the ferromagnetic steel load quite efficiently. We can roughly say that efficiency of the system will be around $\frac{(22.88-0.81)}{22.88} \times 100 = 96.44\%$.

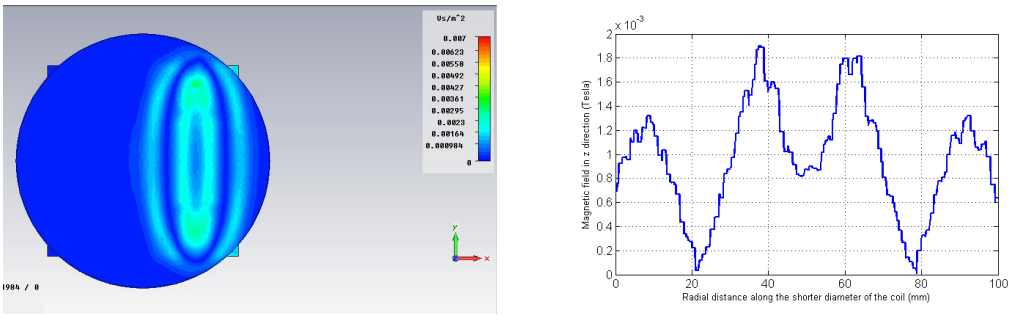

(a) (b)

Figure 5.4: Simulation results for B_z at 5 mm above the single elliptic coil loaded with the ferromagnetic steel:(a) surface scan of B_z and (b) B_z traced on the minor axis.

Figure 5.4 shows the simulation results for B_z along the minor axis at 5 mm above the coil. This B_z profile is consistent with the measurement result as expected. In all-surface ovens, most of the time more than a single coil will be powered depending on the size of the vessel. To better understand how two coils sitting next to each other react when both are powered up, we also performed analysis for the two coil case.

5.2 Analysis of double elliptic coils

In this part we analyzed two elliptic coils placed next to each other as seen in Figure 5.5. The separation between the coils is about 25 mm. Both of the coils are driven at 100 kHz with a $100V_{rms}$ sinusoidal signal. Measurements and simulations are performed for the loaded and unloaded cases. To observe how the coils interact with each other at different phase differences we repeated the measurements for 0°and 180°phase differences between the coils.

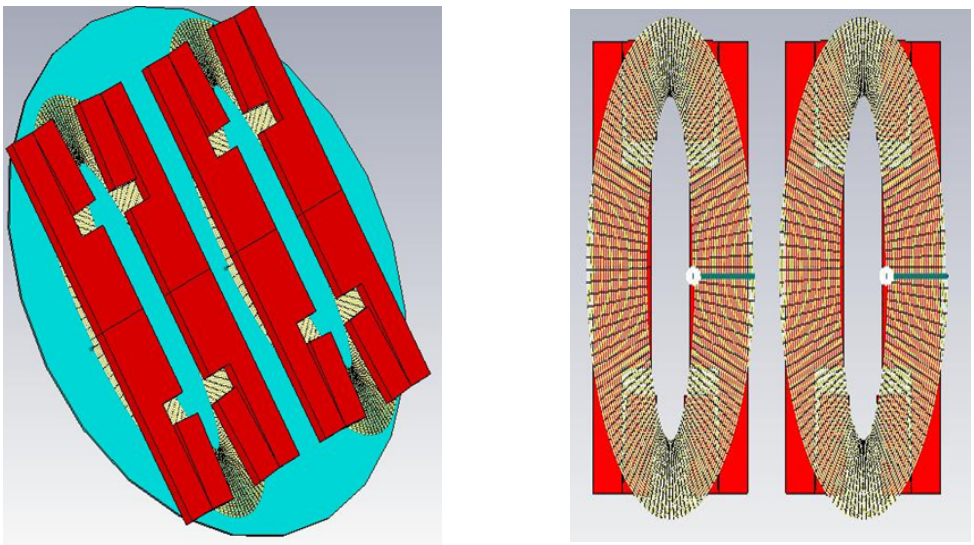

(a) (b)

Figure 5.5: Coil structure used for simulations:(a) perspective-view and (b) front-view.

Figures 5.6 and 5.7 show measurement and simulation results, respectively. In Figure 5.6 only one of the coils is shown. The other coil sits right next to it along the x-axis. It is clear that when the phase difference between coils is 0°, the magnetic field between the coils is suppressed. When the phase difference between the coils is 180°, the magnetic field between the coils is enhanced. Due to mutual coupling, effectively a third coil is produced between the two coils. We can easily conclude that feeding two neighboring coils with a phase difference of 180°enhances the efficiency of the system with respect to the 0°phase difference case. Due to positive mutual coupling, when the coils are driven at a 180°phase difference, it will be sufficient to feed the coils with less current than when the phase difference is 0°to deliver the same amount of power to the load. As a conclusion, to utilize the positive mutual coupling, neighboring coils should be fed at 180°phase differences.

Figure 5.8 shows measurement result of the surface scan of B_z when both coils are loaded with the ferromagnetic steel. Here, again the second coil sits along x-axis (long axis) next to the one seen in the figure. It is clearly seen here that the 0°phase difference suppresses the magnetic field between the coils also when they are loaded. The effect of positive mutual coupling goes along the x-axis

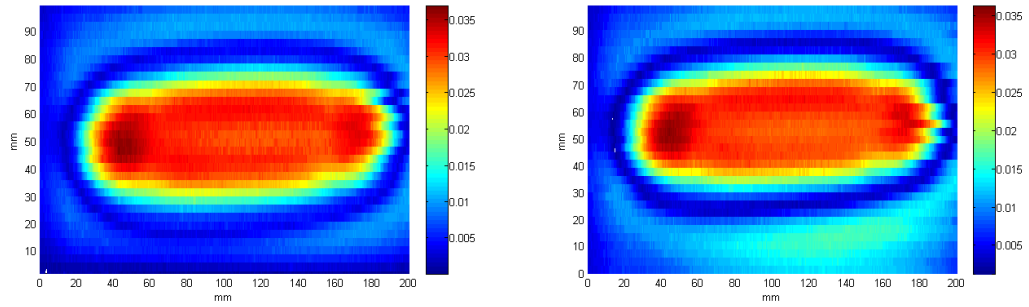

(a) (b)

Figure 5.6: Measured all surface scan of B_z at 5 mm above the two unloaded elliptic coils driven at a phase difference of (a) 0°and (b) 180°.

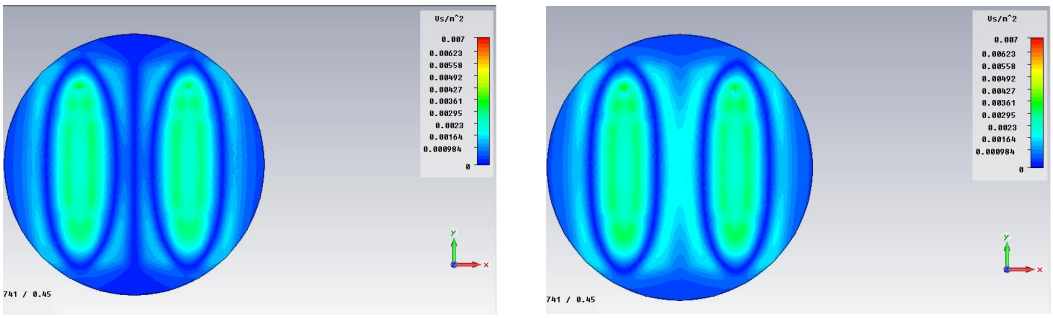

(a) (b)

Figure 5.7: Simulated all surface scan of B_z at 5 mm above the two unloaded elliptic coils driven at a phase difference of (a)0°and (b) 180°.

where windings of two neighboring coils are closer to each other and this positive interaction between the coils decreases as we move toward the tip of the coils where windings of neighboring coils are further away from each other.

Simulation results shown in Figure 5.9 supports the conclusions drawn above. To have a better understanding of the coupling effect between the coils we also performed some numerical analysis of B_z along the minor axis of the elliptic coils. Figure 5.10 summarizes the results for the single coil and the double two coils with a phase difference of 180°and 0°for both the loaded and unloaded cases. Along the x-axis, beyond 80 mm mark makes it the neighborhood of the next coil. For the unloaded case, driving the coils with a phase difference of 0°decreases B_z by about 43% with respect to the single coil case. On the other hand, driving the coils with 180°enhances B_z by about 49% with respect to the single coil case. For

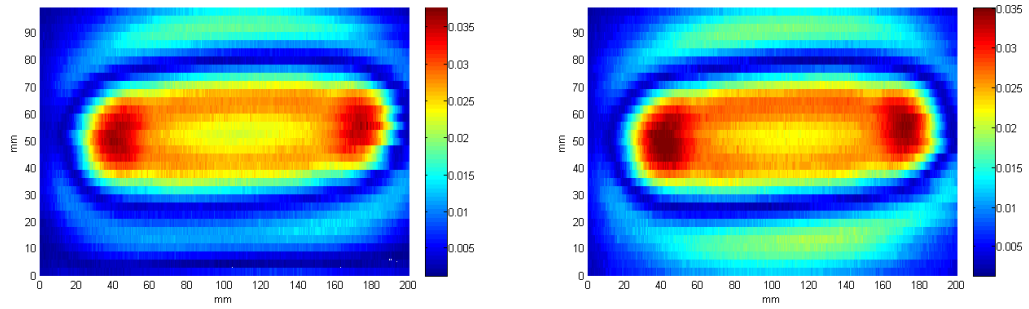

(a) (b)

Figure 5.8: Measured all surface scan of B_z at 5 mm above the two elliptic coils loaded with ferromagnetic steel(a) at 0°and (b) at 180°.

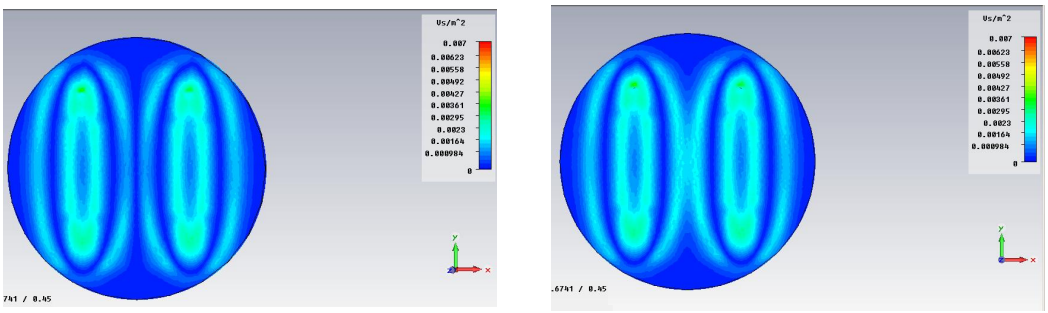

(a) (b)

Figure 5.9: Simulated all surface scan of B_z at 5 mm above the two elliptic coils loaded with ferromagnetic steel and driven at a phase difference of (a) 0°and (b)180°.

the loaded case, these values are 25% and 27%, respectively.

Clearly driving the coils with a phase difference of 180° significantly increases the power delivered to the load. One important point to make here in Figure 5.10 is that the effect of the mutual coupling disappears as we move towards the center of either coil. The analysis in Figure 5.10 is performed right on the minor axis of the coils where the windings of both coils are the closest to each other. This is where we get the most coupling effect. As seen in Figure 5.11, as we get far away from the center minor axis of the ellipse windings of both, coils get further away from each other decreasing the effect of positive mutual coupling. Figure 5.11 depicts the coupling effect about 50 mm above the center minor axis and B_z here is improved by only 18%.

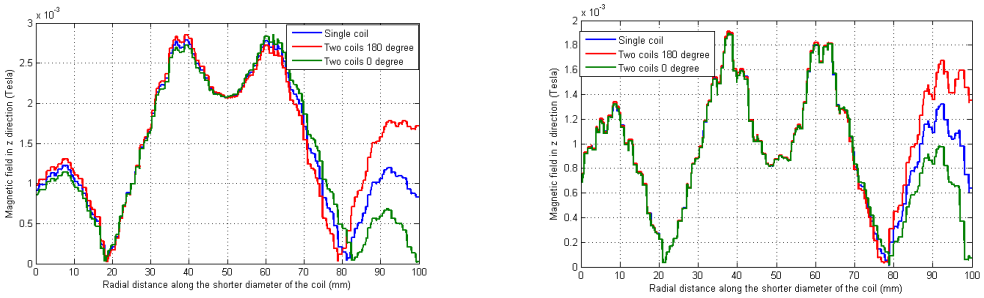

(a) (b)

Figure 5.10: Measured B_z at 5 mm above the single and double elliptic coils when the coils are (a)unloaded and (b)loaded with the ferromagnetic steel.

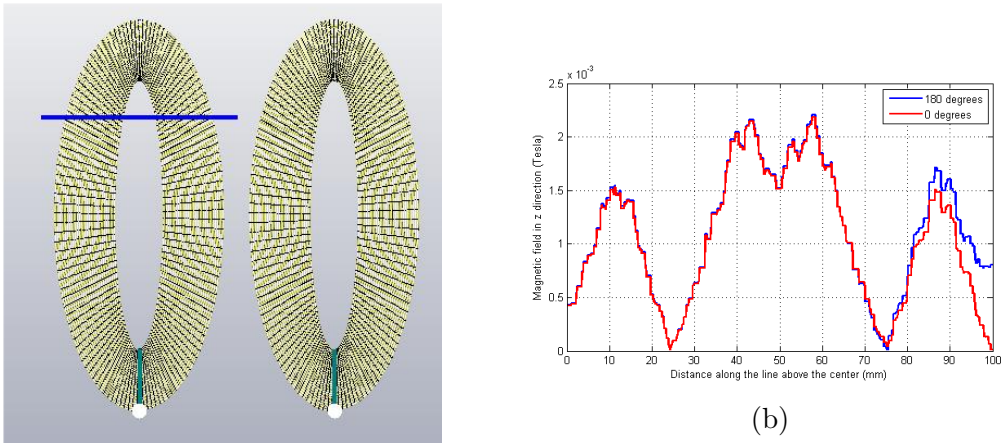

(a) (b)

Figure 5.11: (a) Illustration of the direction along which B_z is measured and (b)B_z at 5 mm above the double elliptic coils along the blue line when the coils are loaded with the ferromagnetic steel.

Chapter 6

Conclusion

To understand the working principle of an inductive heating system, multiple coils are electromagnetically analyzed. First of all, analytical derivation of the fields for a general inductive heating system is performed and these analytical expressions are numerically solved to observe the behavior of the fields and their dependence on the critical parameters such as physical, electrical and magnetic properties of the load and ferrite, number of turns, inner and outer radii of the coil, distance between the load, coil and ferrite. Secondly, an experimental setup is formed and numerical results are experimentally confirmed. It is shown that using a rectangular wire cross-section in a coil helps to fit a larger number of turns on a given surface area than using circular wire cross-section. It is also shown that, in order to heat non-ferromagnetic materials, multi-layer, high-turn coils are required with large inductance values. However, the efficiency of the system while heating non-ferromagnetic materials like aluminum and copper is still very low ($< 50\%$) compared to the system heating ferromagnetic steel. The heating profile of the load can be made more uniform if a pancake type coil is used. The space between the inner and outer coils in a pancake structure makes this possible. The effect of inner and outer radii in a coil loaded with ferromagnetic steel is also investigated both numerically and experimentally, under two different scenarios. For this purpose a prototype structure is fabricated, which enables us to form coils with different inner and outer radii. In the first scenario, the inner radius of

the coil is changed while keeping the number of turns constant. It is observed that as the inner radius increases keeping the number of turns constant, the efficiency increases as long as the outer diameter of the coil is less than or equal to the load diameter. In the second scenario, the length of the wire to form the coil is kept constant and in this case it is observed that as the inner radius increases the efficiency of the coil decreases. Therefore, unless there is a restriction on either the length of the wire or the number of turns, the best practice to form the coil is to keep the inner radius as small as practically possible and ending the coil at an outer diameter equal to or less than that of the load to be heated. Ferrite placement is also investigated for optimum performance enhancement. Here it is shown that for a given number of ferrite bars it is possible to achieve better performance enhancement by first placing the ferrite bars around the inner and outer peripheral of the coil and then placing the rest under the coil. Most of the time, common practice in the ferrite placement is to cover under the coil with ferrite; however this is not the optimal placement. Also, mutual coupling between coils in a coil array for all-surface induction oven is studied. It is shown that mutual coupling between coils in an array can be utilized to increase the efficiency of the coil array. Keeping the adjacent coils out of phase, effectively forms a third coil in between the out-of-phase coils. This eases the power delivery to the load. In other words, compared to conventional coil arrays, about 40% more power to the load can be delivered at the same injected current levels using high-efficiency coil arrays. As future work, the number of strands in copper wires that form the windings will be optimized to minimize copper losses in the coil. In addition to this, a new algorithm for metal recognition will be developed because inductance value of the coil when unloaded must be the highest inductance value of the system for the currently used algorithm to work properly. However, when using a coil array, this may not necessarily be so. This thesis work showed that the proposed high-efficiency coil array holds great promise for flexible inductive heating.

Bibliography

[1] C. N. H. G. H. Brown and R. A. Biewirth, "Theory and application of radio-frequency heating," *D. Van Nostrand Company, New York*, 1947.

[2] S. L. S. S. Zinn, "Elements of induction heating design, control, and applications," *ASM International, Electric Power Research Institute*, 1988.

[3] W. C. Moreland, "The induction range: its performance and its development problems," *IEEE Trans. on Industry Applications*, vol. IA-9, no. 1, pp. 81 – 85, 1973.

[4] L. Hobson and D. W. Tebb, "Transistorized power supply for induction heating," *Int. Journal Electronics*, vol. 59, no. 6, pp. 533 – 542, 1985.

[5] F. P. Dawson and P. Jain, "A comparison of load commutated inverter system for induction heating and melting applications," *IEEE Trans. Power Electronics*, vol. 6, no. 4, pp. 430 – 441, 1991.

[6] J. D. V. W. H. W. Koertzen and J. A. Ferreira, "Design of the halfbridge, series resonant converter for induction cooking," *IEEE Power Electronics Specialist Conference*, pp. 729 – 735, 1995.

[7] D. W. T. L. Hobson and F. G. Turnbull, "Dual element induction cooking unit using power mosfets," *Int. Journal Electronics*, vol. 59, no. 6, pp. 747 – 757, 1985.

[8] S. Y. M. Kamli and M.Abe, "A 50-150 khz half-bridge inverter for induction heating applications," *IEEE Trans. Industrial Electronics*, vol. 43, no. 1, pp. 163 – 172, 1996.

[9] S. Wang, "Induction-heated cooking appliance using new quasiresonant zvs-pwm inverter with power factor correction," *IEEE Trans. Industry Applications*, vol. 34, no. 4, pp. 705 – 712, 1998.

[10] S. Y. Y. S. Kwon and D. Hyun, "Induction-heated cooking appliance using new quasiresonant zvs-pwm inverter with power factor correction," *IEEE Applied Power Electronics Conf. (APEC)*, pp. 575 – 581, 1999.

[11] M. N. H. Omori, H. Yamasita and T. Maruhashi, "A novel type induction-heating single ended resonant inverter using new bipolar darlington-transistors," *IEEE Power Electronics Specialists Conference (PESC)*, pp. 590 – 599, 1985.

[12] L. Cohen, "Evaluation and comparison of power conversion topologies," *Europian Power Electronics Conference (EPE)*, pp. 9 – 16, 1993.

[13] L. H. J. M. Leisten, "A parallel resonant power supply for induction cooking using gto," *IEE International Conference on Power Electronics and Variable Speed Drivers (PEVSD)*, pp. 224 – 230, 1990.

[14] J. M. B. J. A. S. Llorente, F. Monterde, "A comparative study of resonant inverter topologies used in induction cookers," *IEEE Applied Power Electronics Conference (APEC)*, pp. 1168 – 1174, 2002.

[15] Y.-C. Jung, "Dual half bridge series resonant inverter for induction heating appliences with two loads," *Electronics Letters*, vol. 35, no. 16, pp. 1345 – 1346, 1999.

[16] J. A. C. Carretero, O. Lucia and J. M. Burdio, "Phase-shift control of dual half-bridge inverter feeding coupled loads for induction heating purposes," *Electronics Letters*, vol. 47, no. 11, pp. 1345 – 1346, 2011.

[17] F. C. J. Y. G. Francois Forest, Eric Laboure, "Principle of a multi-load/single converter system for low power induction heating," *IEEE Transaction on Power Electronics*, vol. 15, no. 2, pp. 223 – 230, 2000.

[18] J. A. O. L. I. Millan, J.M. Burdio and D. Palacios, "Resonant inverter topologies for three concentric planar windings applied to domestic induction heating," *IEEE Electronics Letters.*, vol. 46, no. 17, 2010.

[19] J. M. B. J. A. Diego Puyal, Carlos Bernal and I. Millan, "Versatile high-frequency inverter module for large-signal inductive loads characterization up to 1.5 mhz and 7 kw," *IEEE Transaction on Power Electronics*, vol. 23, no. 1, pp. 75 – 87, 2008.

[20] M. S. Adler, "A field-theoretical approach to magnetic induction heating of thin circular plates," *IEEE Transactions on Magnetics*, vol. mag-10, no. 4, pp. 1118 – 1125, 1974.

[21] W. G. Hurley and J. G. Kassakian, "Induction heating of circular ferromagnetic plates," *IEEE Transactions on Magnetics*, vol. mag-15, no. 3, pp. 1174 – 1181, 1979.

[22] J. B. L. B. J. Acero, R. Alonso and J. Artigas, "An electromagnetic-based model for calculating the efficiency in domestic induction heating appliances," *IEEE Power Electronics Soecialists Conference (PESC)*, pp. 153 – 158, 2006.

[23] F. D. R. Rodriguez, J.M. Dishman and E. Whelan, "Modeling of two-dimensional spiral inductors," *IEEE transactions on Components, Hybrids and Manufacturing Technologies*, vol. CHMT-3, no. 4, pp. 535 – 541, 1980.

[24] J. B. L. B. J. Acero, R. Alonso and D. Puyal, "Analytical equivalent impedance for a planar circular induction heating system," *IEEE Transactions on Magnetics*, vol. 42, no. 1, pp. 84 – 86, 2006.

[25] W. G. Hurley and M. C. Duffy, "Calculation of self and mutual impedances in planar magnetic structures," *IEEE Trans. Magn.*, vol. 31, no. 4, pp. 2416 – 2422, 1995.

[26] W. A. Roshen, "Effect of finite thickness of magnetic substrate on planar inductors," *IEEE Trans. Magn.*, vol. 26, no. 1, pp. 270 – 275, 1990.

[27] W. A. Roshen, "Analysis of planar sandwich inductors by current images," *IEEE Trans. Magn.*, vol. 26, no. 5, pp. 2880 – 2887, 1990.

[28] J. A. Tegopoulus and E. E. Kriezis, "Eddy currents in linear conducting media," *Amsterdam: Elsevier*, ch.5, 1985.

[29] L. A. B. J. M. B. J. Acero, R. Alonso, "Modeling of planar spiral inductors between two multilayer media for induction heating applications," *IEEE Transactions on Magnetics*, vol. 42, no. 11, pp. 3719 – 3729, 2006.

[30] M. C. D. W. G. Hurley, "Calculation of self and mutual impedances in planar sandwich inductors," *IEEE Transactions on Magnetics*, vol. 33, no. 3, pp. 2282 – 2290, 1997.

[31] J. B. J. A. D. Puyal, C. Bernal and I. Millan, "Methods and procedures for accurate induction heating load measurement and characterization," *IEEE Transactions on Power Electronics*, pp. 805 – 810, 2007.

[32] C. C. J. Acero, O. Lucia and I. Lope, "Efficiency improvement of domestic induction appliances using variable inductor-load distance," *IEEE Transactions on Power Electronics*, pp. 2153 – 2158, 2012.

[33] I. M. O. L. R. A. J. Acero, C. Carretero and J. Burdio, "Analysis and modeling of planar concentric windings forming adaptable-diameter burners for induction heating appliances," *IEEE Transactions on Power Electronics.*, vol. 26, no. 5, pp. 1546 – 1558, 2011.

[34] J. M. B. J. Acero, R. Alonso, "Frequency-dependent resistance in litz-wire planar windings for domestic induction heating appliances," *IEEE Transactions on Power Electronics*, vol. 21, no. 4, pp. 856 – 866, 2006.

[35] J. M. B. R. A. L. B. J. Acero, P. Hernandez, "Simple resistance calculation in litz-wire planar windings for induction cooking appliences," *IEEE Transactions on Magnetics*, vol. 41, no. 4, pp. 1280 – 1288, 2005.

[36] J. B. J. Acero, R. Alonso and L. Barragan, "Enhancement of induction heating performance by sandwiched planar windings," *IEEE Electronics Letters.*, vol. 42, no. 4, 2006.

[37] D. E. T. W. A. Roshen, "Planar inductors on magnetic substrates," *IEEE Transactions on Magnetics*, vol. 24, no. 6, pp. 3213 – 3216, 1988.

[38] O. L. J. M. B. R. A. J. Acero, C. Carretero, "Analysis of the coupling between small ring-type coils used in adaptable-size burners for domestic induction heating hobs," *Applied Power Electronics Conference and Exposition*, pp. 2000 – 2006, 2011.

[39] R. A. J. B. C. Carretero, J. Acero and F. Monterde, "Modeling mutual impedances of loaded non-coaxial inductors for induction heating applications," *IEEE Transactions on Magnetics*, vol. 44, no. 11, pp. 4115 – 4118, 2008.

[40] K. W. E. C. L. C. Meng and W. M. Wang, "Thermal impacts of electromagnetic proximity effects in induction cooking system with distributed planar multicoils," *IEEE Transactions on Magnetics*, vol. 47, no. 10, pp. 3212 – 3215, 2011.

[41] D. Roncati, "Iterative calculation of the heat transfer coefficient," http://www.progettazioneottica.it.